2-D ELECTRONIC MATERIALS: EPITAXIAL GROWTH OF GRAPHENE ON 6H-SILICON CARBIDE (0001)

A Dissertation

Presented to the Faculty of the Graduate School

of Cornell University

in Partial Fulfillment of the Requirements for the Degree of

Doctor of Philosophy

by

Dorr Oliver Campbell

January 2015

2-D ELECTRONIC MATERIALS: EPITAXIAL GROWTH OF GRAPHENE ON 6H-SILICON CARBIDE (0001)

Dorr Oliver Campbell, Ph.D.

Cornell University 2015

Graphene holds great promise as a material for high-speed electronics, especially as Si technology approaches its performance limits. Growth of epitaxial graphene by thermal decomposition of SiC is considered to be one of the most promising production routes since it has the potential to produce homogenous, wafer-size films directly on a semi-insulating or semiconducting substrate.

Furthermore, graphene's planar 2-D structure enables devices and circuit designs with standard top-down lithography and processing techniques. However, the growth mechanism of graphene on SiC is not very well understood and much work remains to be done to improve the morphology, domain size and epitaxial quality of the grown graphene in order to take advantage of the unique properties of the material.

This research work was aimed at using a modified CVD chamber in the Cornell University Wide-Bandgap-Semiconductor Laboratory to optimize the growth of epitaxial graphene by controlled decomposition of 6H-SiC(0001) in an argon mediated gas flow at near atmospheric pressure. Grown films were characterized using Raman spectroscopy, atomic force microscopy, X-ray

photoelectron spectroscopy, transmission electron microscopy, and electrical measurements.

Uniform large-area monolayer and few-layer epitaxial graphene were successfully grown on SiC terraces of up to 8 μm wide, and with Hall mobilities of up to 840 $cm^2/V.s$. The as-grown graphene was found to be intrinsically electron doped with sheet carrier density in the range of 3 – 9 x 10^{12} cm^{-2}. However, certain growth features that tended to disrupt growth by uniform step flow decomposition were observed. These included deep rounded pits at higher temperatures, shallow triangular pits, arrow-like incursions across terraces, finger growths, residual SiC islands on terraces, nucleation of graphene at multiple defect points on terraces, and extra graphene layers at step edges. Further research is required to determine the mechanisms of formation of these features and to determine how they can be eliminated or reduced.

For the first time SiC grown epitaxial graphene films, transferred from the substrate by a special process, was imaged in plan-view by TEM. The TEM images, along with selected-area electron diffraction, showed that a bilayer film had the *AB* Bernal stacking.

BIOGRAPHICAL SKETCH

Dorr Campbell was born on October 16, 1959 in Westmoreland, Jamaica. His tertiary education began in 1981 with a B.Sc. in Natural Sciences from the University of the West Indies (Jamaica) where he majored in Pure Physics, Applied Physics (Materials Science) and Chemistry.

He completed his first Master's Degree in Metallurgical Manufacturing Processes and Management at the University of Birmingham, UK in 1985. He later earned a B.Eng. Degree in Mechanical Engineering in 1996 and also a Post-Graduate Diploma in Education in 2008, both from the University of Technology, Jamaica. In 2012 he earned an M.Sc. in Electrical Engineering from Cornell University.

Dedicated to my wife Grace who stood by me throughout this late journey

ACKNOWLEDGEMENTS

The author wishes to express sincere thanks to all who provided support and encouragement that enabled the completion of this effort. Special thanks to my Academic Advisor, Prof. Michael Spencer, who provided the most crucial support and advice which were needed to undertake and complete this program of study. I am also very grateful to Prof. Michael Thompson, Prof. R. Bruce Van Dover, and the late Prof. Lester Eastman for the support they kindly provided as members of my Academic Advisory Committee.

My sincere thanks to Mr. Scott Coldren, Manager of Student Services, for the tremendous guidance and help that he provided whenever I needed to have any administrative matter dealt with. To all my colleagues in Prof. Michael Spencer's Group who were willing to provide advice and important information to facilitate my progress, I am thankful.

Very special thanks to my wife Grace who accompanied me to Cornell University and made my sojourn so much easier.

Finally, thanks be to God for His numerous blessings and provisions.

TABLE OF CONTENTS

CHAPTER 1

INTRODUCTION

1.1 General

The objective of this research was to use a modified CVD chamber at the Cornell University Wide-Bandgap-Semiconductor Laboratory to optimize the growth of epitaxial graphene (EG) by the thermal decomposition of the Si-face of 6H-silicon carbide (6H-SiC(0001)), and to characterize the graphene grown. A particular goal was to determine the conditions required to obtain uniform monolayer graphene growth.

Graphene is a one-atom thick planar allotrope of carbon in which the carbon atoms are arranged in a hexagonal honeycomb pattern. It is essentially one isolated layer of graphite and was, in fact, first isolated and identified by Novoselov and Geim in 2004 by mechanical exfoliation of graphite [1]. Since then, graphene has drawn tremendous research interest due to its combination of exceptional and unique properties. Because of its remarkable electronic and other physical properties it is regarded as a novel material having great scientific and technological potential.

The carbon sp^2 bonding in graphene to form a two-dimensional crystal lattice is responsible for its extraordinary physical properties. It exhibits room-temperature ballistic transport property, has ultra-high intrinsic carrier mobility, high thermal conductivity and high elastic modulus. Furthermore, it

is ambipolar and gate-tunable for electron or hole conduction with very high current-densities [1-6]. Unlike in the traditional semiconductors, like Si, Ge and GaAs where hole mobility is lower than electron mobility, in graphene the mobilities are equal [7].

The technological importance of graphene is underlined by the fact that the 2010 Nobel Prize in Physics was awarded to Novoselov and Geim for their discovery of and contribution to understanding the properties and potential of graphene. Graphene holds great promise for the creation of high speed electronics operating in the GHz to THz range, and is considered as a possible substitute material for Si which is fast reaching its limit in size scaling for increased speed of devices. Also, its planar 2-D structure will enable device and circuit design to remain based on standard top-down lithography and processing techniques. In this respect it has a distinct advantage over carbon nanotubes. The strength and flexibility of graphene also makes it attractive for conformal and flexible electronics. It has the potential for a wide variety of applications ranging from RF FETs, NEMS resonators, ultra-high sensitivity gas sensors, broadband high-response photodetectors, non-volatile memories, transparent conducting electrodes for solar cells and LCDs, filler for composite materials, and one-atom-thick impermeable membranes [8-13]. Additionally, it provides a platform for fundamental research in physics based on novel properties, such as linear dispersion relationship in the electronic band structure, quantum Hall effects, and relativistic massless electrons (Dirac fermions) giving rise to such phenomenon as the Klein tunneling [2-6].

Before the 2004 isolation of graphene, it was generally accepted by the scientific community that one-atom thick two-dimensional materials could not physically exist by themselves [14]. However, since the discovery of graphene proved otherwise, there has been a surge in research to develop other two-dimensional materials. Of particular interest has been hexagonal boron nitride which is considered to be the chemical analog of graphene since it has similar hexagonal structure to graphene but with alternating boron and nitrogen atoms in the hexagonal structure. Hexagonal boron nitride, an insulator with completely different properties from graphene, is considered to be an excellent complementary substrate material for graphene electronic device applications [15-17]. Development of other two-dimensional pnictides, as well as, transition metal chalcogenides, such as, molybdenum disulphide (MoS_2), molybdenum diselenide ($MoSe_2$) and tungsten diselenide (WSe_2) is also being pursued. Of great interest is the development of devices based on graphene hetero-structures with other two-dimensional materials. For example, a high-response MoS_2-graphene hetero-junction photodetector with broad spectral range has been demonstrated [18].

1.2 Graphene Growth Methods

Several routes for obtaining graphene have been, or are being, developed. These include micromechanical cleavage of graphite, high-temperature thermal decomposition of silicon carbide (SiC), chemical vapor deposition (CVD) onto

transition metal substrates (typically, Cu and Ni), and CVD deposition onto dielectric substrates, such as sapphire (Al_2O_3), hexagonal boron nitride (h-BN) and silicon dioxide (SiO_2).

Micromechanical cleavage or mechanical exfoliation of graphite, the method used in the pioneering work of Novoselov and Geim, appears relatively simple and crude. It is achieved by using a scotch tape to peel very thin layers of graphite from a bulk crystal and repeatedly making the film thinner and thinner with the scotch tape before transferring the resulting small flakes unto a SiO_2/Si substrate by pressing the tape unto the SiO_2 surface. Monolayer, bilayer and thicker films, thus created, can be identified under an optical microscope by color contrasts [1, 19]. Bulk crystal of highly-oriented pyrolytic graphite (HOPG) is usually used as raw material, but Kish graphite is also used. This method results in high quality flakes of graphene, but the method is tedious and time consuming and only leads to small isolated crystals in the 10 μm range. Thickness and size are also difficult to control and yield is poor, hence the method is not suitable for commercial or large-scale scale device production. Nevertheless, mechanically exfoliated graphene has been used for extensive study of the fundamental properties of graphene. These high quality crystal also have the highest carrier mobility, typically in the order of 15,000 cm^2/V.s on a SiO_2/Si substrate and as high as 200,000 cm^2/V.s for freely suspended films [20].

Growth on transition metal foils, especially on Cu foil, by CVD is now an established route for preparation of wafer-size, large-area graphene films. The mechanism of growth is by elevated-temperature catalytic decomposition of a precursor hydrocarbon gas, typically methane (CH_4), at the surface of the metal. Hydrogen atoms desorbs leaving carbon atoms to aggregate by diffusion to form graphene. Synthesis of uniform wafer-size graphene films with high carrier mobility, (5,000 – 10,000 $cm^2/V.s$), has been achieved by this method [21, 22]. The major drawback of this method is that the graphene is grown on a conducting substrate which is not suitable for device fabrication. As a consequence, the film has to be transferred from the metal foil to a dielectric substrate such as SiO_2 on Si for electronic device applications. This involves the use of harsh chemical to etch away the metal substrate and which leads to contamination of the graphene film.

Direct growth of graphene on an insulating substrate is considered to be the most practical and scalable approach for 2-D graphene electronics as this would obviate the need for film transfer for device fabrication, which is the major problem with growth on metal substrates. Graphene synthesis by CVD deposition on such diverse dielectric substrates, as MgO, SiO_2, Si_3N_4, HfO_2, BN and sapphire, has been studied [15-17, 23-26]. However, to date these methods have not been able to produce graphene of a quality that is competitive with graphene grown on metal substrates or epitaxial graphene grown on SiC. High-temperature CVD growth on sapphire in hydrogen

mediated methane as precursor has so far given the most promising results [25].

1.3 Epitaxial Growth on SiC

High-temperature graphitization of the (0001) and $(000\bar{1})$ surfaces of SiC under high vacuum was investigated by van Bommel *et al* from as early as 1975, and in 2004 Berger *et al* first proposed the thermal decomposition of SiC as a viable route for the synthesis of graphene [27, 28]. This method shows promise for growing uniform, large-area, wafer-size graphene layers for various technological applications. Hence, for this thesis research graphene was directly grown on semi-insulating 6H-SiC(0001). The graphene that is produced this way is referred to as epitaxial graphene (EG), since the graphene grown is aligned with respect to the substrate.

Using SiC wafers as the growth substrate presents considerable advantages. To begin with, there is no need for externally supplied precursor gases since the carbon atoms required to form the graphene film come directly from the thermal decompositions of the SiC surface. Graphene can be obtained directly on a semiconductor or semi-insulating substrate so there is no need for transfer of the graphene film. Also, the planar substrate and growth geometry enables device and circuit design with standard top-down lithography and processing techniques. Furthermore, the SiC substrate itself is an excellent semiconductor that can facilitate direct integration with conventional electronics [29-31].

On the other hand, for the SiC route to fulfill its promise as a viable method for the production of graphene, it will have to develop to the point where uniform, large-area (wafer-size), low-defect graphene can be reproducibly and controllably produced on the SiC substrate. Although significant progress has been made to this end, much research is still needed to fulfill the required target, so research is still ongoing to develop this route for production of large-area graphene.

The basic method for growing epitaxial graphene on SiC is to heat the SiC substrate, in vacuum or in an inert environment, to temperatures usually in the range of 1200 °C to 1700 °C so that thermal decomposition of the basal plane surface occurs with desorption of Si atoms from the surface and rearrangement of the free carbon atoms into the graphene lattice. However, growth temperatures as high as 2000 °C have been reported [29, 32, 33]. Growth of EG occurs at the lower end of the temperature range for high-vacuum and ultra-high vacuum conditions while the higher end of the temperature range is found to be necessary for argon-mediated growths at near atmospheric pressures [34, 35]. This is discussed further in Section 1.3.2, below.

1.3.1 Si-Face versus C-face SiC Growth

Graphene can be grown on either of the two polar basal planes of 6H- or 4H-SiC, that is, on either the Si-terminated face (0001) or the carbon-terminated face $(000\bar{1})$ face of a nominally on-axis wafer (See Section 2.2 of Chapter 2).

Studies have clearly established that graphene films grown on the Si-face is significantly different from the films grown on the C-face in respect to growth rates, growth mechanisms, film morphologies, and electrical properties [27, 36-39].

For the same growth conditions, growth on the C-face is much faster than growth on the Si-face. Multiple layers (10 – 100) of graphene can grow very quickly on the C-face and film thickness and uniformity is difficult to control. For thick films, wrinkles invariably form in the films during cooling to room temperature due to the difference in thermal expansion between the graphene and the substrate. Additionally, individual graphene layers in the films on the C-face contain rotational stacking faults. This is evidenced by misalignment of films with respect to the substrate, as well as, turbostratic disorder in the films themselves, where individual graphene layers do not follow the Bernal *AB* stacking order. A study by Emtsev *et al* shows that this structure is due to weak interaction between the first graphene layer and the SiC$(000\bar{1})$ substrate [36]. Hite *et al* have studied graphene growth on C-face and found direct evidence that threading screw-dislocations in the SiC substrate act as preferred local nucleation sites for graphene growth, thus allowing a direct path for Si sublimation from the SiC [37]. This is in contrast to the general mechanism for growth on the Si-face by reverse step flow decomposition with sublimation of Si from retracting step edges. The carrier mobility of graphene grown on SiC$(000\bar{1})$ is comparable to that of exfoliated and metal-substrate CVD

graphene [40]. However, the lack of thickness control has been a major factor curtailing it use for electronic applications.

Growth on the Si-face starts with the formation of a carbon rich interfacial layer, variously referred to as “interface layer”, “buffer layer”, and “zeroth layer” (or “layer 0”) [34, 36, 40, 39, 41]. It will hereafter be referred to as the buffer layer in this report. This buffer layer is an initial graphene-like surface reconstruction of carbon atoms with a (6√3 x 6√3)R30° configuration, which forms before any graphene grows. Although its atomic arrangement is similar to graphene, it does not have the properties of graphene, and about one-third of the atoms in this layer are covalent bonded to the underlying SiC substrate, via the SiC dangling bonds. The buffer layer is always present with all as-grown graphene films on the Si-face. Emtsev *et al* proposed that each new graphene layer is formed at the bottom of existing layers by releasing the graphene-like buffer layer from the substrate as Si atoms evaporate, while a new buffer layer form. Thus, the azimuthal orientation of the buffer layer is inherited by each new graphene layer, leading to ordered stacking [36]. This is in contrast to growth on the C-face where it has been recently shown that a buffer layer forms only under specific growth conditions [42, 43]. A process of hydrogen intercalation can be used to eliminate the buffer layer after graphene is grown on SiC(0001) [40, 44-46]. The buffer layer is discussed further in Section 2.2.2.

It has proven much easier to grow uniform monolayer and bilayer graphene on the Si-face of SiC than on the C-face. This is the overriding reason why growth on the Si-face is still considered to be the preferred way to grow EG for electronic applications, even though the carrier mobility of Si-face graphene is relatively low, in the order of about 700-900 $cm^2/V.s$ at room temperature [35, 40].

1.3.2 Growth Pressure

When Berger *et al* first proposed the thermal decomposition of SiC as a viable route for graphene production in 2004, they proposed decomposition under ultra-high vacuum [28]. Hence, research up to 2009, aimed at understanding and optimizing EG growth on SiC, were conducted under ultra-high vacuum or high-vacuum conditions. However, in late 2008, Virojanadara *et al* first published results which suggested that higher growth temperature in combination with an argon ambient may be a key factor for obtaining large homogenous single layer graphene and, in early 2009, Emtsev *et al* published results that showed that growth at near atmospheric pressure resulted in significantly improved film quality [29, 35]. So, most current research on SiC graphene growth is carried out at atmospheric or near atmospheric pressures. For this thesis research, the graphene growths were generally carried out at close to atmospheric pressure. Further discussion on this is given in Chapter 2 and in the Results and Discussion section of this report.

1.4 Scope of Research

This thesis research was aimed at using a modified CVD chamber at the Cornell Wide-Bandgap-Semiconductor Laboratory to optimize the growth of monolayer epitaxial graphene by thermal decomposition of 6H-SiC(0001), and to characterize the graphene grown. Growths were generally done with argon flow at near atmospheric pressure, and the effect of growth temperature and time were investigated. The effects of argon flow rate and pressure, wafer quality, and stage rotation were not studied. Raman spectroscopy, atomic force microscopy (AFM), X-ray photoelectron spectroscopy (XPS), transmission electron microscopy (TEM) and van der Pauw electrical measurements were used to characterize the graphene grown. A limited elevated temperature oxidation study of EG was also done.

Chapter 2 of this report gives technical details of the structure and properties of SiC and graphene, as well as, an outline of EG growth models. Chapter 3 outlines the experimental procedures followed, Chapter 4 gives the results and discussion, and Chapter 5 provides the conclusions and recommendations.

CHAPTER 2

MATERIALS AND GROWTH MODELS

2.1 General

The first part of this chapter gives a detailed technical overview of the structure and properties of the two key materials in this research; (1) graphene, and (2) silicon carbide (SiC), the substrate used for the graphene growth. An understanding of the structure and properties of SiC is important in order to appreciate its importance as a substrate for graphene growth, and also to understand the mechanisms of graphene growth by this route. The second part of the chapter outlines growth conditions and models for epitaxial graphene.

2.2 Silicon Carbide

Silicon carbide is now recognized as an important substrate for epitaxial growth of graphene by controlled thermal decomposition of the SiC surface. But, since its availability in good quality crystalline forms, SiC itself has been widely used as a semiconductor material for high-temperature and high-power electronics due to its wide bandgap, high thermal conductivity, high electron saturation velocity, and high breakdown electric field [47, 48]. The band gaps for different forms of SiC vary from 2.39 eV to 3.33 eV [49]. For certain applications, such as high power switching and high frequency power

generation, it is technically superior to silicon. However, presently device fabrication using SiC is more complex than for silicon.

SiC crystallizes in many different polymorphic modifications referred to as *polytypes*, and over 250 have been identified. Although every atom, (Si or C), is tetrahedrally surrounded by four atoms of the other species, the polytypes differ in crystal symmetry, as well as, in the large number of possible variations of stacking order along the c-axis. The physical and electronic properties are very much dependent on the SiC polytype.

The polytypes of SiC occur in four distinct crystal symmetries. One form is cubic with a zincblende lattice, another form has the wurtzite structure, and all other polytypes have either a hexagonal unit cell (with $c/a > 2$) or a rhombohedral unit cell. Wurtzite is a specific member of the hexagonal crystal system.

The special case of polymorphism exhibited by SiC is a consequence the large number of possible variation of stacking order along the c-axis for polytypes with hexagonal and rhombohedral structures. The polytypes all have the same a and b lattice parameters (3.078 Å), that is, identical bilayers of Si-C, but different stacking sequence of these layers, and hence different c lattice parameters [50].

To identify the crystal structure of a polytype the most widely used nomenclature is that of Ramsdell (1947) [51]. In this convention, a number is assigned which gives the number of bilayers in the hexagonal unit cell, and a

letters C, H or R is assigned, which designate the crystal symmetry. The cubic form fits into this system by taking the [111] direction as "c-axis". The polytype with the wurtzite structure is denoted as 2H-SiC, reflecting its two bilayer stacking periodicity and hexagonal symmetry. There is only one possible cubic polytype, which is designated as 3C-SiC or β-SiC. Apart from identifying the numerous hexagonal and rhombohedral structures using the Ramsdell convention, they are also collectively referred to as α-SiC. The 4H-SiC and 6H-SiC hexagonal polytypes are the two most available, and the two of most interest for electronics. They are also the two polytypes that are commonly used for graphene growth, although growth on the 3C-SiC has also been carried out [33].

The atoms in a bilayer can be arranged in three configurations, A, B, or C in order to achieve closest packing. The stacking sequence of those configurations defines the crystal structure, with the unit cell being the shortest periodically repeated unit of the stacking sequence. The stacking sequences along the $(11\bar{2}0)$ plane for different SiC polytypes, including the 4H- and 6H-polytypes, are illustrated in Figure 2.1 [52].

Silicon carbide wafers are available in electron doped (*n*-type), hole doped (*p*-type) and semi-insulating grades. Nitrogen and aluminum are typically used for electron and hole doping, respectively. Wafer sizes of 50-, 75- and 100-mm (2-, 3- and 4-in) diameters are commercially available.

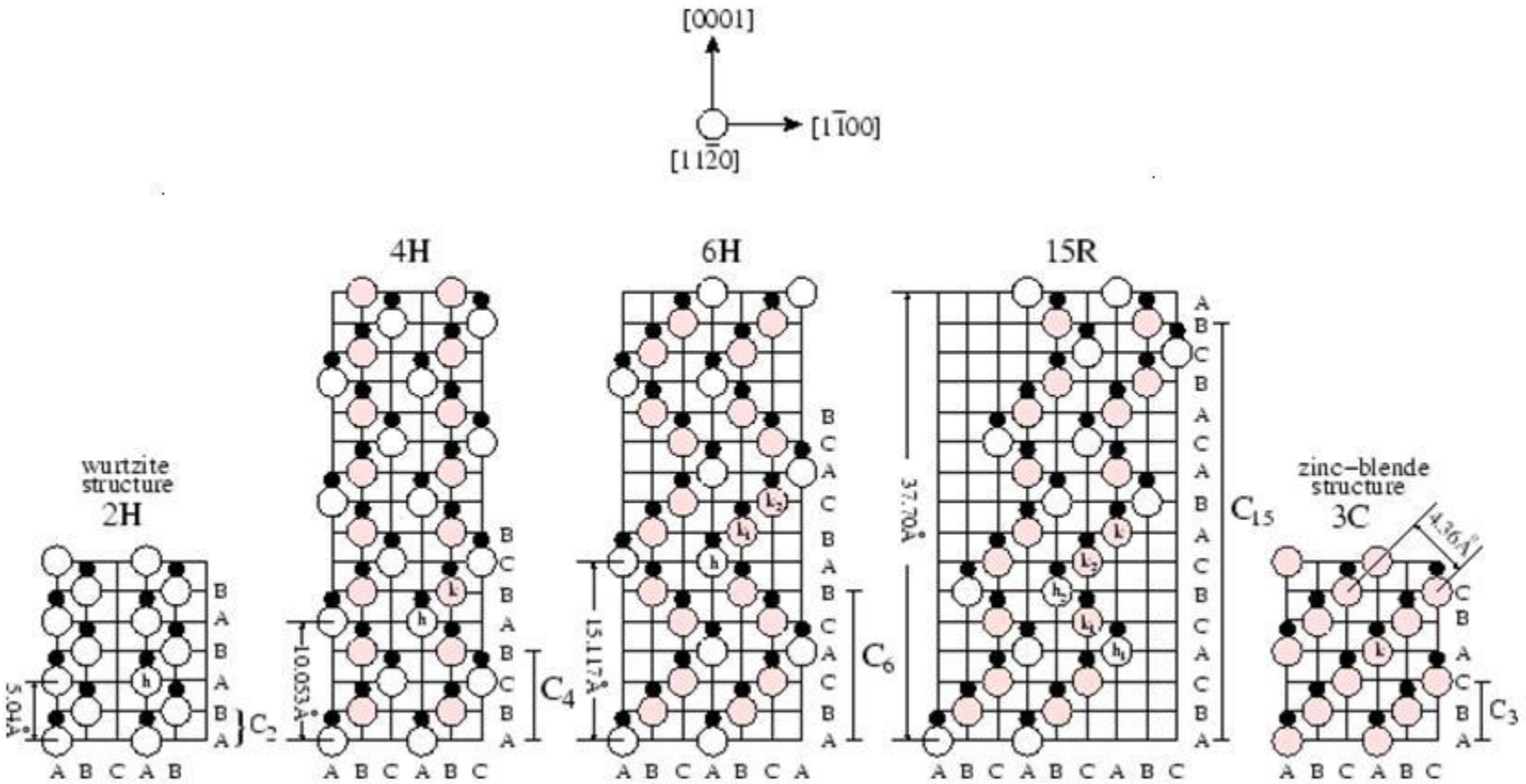

Figure 2.1: Stacking sequences for different SiC polytypes along the $(11\bar{2}0)$ plane [From Reference 52].

Nominally on-axis SiC wafers, that is wafers that are cut so that the wafer surface is approximately perpendicular to the crystal c-axis ([0001]-direction), have two polar faces: a Si-terminated face and a C-terminated face. However, by current wafer processing technology it is not possible to achieve precise wafer surface orientation, so there is always an "off-cut" angle which quantitatively describes the misalignment from precisely on-axis. The US Naval Research Laboratory has found typical off-cuts for nominally on-axis wafers from various vendors to range from 0° to 0.8° towards the $[11\bar{2}0]$ or $[1\bar{1}00]$ directions [31]. This misalignment from the nominal on-axis orientation results in the formation of steps and terraces on the wafer surfaces. It should be noted that smaller off-cut angles result in smaller step heights and wider surface terraces. Uniform graphene grown on wide terraces with small step heights is highly desirable for device fabrication [32, 53-57]. This is because wider terraces translate directly into lower step edge densities and also facilitate larger uniform domains of graphene. Uniform, large-area graphene on SiC is crucial for applications that will involve patterning. Furthermore, several researchers have correlated the surface morphology of SiC(0001) with the electronic properties of the graphene grown and found that step edges cause scattering of charge carriers, high vicinal step resistance, and reduced mobility [55-57]. The scattering at the step edges has been attributed to higher levels of point defects at these edges as well as the interruption to the homogeneity of the graphene film at step edges. It has been well established, both by the research done for this thesis and by other researchers, that

graphene grown by thermal decomposition of SiC(0001) usually result in thicker film thicknesses at the step edges as compared to that on the terraces themselves [35, 53]. Hence, films grown with narrow terraces and high step edge densities lead to increased inhomogeneity and reduced carrier mobility. In general, steps and other topographical feature, such as pits, surface roughness and various domain boundaries will influence the transport of epitaxial graphene grown on SiC.

Virojanadara *et al*, recognizing that one possible way to obtain larger terrace widths and smaller step heights could be to have substrates with better defined on-axis orientation, have investigated the effect of SiC substrate orientation on graphene morphology. They found that larger terrace widths and smaller step heights were obtained on substrates with a smaller mis-orientation from on-axis (0.03°) than on those with larger (0.25°) [32]. A related investigation by Robinson *et al* showed that step edge density increased with wafer mis-orientation resulting in a monotonic increase in average graphene thickness, as well as, a 30% increase in carrier density and 40% decrease in mobility for up to 0.45° miscut toward $[1\bar{1}00]$. However, beyond 0.45°, carrier mobility was similar to low miscut angles, although average graphene thickness and carrier density continued to increase [54].

2.2.1 6H-SiC

Semi-insulating 6H-SiC, supplied by II-VI Inc., was used for this thesis research. The wafers were 76.2 mm in diameter, 400 μm thick, and were

chemical mechanically polished (CMP) on the Si-face and optically polished on the C-face. Face orientation was nominally on-axis with a tolerance of ±0.5°.

Figure 2.2 shows a ball-and-stick model of the 6H-SiC crystal arrangement along the $(11\bar{2}0)$ plane, with the c-axis ([0001]-direction) pointing vertically upwards. The Si-face is the (0001) basal plane at the top and the C-face is the $(000\bar{1})$ basal plane at the bottom. Note that the thickness of a Si-C bilayer is 2.52 Å, so with six bilayers in the unit cell, the unit cell height is 15.12 Å. The stacking order is ABCACB… (See Figures 2.1 and 2.2).

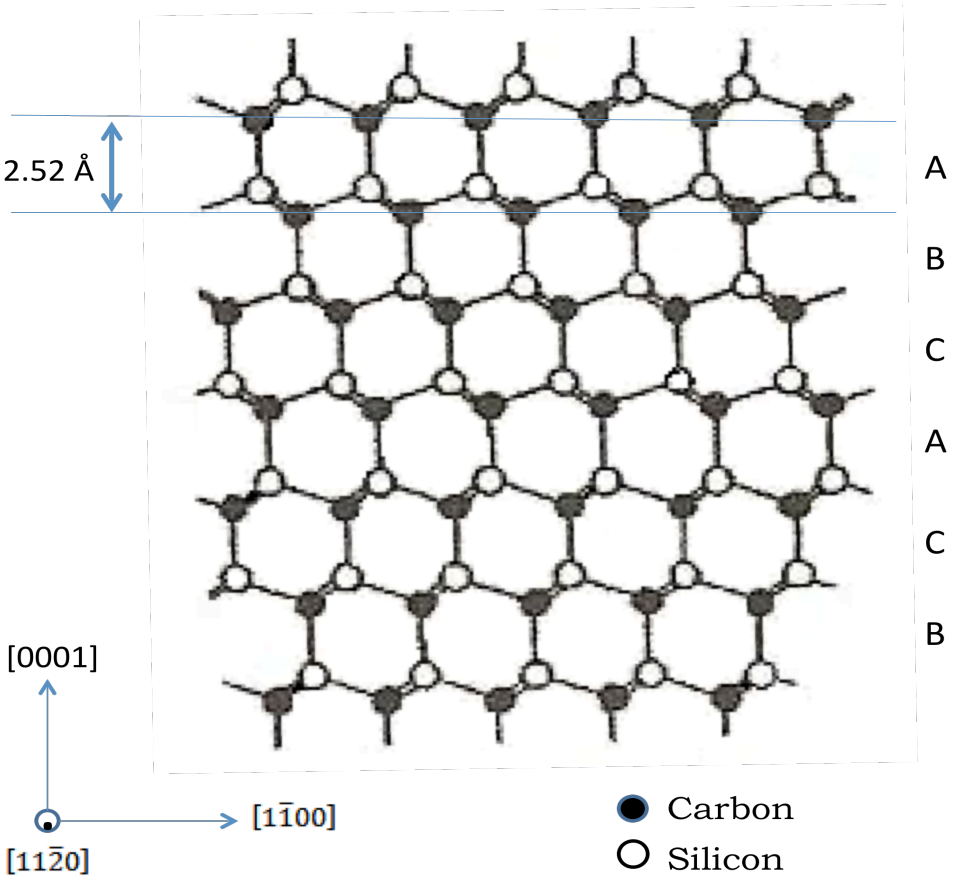

Figure 2.2: Crystallographic structure of 6H-SiC along the $(11\bar{2}0)$ plane. The Si-C bilayer height is indicated by the horizontal lines.

Based on the density of carbon atoms in each Si-C bilayer and the density of carbon in a graphene monolayer (3.820/Å^2), the decomposition of about three bilayers of SiC is required to form one layer of graphene of the same surface area [39, 58]. This requirement makes the layer-by-layer growth of graphene complicated.

2.2.2 Surface Reconstructions and Formation of (6√3 x 6√3)R30° Buffer Layer

The interaction between epitaxial graphene and the SiC substrate is critical in determining its electrical and physical properties. Hence, it is important to understand the nature of this interaction.

Prior to formation of graphene on either of the polar faces of SiC, the surfaces undergo a series of surface reconstructions as a function of both temperature and pressure [34, 36, 39, 41]. For the (0001) Si-face the final phase before graphene formation is a graphene-like (6√3 x 6√3)R30° reconstruction of carbon atoms which persists as an interfacial ("buffer") layer even after graphene growth. This Si-face buffer layer has been confirmed by several groups from samples prepared under various growth conditions [39, 43]. However, no interfacial buffer layer is generally present on the $(000\bar{1})$ C-face after graphene formation. As discussed before, this is a factor in the significant difference between graphene growths on the two faces. It should be pointed out however that recent work by a group at the Carnegie Mellon University (Feenstra *et al*) has shown that a graphene-like buffer layer does form during graphene growth

on the C-face under specific growth conditions [42, 43]. The Carnegie Mellon group found that when graphene is prepared on the C-face of SiC in a Si-rich environment, using either disilane at about 5 x 10^{-5} Torr or cryogenically purified neon at one atmosphere pressure, an interface structure with a (√43 x √43)R±7.6° symmetry forms. After oxidation by mild heating in the presence of oxygen, the (√43 x √43)R±7.6° structure transforms to one with (√3 x √3)R30° symmetry. It is argued that both of these structures are indicative of a graphene-like buffer layer that terminates the SiC crystal, and that, with additional graphene formation, this buffer layer is present at the interface between the graphene and the SiC, just as occurs for the Si-face surface. The progress of surface reconstructions for the (0001) Si-face is outlined, below.

Tromp and Hannon have studied the thermodynamics and kinetics of graphene growth on 4H-SiC(0001) under ultra-high vacuum and outlined the sequence of surface phase formation as follows, from Si-rich on the left-hand side to C-rich on the right hand side [34]:

$$(3x3)\rightarrow(1x1)\rightarrow(\sqrt{3}x\sqrt{3})\rightarrow(6\sqrt{3}x6\sqrt{3})+\text{graphene}$$

Based on their study using *in situ* LEEM and LEED, and balancing the rate of Si evaporation with an external flux of Si, they were able to construct the pressure-temperature (*p-T*) diagram shown in Figure 2.3. The *p-T* diagram clearly shows that phase transformations are shifted to higher temperature with increase in Si background pressure. Tromp and Hannon points out that heating under ultra-high vacuum, at temperatures where Si evaporates, drives

the surface out of thermodynamic equilibrium with little opportunity to control the kinetic of the phase transformation. This provides an explanation as to why ultra-high vacuum growth of graphene results in high surface roughness and small graphene domain size as compared to atmospheric pressure growth. Emtsev *et al*, one of the first proponents of EG at near atmospheric pressure, suggest that the reason for the observed improvement of the surface morphology of atmospheric pressure Ar-mediated growths is because, for a

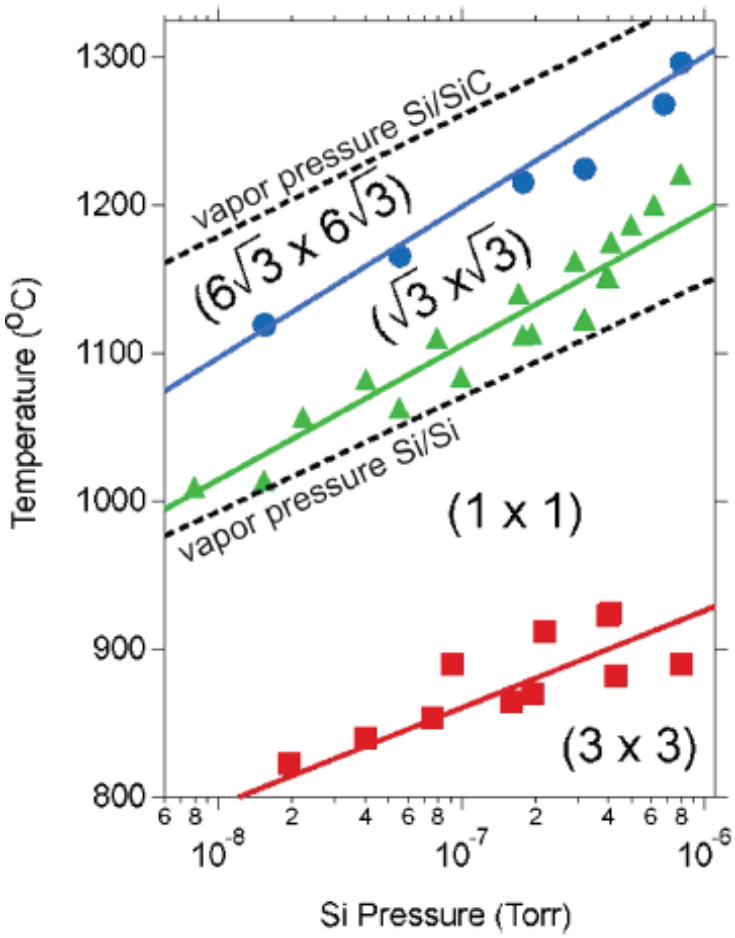

Figure 2.4: Pressure-temperature phase diagram for the 4H-SiC(0001) surface (from Tromp and Hannon, Reference 34). The equilibrium vapor pressure of Si over a Si substrate (lower dashed line), and the extrapolated equilibrium vapor pressure of Si over SiC (upper dashed line) are also plotted.

given temperature, the presence of high pressure argon lead to a reduced Si evaporation from the substrate. The presence of the argon atmosphere suppresses Si sublimation until significantly higher temperature is attained (up to 1500 °C) as compared to vacuum, where Si desorption start at about 1150 °C. The significantly higher growth temperatures possible under atmospheric pressure argon facilitates surface diffusion so that the restructuring of the surface is completed before graphene is formed, leading to marked improvement in surface morphology. Ultra-high vacuum growth (UHV) of EG was generally discontinued after 2009 when Emtsev *et al* showed that atmospheric pressure growth produce better surface morphology and larger domains of graphene on SiC step terraces [35]. Graphene grown in UHV typically have a high degree of substrate roughening and narrow terraces of less than 50 nm across [58].

2.2.3 Hydrogen Intercalation and Decoupling of Buffer Layer

One-third of the carbon atom in the buffer layer which is formed on SiC(0001) during graphene growth are covalently bonded to the Si atoms of the SiC surface, via the Si dangling bonds [36, 44]. So, although the buffer layer has a graphene-like hexagonal structure, the linear dispersion π-band structure of graphene does not occur in the buffer layer. Hence, it is insulating and it does not share the electronic properties of graphene (See Section 2.3). Ristein *et al* has shown that the *n*-type character of epitaxial graphene can be explained by donor-like states associated with the buffer layer and its interface to the SiC

substrate [59]. They show that an ensemble of electronic states associated with the buffer layer and the SiC surface can be combined into an interface density of states, and that the most plausible explanation for the *n*-type character of epitaxial graphene on SiC(0001) is electron transfer from these density of states to the graphene layer. The transfer of electrons from the donor states at the SiC/graphene interface will result in concurrent accumulation of positive charge at this interface that will act as scattering centers to strongly reduce the carrier mobility of the graphene [44]. Hence, for practical applications of EG, it is desirable to counteract the influence of this interface layer. Riedl *et al*, and subsequently other researchers, have shown that it is possible to decouple the buffer layer from the SiC substrate by hydrogen intercalation to form "quasi-free-standing" epitaxial graphene [40, 44-46]. Hydrogen intercalation is typically carried out by annealing as-grown EG between 600 °C and 1100 °C in a hydrogen-argon gas mixture at atmospheric pressure. The hydrogen decouples the buffer layer from the SiC surface by preferentially combining with and saturating the dangling Si bonds at the substrate surface, and the released buffer layer converts into a new graphene layer. Riedl *et al* showed that as-grown monolayer graphene is converted to bilayer graphene and a buffer layer alone can be converted to monolayer graphene by this process [44]. Figure 2.5 from Riedl *et al* illustrates the effect of the hydrogen intercalation process. The process has been shown to be reversible [44, 45].

Hydrogen intercalation has been found to result in marked improvement in the electric properties of the now decoupled graphene [40, 46]. This is attributed to the elimination of the buffer layer which is a known source of carrier scattering. Hence, the decoupled graphene has been termed "quasi-free-standing". For example, results from Robinson *et al* have shown that upon elimination of the buffer layer by hydrogen intercalation, there was a significant increase in carrier mobility from 800 $cm^2/V.s$ to more than 2000 $cm^2/V.s$ [40]. Also, Speck *et al* have obtained room temperature carrier mobility of 3100 $cm^2/V.s$ for a buffer layer converted to monolayer graphene by hydrogen intercalation [46]. Speck *et al* also found that the compressive strain normally observed in monolayer graphene was eliminated, and the graphene was hole doped in contrast to the usual electron doping observed in as-grown graphene.

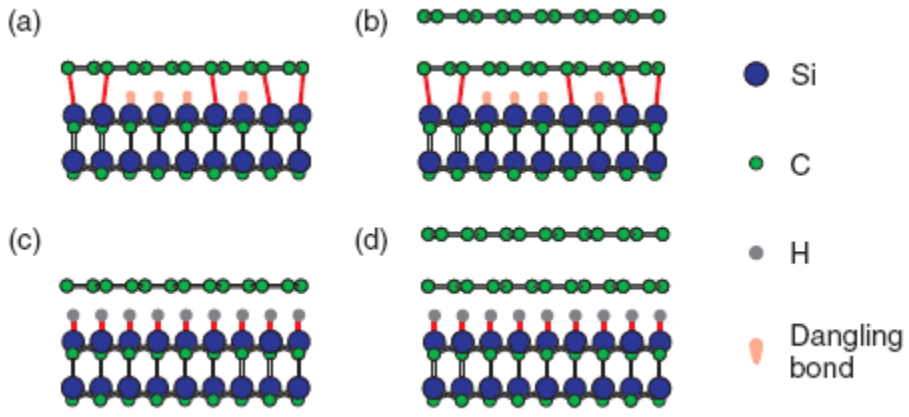

Figure 2.5: Models for the effect of hydrogen intercalation on buffer layer only [(a) and (c)], and on monolayer plus buffer layer EG [(b) and (d)]. (From Riedl et al, Reference 44).

It should be pointed out that it was found that the presence of the buffer layer also makes it more difficult to transfer as-grown EG film from the SiC substrate to other substrate or to TEM grids for analysis. So, for the films transferred for TEM analysis in this research, hydrogen intercalation of the as-grown EG was first carried out.

2.3 Graphene

Graphene is composed of carbon atoms arranged in a two-dimensional hexagonal lattice so that it has the appearance of a honeycomb structure (See Figure 2.6). It essentially an isolated layer of graphite in which graphene layers are stacked upon each other and held together by van der Waals bonds. This one-atom thick sheet of carbon atoms can be regarded as the basic carbon allotrope from which all the other carbon allotropes, of different dimensionality, can be formed. So, as indicated above, graphene sheets can be stack upon each other to form the three-dimensional graphite structure, and also tailored sheets of graphene can be rolled up into a tube to form one-dimensional carbon nanotubes or into a ball to form zero-dimensional fullerenes (Figure 2.7) [60].

Electronic bonding between the carbon atoms in graphene results from sp^2 hybridization of an *s*-orbital and two *p*-orbitals in the outer valence shell to form three trigonal σ-bonds per atom. These three in-plane σ-bonds form the rigid backbone of the hexagon and are responsible for the robustness of the lattice structure. The unaffected partially filled p_z orbitals, which are

perpendicular to the plane, lead to the formation of π-bands which are responsible for electron conduction. Figure 2.8 shows a schematic of the bonding structure, as well as, the hexagonal structure with the unit cell highlighted [39].

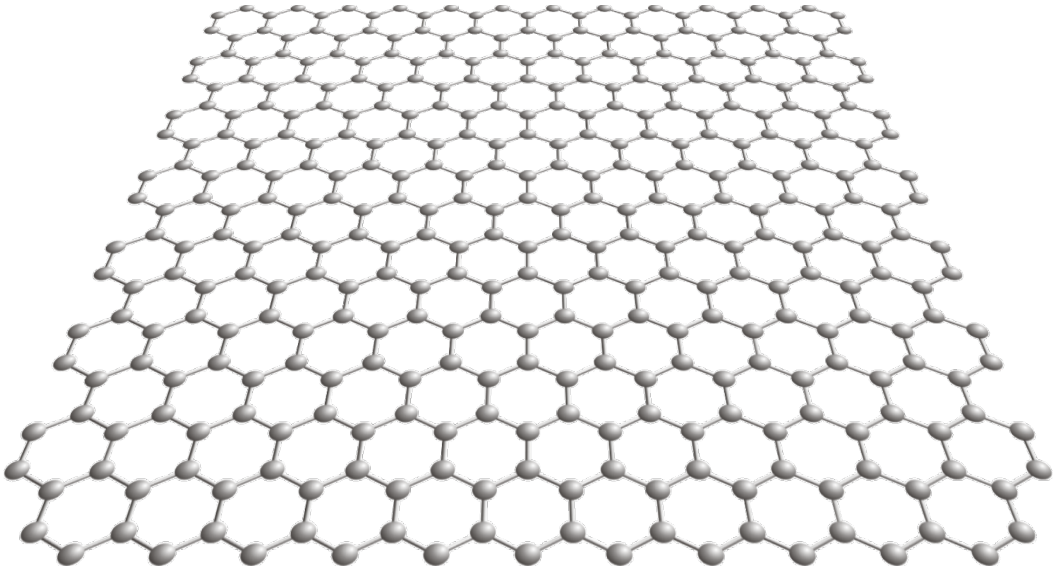

Figure 2.6: Two-dimensional honeycomb structure of graphene.

The electronic band structure of graphene shows linear dispersion of the π-bands near the K or K' point of the Brillouin zone (FBZ) as illustrated in Figure 2.9. Also, the π-bands intersect at these points, which make graphene a zero bandgap semi-metal. The point of intersection is called the Dirac point, and in neutral graphene the Fermi level is at the Dirac point. Also, the symmetry of the intersection is responsible for the ambipolar property of graphene. The linear dispersion of the π-bands is what gives graphene it unique transport

properties. Charge carriers act like massless relativistic particles, (called massless Dirac fermions), which are governed by a Dirac-like equation rather than the Schrodinger equation. Thus, very high carrier mobility and ballistic transport with long mean free path (up to about 0.4 μm) are achievable in graphene. Additionally, graphene exhibits some unique physical properties, such as, quantum Hall effects and Klein tunneling, and provides a unique platform for the study of a 2-D electron gas system [2 - 6, 39].

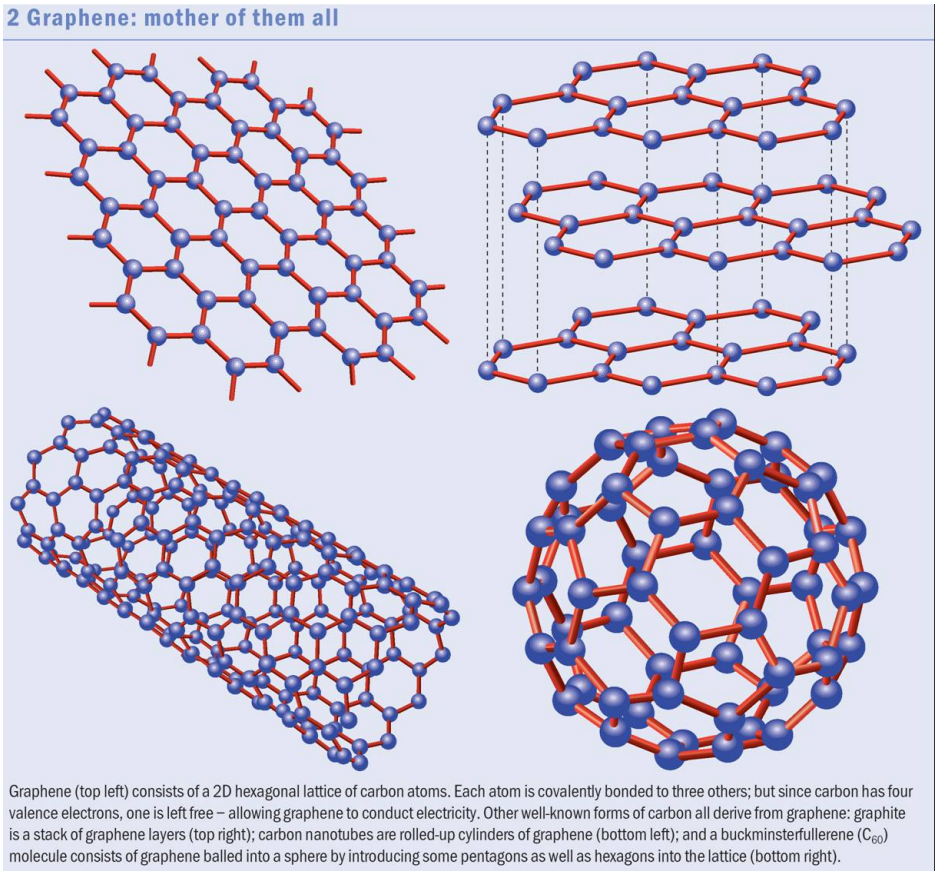

Figure 2.7: Showing how the different allotrope of carbon relates to the two-dimensional graphene sheet. (From Castro Neto, A.H., *et al.* (Reference 59)).

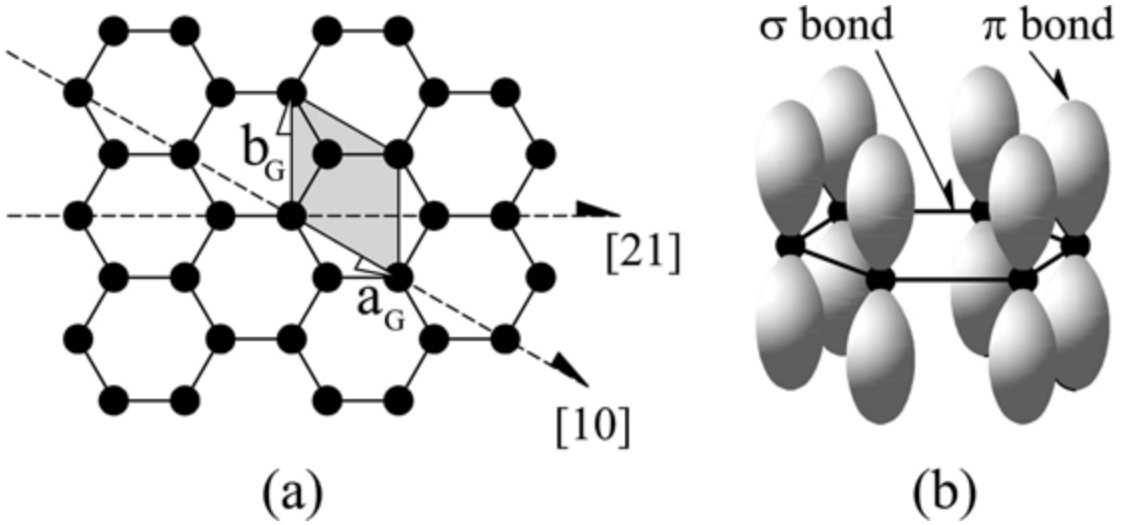

Figure 2.8: (a) Hexagonal structure of graphene. The unit cell (shaded) and standard unit cell vectors are shown. (b) Schematic of the bonding structure, consisting of in-plane σ-bonds and π-orbitals perpendicular to the plane of the sheets. (From Hass, J. *et al. Journal of Physics: Condensed Matter* **20**, (2008), 323202, Reference 39).

It should be pointed out that the interaction of graphene with an underlying substrate critically determines its electronic and physical properties. The highest carrier mobility and ballistic transport properties of graphene have been achieved for freely suspended high-quality films obtained by mechanical exfoliation of graphite. So, as indicated before, carrier mobility as high as 200,000 $cm^2/V.s$ has been obtained for freely suspended films, but this plummets significantly to in the order of 15,000 $cm^2/V.s$ when similar films are placed even on high-quality SiO_2/Si substrates [30]. For epitaxial films grown on SiC(0001) the carrier mobility is still significantly lower. This is a result of the interaction of the epitaxial graphene with the underlying substrate, which has been discussed previously in Section 2.2, in greater details. The dangling Si bonds terminating the bulk SiC surface, the presence of the interfacial

carbon-rich buffer layer, and surface morphological features such as step edges, pits and other domain boundaries all interact with the graphene film to determine the specific electronic and physical properties.

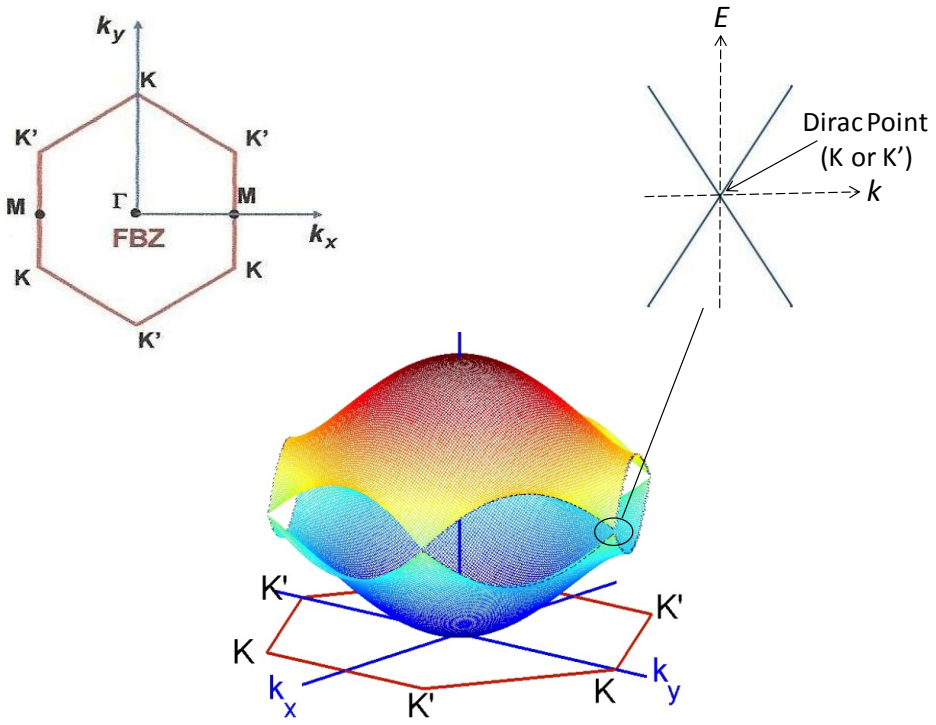

Figure 2.9: First Brillouin zone of the graphene crystal and the π-band structure. The linear dispersion of the band structure at the K and K' points is illustrated (conical in 3-dimensions). (Partly from Prof. Farhan Rana's class notes, ECE 4070, Cornell University)

2.4 Growth Models

Epitaxial growth of graphene on SiC(0001) entails a complex combination of processes, namely, SiC decomposition, Si desorption, step-flow patterns, interaction of SiC crystal defects, carbon diffusion, and graphene island

nucleation and growth. Furthermore, the process of graphene growth is markedly different from conventional chemical vapor deposition (CVD) processes in that the precursor atoms are not supplied from external sources but come from the substrate itself so that they are not homogenously distributed over the surface during growth. Both the decomposition of the SiC surface and the diffusion processes, (for desorption of Si, and nucleation and growth of graphene), require high temperatures, where at any given temperature all the processes may not be optimized but instead may be competing. Thus, much research is still required to fully understand the competing processes so as to optimize the growth of epitaxial graphene on SiC. Within this complex scenario a few simplified models of epitaxial graphene growths have been proposed. These are discussed below.

2.4.1 Step Flow Growth

The thermal decomposition process that produces graphene on SiC(0001) occurs preferentially at step edges, where Si and C atoms are least well bonded [61]. Research by Hupalo *et al* for graphene growth on 6H-SiC(0001) in UHV indicated that silicon desorption from steps is the main controlling process, and that different types of single bilayer steps released carbon at different rates causing them to retract at different speeds [58]. They graphitized a SiC substrate which initially had a regular series of single bilayer steps, without doing any H_2 etching prior to graphitizing, and were able to follow the progress of step recession and graphene growth using scanning tunneling microscopy

(STM). From the STM data and the fact that stoichiometry requires the carbon atoms contained in about three SiC bilayers to form a single graphene sheet, they proposed the growth model illustrated in Figure 2.10 for the formation of graphene islands, fingers and continuous layer. The model shows three adjacent steps retracting at different speeds as indicated by the relative lengths of the arrows drawn on the surfaces and also based on how they are numbered, (1 is fastest, 3 is slowest). The steps retract by evaporation of Si and release of C.

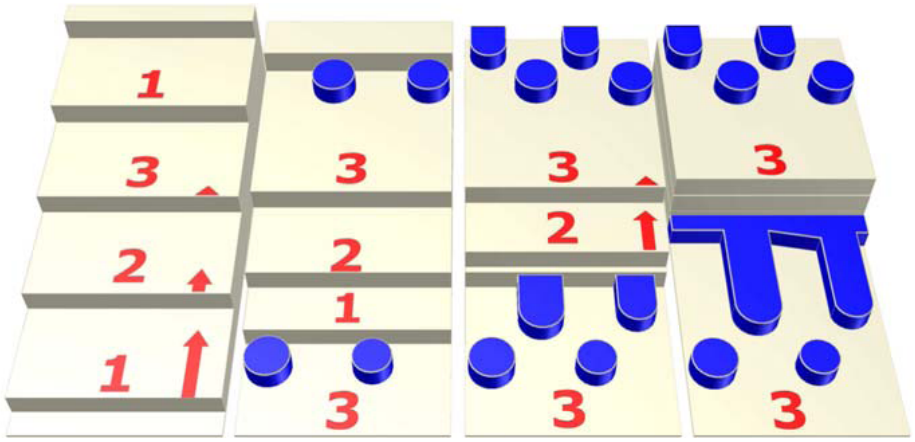

Figure 2.10: A schematic growth model of graphene on 6H-SiC. Three adjacent steps having different retraction speeds generate successively graphene islands, fingers, and a continuous layer. (From Hupalo, M., *et al. Physical Review B* **80**, 041401(R) (2009), Reference 58).

Single bilayer step number 1, with the fastest retraction speed, decomposes fast and catches up with the edge of step 2, and in doing so releases only enough carbon atoms to form graphene islands. In catching up with step 2, step 1 now form a two-bilayer step with 2. The two-bilayer step formed from 1

and 2 is retracting faster than step 3 and eventually catches up with it to form a three-bilayer step, and in doing so releases only enough carbon atoms to form larger finger-like islands. The three-bilayer step formed by steps 1,2 and 3 then continues to retract together producing a sufficient number of carbon atoms to form a continuous graphene film. This model suggests that depending on the progress of growth, the sample can consist of different extents of island, finger or continuous film of graphene. It also points to the importance of the morphology of the SiC substrate prior to graphitization in achieving uniform graphene growth.

The important observation by Hupalo *et al* that different SiC steps have different evaporation rates is consistent with the data provided in a paper by Kimoto *et al* on step bunching mechanism in chemical vapor deposition of 6H- and 4H-SiC(0001) [62]. In the situation described here, growth is by step-controlled epitaxy, where crystal growth proceeds in a step-flow mode. The authors proposed a model of step bunching based on minimization of free energy during crystal growth, taking into consideration the extra energy required for adding a new layer onto a particular terrace. Several types of terraces exist on SiC(0001), owing to the peculiar stacking sequence (See Section 2.2.1). Kimoto *et al* showed, for example, that 6H-SiC has three distinct terraces on which the deposition of a new layer has different energy costs. The terrace requiring the least extra energy to facilitate deposit and growth would grow faster by step-flow, and vice versa.

For epitaxial graphene growth on SiC, the opposite of what is just described above would be the case. The SiC steps would be bunching by decomposing in a reverse step-flow manner, but, by similar reasoning, different types of terraces would erode at different rates. In this case, steps with higher surface energies would be expected to erode more favorably and faster so as to generally minimize total surface energy. Figure 2.11, from Yazdi *et al*, using data from Kimoto *et al*, illustrate this for 6H-SiC [33]. The distinct terrace types are designated 6H1, 6H2 and 6H3 as was done by Kimoto *et al*. However, in this figure it is the energy required for desorption that is indicated, hence

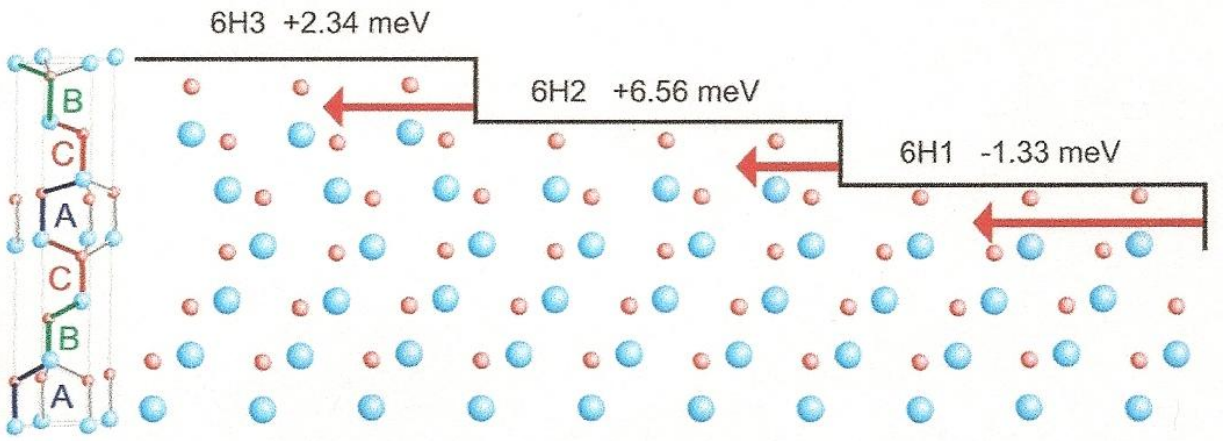

Figure 2.11: Stacking sequences and possible terrace on 6H-SiC. Large blue spheres and small red spheres represent Si and C atoms, respectively. The surface energies needed to remove particular terraces are indicated, the lengths of the red arrows indicates relative decomposition rates. (From Yazdi *et al*. *Carbon* **57**, (2013) 477-484, Reference 33).

the lower the energy the faster the step flow will be. Note that the terrace with the highest energy to deposit will need the lowest energy to erode and vice versa.

A mechanism based on differential step flow can also be used to model the formation of SiC islands, (with buffer layer), which are sometimes observed on terraces along with graphene growth [63] (See Section 4.4.2 of Chapter 4: Results and Discussion). These islands are believed to occur when SiC/buffer layer, sandwiched between graphene finger growths, do not proceed to complete decomposition, even after the step front from which they originate has completely eroded away. Increasing the growth time or growth temperature should cause these islands to shrink towards the point where the surface is completely covered by graphene.

Ohta *et al* have studied the role of carbon surface diffusion on the growth of epitaxial graphene on SiC in an argon-mediated atmosphere [64]. They found that carbon diffusion governs the spatial relationship between SiC decomposition (Si sublimation) and graphene growth, and that growth mechanisms depend strongly on the initial surface morphology. Ohta *et al* conclude that simple step flow growth is not possible at isolated single bilayer SiC steps because instabilities caused by carbon diffusion lead to complex growth morphologies (arrows, fingers). (See Section 4.4.1 and 4.4.2 of Chapter 4: Results and Discussion). However, triple bilayer steps allow large continuous graphene sheets to grow by step flow, even for vacuum growths. Furthermore, they proposed that the improvements in the Ar-assisted method are caused by a changed buffer layer surface morphology, rather than fundamental differences in the mechanism by which graphene forms.

The mechanism for the formation of arrow-like feature, proposed by Ohta *et al*, is summarized as follows. If the SiC surface from which growth starts consist of a terrace with single bilayer step edge, the decomposition of the terrace, beginning at the step edge, will only provide sufficient C atoms to nucleate graphene ribbons which will decorate the step edge and retard further step edge decomposition along the boundary where it is covered by graphene.

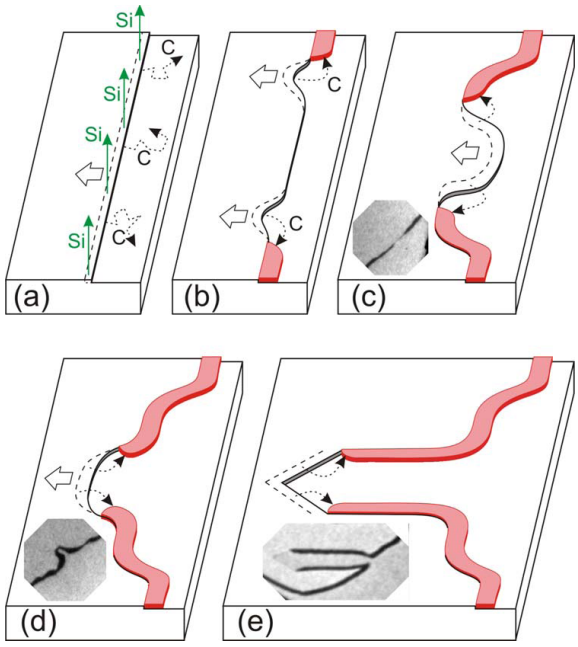

Figure 2.12: Schematic of the mechanism of formation of an arrow feature. The insets show static LEEM images of SiC bilayer steps at similar stages of evolution. (From Ohta *et al*. *Phys. Review B* **81,** 121411(R) (2010), Reference 64).

Subsequent etching occurs preferentially near the point of contact of the graphene ribbon with the undecorated SiC step, so that the graphene ribbon is drawn along the etched step. Eventually, the initial step edge becomes entirely

decorated by the graphene ribbon, and etching will occur only if new lengths of SiC steps are created by rapid etching dents in the step edge when two ribbons approach each other, thus forming an arrow feature. Ohta *et al* also used kinetic theory to show that arrow geometry represents a stable steady-state geometry of graphene growing via diffusion-limited etching of SiC bilayer steps. The mechanism is illustrated in Figure 2.12.

There is little quantitative understanding of the kinetics of EG growth. Borovikov and Zangwill have however proposed a theory based on a linear stability analysis of a step equation of motion that predicts the separation between EG fingers as function of growth temperature, background Si pressure, and the influence of an inert gas in the growth chamber [61]. They proposed a local heat release mechanism, to explain the finger-like structure that is observed when graphene is grown by step flow decomposition of Si(0001), as follows. Thermal decomposition of SiC starts at random points along step-edges and releases free carbon to crystallize into new buffer layer material with strong σ-bonds. This releases heat that transiently increases the local temperature and promotes further decomposition at the points along the step where it has already begun (See Figures 2.13 and 2.14). For quantitative analysis, they used $h(x, t)$ to denote the position of the SiC step edge, and assume that the decomposition rate depends of the curvature of the front. Hence, they gave the following as a suitable evolution equation for $h(x, t)$:

$$\frac{\partial h}{\partial t} = -V - aV\frac{\partial^2 h}{\partial x^2} + \sigma\Gamma\frac{\partial^2 h}{\partial x^2} - \sigma D\frac{\partial^4 h}{\partial x^4} \qquad (1)$$

Where, V is the average velocity of the step due to decomposition, a is the SiC lattice constant, $\sigma = a\gamma/kT$, γ is the SiC step stiffness, $\Gamma = \nu \exp(-E_1/kT)$ is the mean rate at which atomic species detach from a straight SiC step, ν is the attempt frequency, and $D = a^2\nu \exp(-E_2/kT)$ is the edge diffusion constant.

Borovikov and Zangwill points out that the last two terms of equation (1) are from extensive studies of the effect of capillary smoothing on the morphology of step edges on vicinal surfaces. The second derivative term models evaporation-condensation events where atoms detach from a step edge, migrate rapidly on the adjacent terrace, and re-attach to the step elsewhere. The fourth derivative term models edge diffusion events where atoms migrate along the step edge itself.

For linear stability analysis, Borovikov and Zangwill assume that equation (1) has a solution of the form: $h(x,\ t) = -Vt + \varepsilon(t)\sin(2\pi x/\lambda)$, where $\varepsilon(t)$, the perturbation amplitude, grows (decays) exponentially when the wavelength λ, (ie., separation between fingers), is greater (less) than a critical value. The most unstable (fastest growing) wavelength λ_m is given by:

$$\lambda_m = \sqrt{\frac{8\pi^2\sigma D}{aV - \sigma D}} \qquad (2)$$

From kinetic theory, the average step velocity is given, in terms of the difference between the flux of Si atoms sublimating from the surface (as

measured by the equilibrium vapor pressure of Si over SiC) and the growth chamber background pressure P, as:

$$V = \beta \frac{a^3}{\sqrt{2\pi m k_B T}} \left(P_{eq} - P\right) \qquad (3)$$

Where m is the mass of a Si atom, P_{eq} is the equilibrium vapor pressure of Si which is given by $\log_{10} P_{eq}(\text{Pa}) = 12.74 - 2.66 \text{ x } 10^4/\text{T(K)}$, and β is the evaporation coefficient.

Also, Borovikov and Zangwill noted, (from the work of Tromp and Hannon), that that growth temperature T_G is shifted to higher temperature as P increases, and no decomposition occurs if $P > P_{eq}$ [34]. (See Figure 2.4)

Using equations (2) and (3), and the information just indicated in the last paragraph above, Borovikov and Zangwill made plots to show the dependence of the fastest growing wavelength with growth temperature for several values of background Si pressure P (See Figure 2.15). In doing this they used rough approximation for the constants γ, E_1, E_2 and β since none of these is truly known for SiC. They found that the theory agreed semi-quantitatively with experimental results.

From their plots of λ_m as a function of temperature for different Si background pressures (Figure 2.15), Borovikov and Zangwill point out the following. There is no graphene growth when $T < T_G$ and step edges are absolutely stable (no fingers) when $T > T_S$. Between T_G and T_S, there is a temperature window where

the step edge is unstable. The window is largest for the UHV growth and decreases as P increases. There is a critical pressure, P_S, above which graphene growth occurs with no morphological instability of the SiC step edges. Below P_S and just above T_G, there is a narrow region of stable growth.

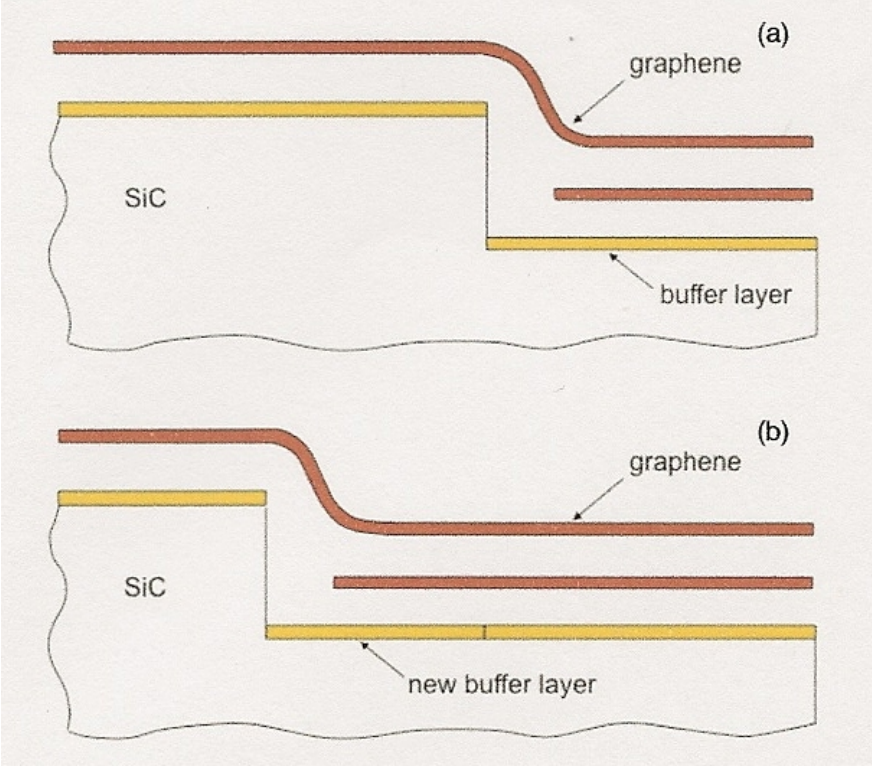

Figure 2.13: Graphene growth on at a step on Si(0001): (a) Upper step begin to decompose and liberate Si and C atom. The upper buffer layer transforms to graphene the liberated C atoms recrystallize at base of the step to extend the lower buffer layer. (b) Advance of second graphene layer. (From Borovikov and Zangwill. *Physical Review B* **80** (12), p.4, (2009), Reference 61).

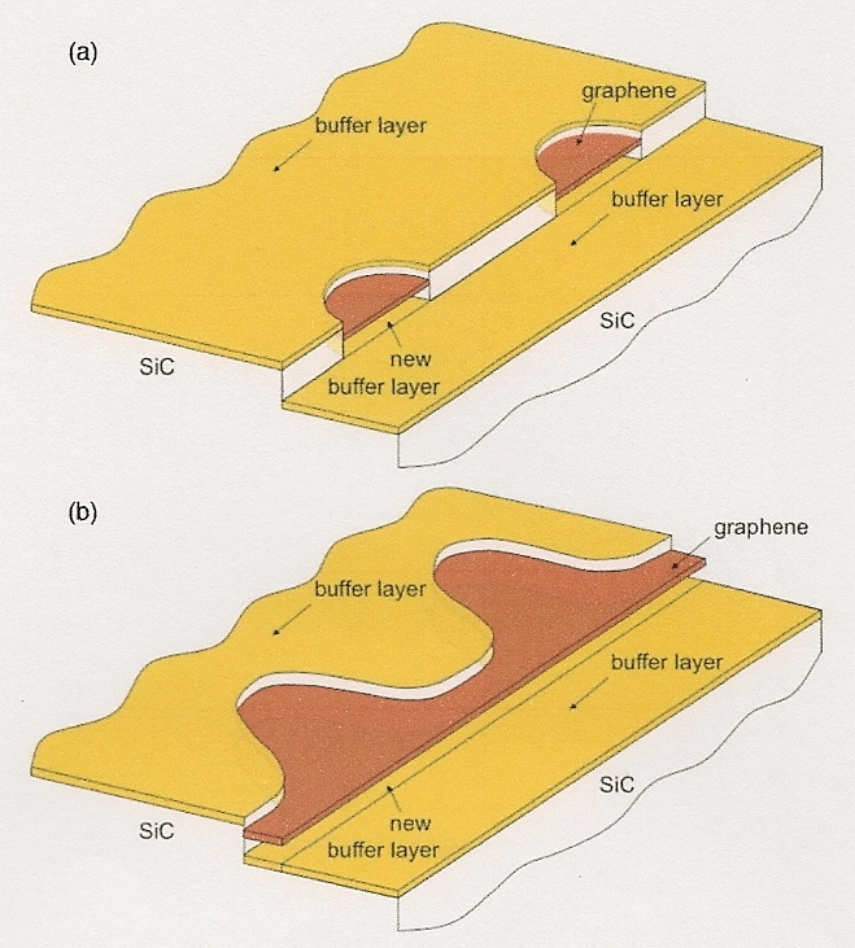

Figure 2.14: Onset of instability: (a) thermal decomposition of SiC starts at random points along the step edges; (b) the formation of new buffer layer releases heat, which locally accelerates further decomposition and graphitization. The topmost complete graphene layer is not shown. (From Borovikov and Zangwill. *Physical Review B* **80** (12), p.4, (2009), Reference 61).

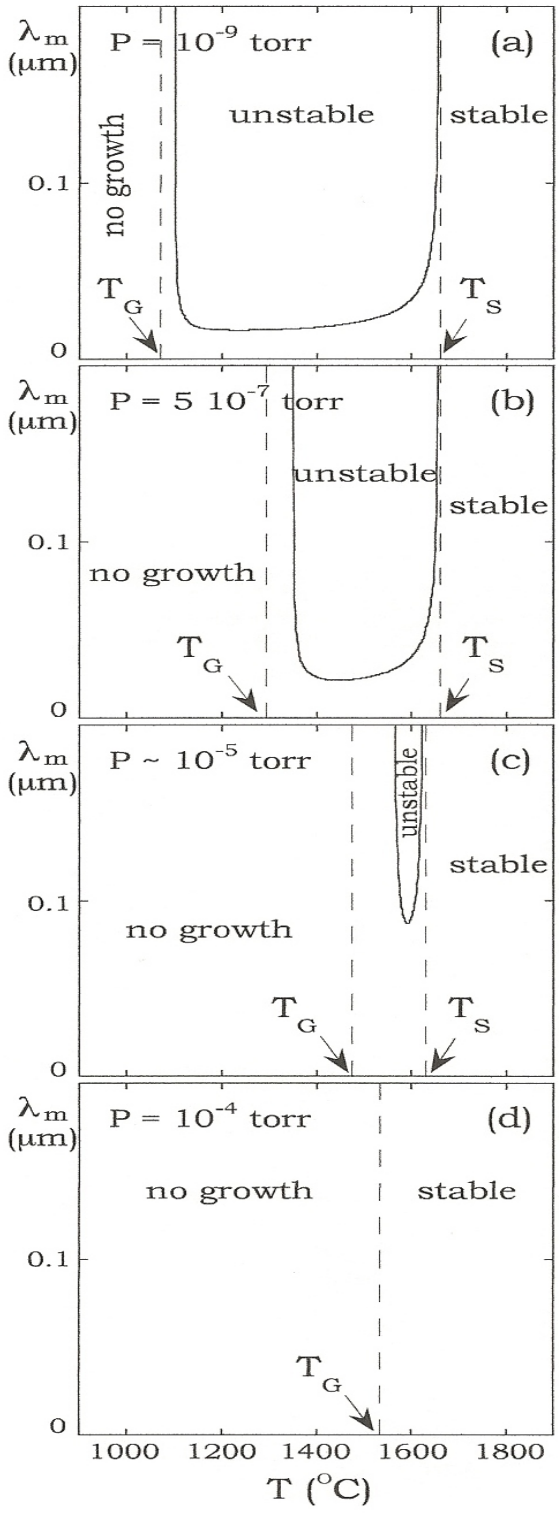

Figure 2.15: Dependence of the fastest growing wavelength λ_m on the growth temperature T for several values of the background Si pressure P. (From Borovikov and Zangwill. *Physical Review B* **80** (12), p.4, (2009), Reference 61).

CHAPTER 3

EXPERIMENTAL PROCEDURES

3.1 Introduction

All growths were carried out in a vertical, water-cooled, cold-wall, stainless steel chamber. This growth chamber was cylindrical in shape with a base pressure of about 2.0 x 10^{-8} Torr, when cold. The chamber was kept at its base pressure by a Pfeiffer turbo-molecular pump when not in use. Pressure in the chamber was monitored by an ion gauge for low pressures, by a Baratron pressure transducer for intermediate pressure range, and by a Pirani gauge for pressures nearer atmosphere. The chamber incorporated two heating elements: a graphite filament just below the top of a stage in the chamber for sample placement, and a tungsten filament, placed like a showerhead, about two inches above the sample stage. Either or both filaments could be used for heating the sample during growth. With both filaments operating, temperatures up to about 1800 °C could be achieved. Figure 3.1 gives a picture of the growth chamber and figure 3.2 give a schematic of the filaments configuration in relation to sample placement.

Growth temperatures were measured using an infrared pyrometer focused on the surface of the graphite susceptor (carrier) on which growths were carried out. The furnace had to be pre-profiled to determine what power input to the filaments was necessary to achieve different temperatures of growth.

Additional details on the temperature profiling are given in Section 3.2 of this chapter.

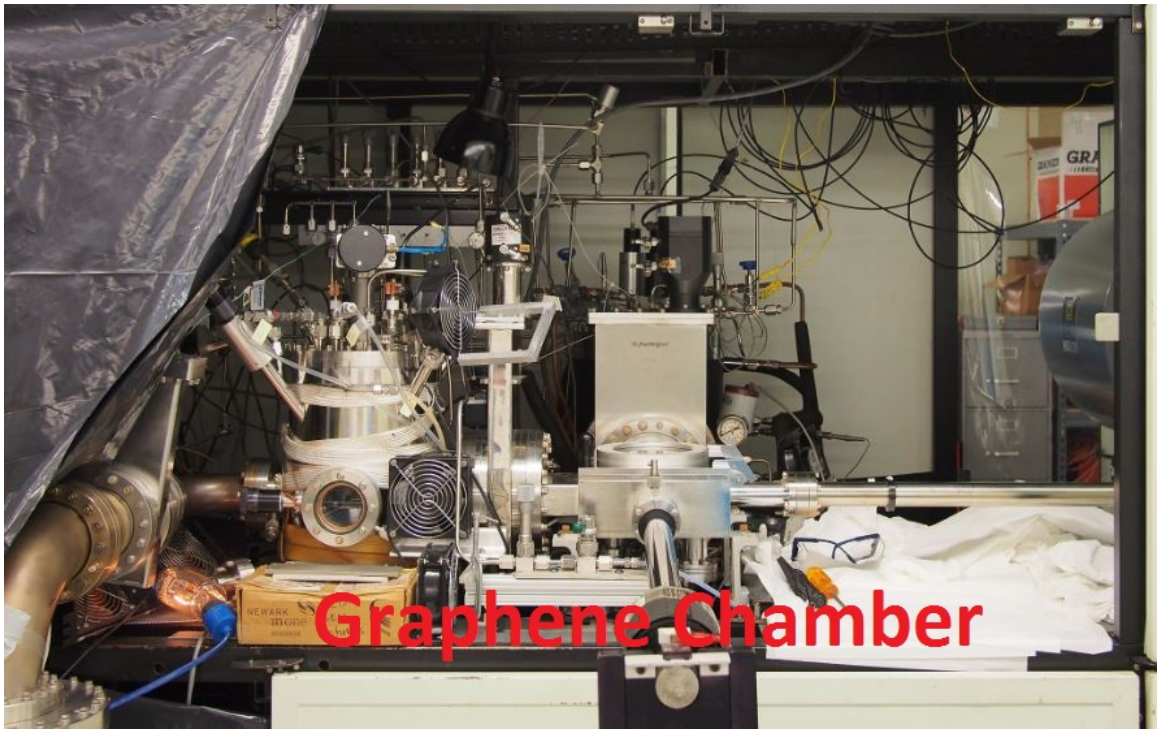

Figure 3.1: Picture of the graphene growth chamber. Auxiliary equipment such as pumps, power supplies, controls and displays are not shown.

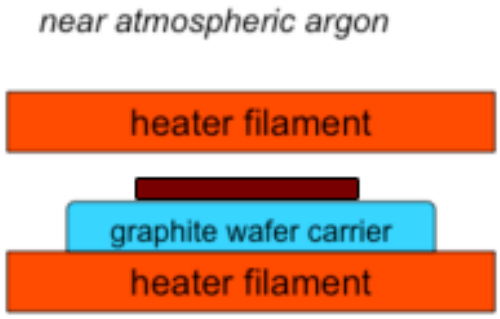

Figure 3.2: Schematic drawing of the heater filaments in relation to sample placement.

It was initially believed that it would be necessary to use both filaments to establish temperatures for graphene growth. However, it was subsequently discovered that one filament was sufficient. All growths were then done using the lower filament only.

Most of the growths were done at near atmospheric pressure in an argon ambient. However, some initial trial growths were done under high-vacuum conditions. Some initial growths were also conducted with rotation of the stage in the chamber, but this was discontinued after the system lost this functionality. Finally, although some initial growths were done with argon flow into the side of the chamber near the base, this was discontinued and flow was done through the top cover of the chamber as this provided better laminar flow patterns.

The effect of argon flow rate was not investigated in this study. For most growths a flow rate of about 2000 sccm was used.

Samples for growth were cut from 3-inch diameter, semi-insulating 6H-SiC wafers supplied by II-VI Inc. The wafers were nominally on-axis, chemical mechanical polished (CMP) on the (0001) Si-face and optically polished on the $(000\bar{1})$ C-face. Depending on the range of analysis to be done on the grown graphene, three different sample sizes were used: 6 mm x 6 mm, 6 mm x 12 mm and 12 mm x 12 mm.

The graphene grown on the SiC samples were characterized using Raman spectroscopy, atomic force microscopy (AFM), X-ray photo-electron spectroscopy (XPS), transmission electron spectroscopy (TEM), and Hall mobility measurements. A limited elevated temperature oxidation study of multilayer graphene grown under high-vacuum conditions was carried out to assess the inertness (or reactivity) of graphene when heated in an oxygen-rich environment. Transfer of graphene from the SiC substrate to other substrates was carried out to determine film transfer characteristic. Also, graphene films were transferred to TEM grids for TEM structural characterization.

3.2 Temperature Profiling of Growth Chamber

Before growths were started, and after modifications to the growth chamber, temperature profiling was done to determine the power input to the filaments necessary to achieve a given temperature at the position where growth was carried out in the chamber under the usual argon flow rate. This was done with both filaments powered, or with only the bottom filament powered. The infrared pyrometer was focused unto the graphite carrier in the chamber and the power inputs to filament(s) were manually adjusted to achieve the temperature required. The error in temperature setting was estimated to be about ±10 °C. Plots of temperature against power input have been prepared. Example calibrations are shown in Figures 3.3 and 3.4.

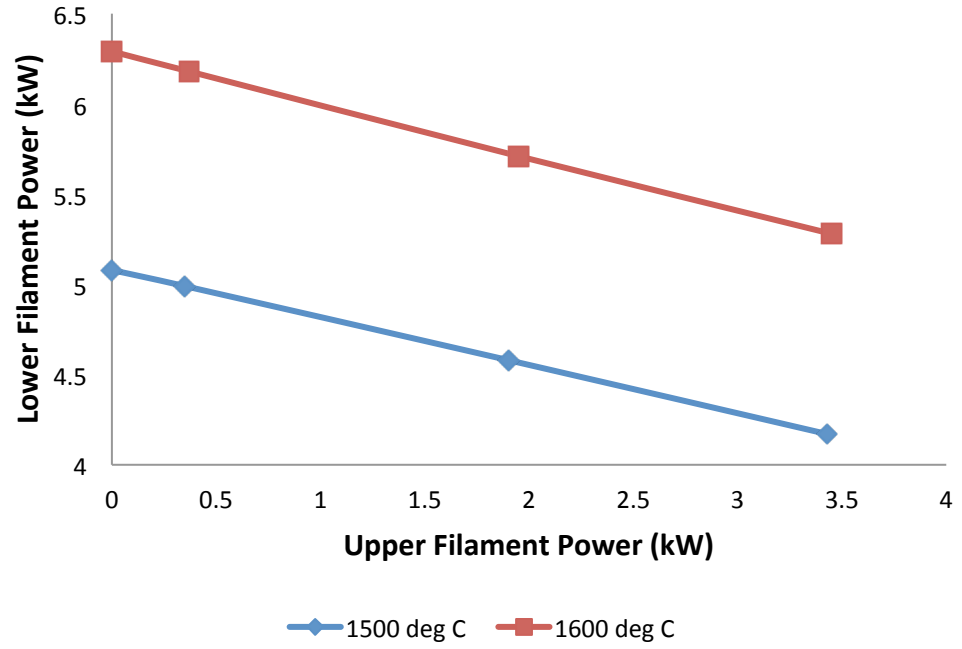

Figure 3.3: Power inputs for sample temperatures of 1500 °C and 1600 °C using both upper and lower filaments together.

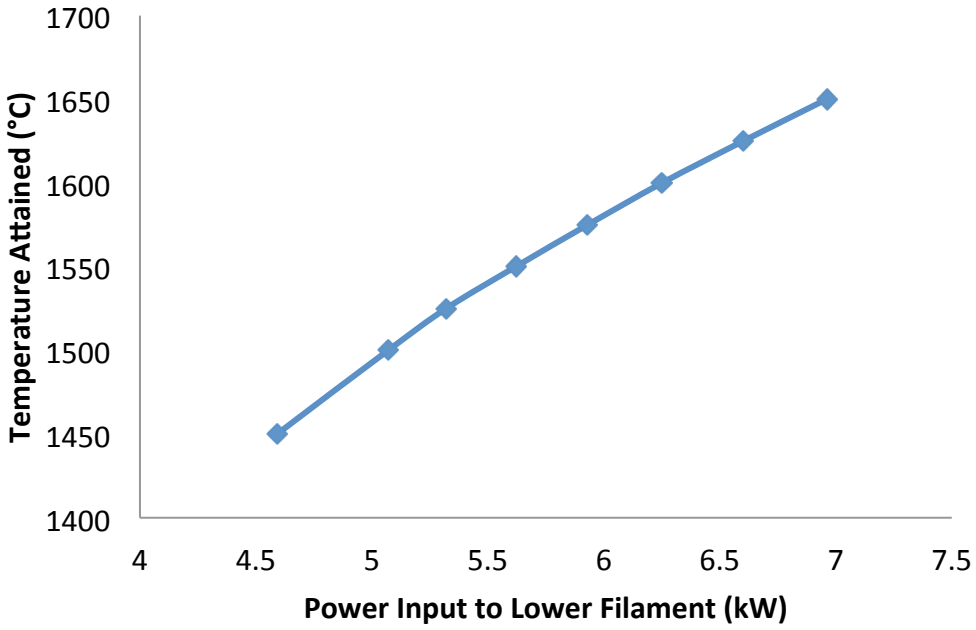

Figure 3.4: Power input to achieve temperatures in the range 1450 °C to 1650 °C using the lower filament only.

3.3 General Growth Procedure

For a typical growth, a SiC samples was first thoroughly solvent cleaned in acetone and ethanol, blow-dried with high-purity nitrogen, and then loaded into the load-lock chamber of the growth equipment. The load-lock was pumped down to a pressure of about 2.2 x 10^{-3} Torr and held for at least 30 minutes before carefully transferring the sample to the growth chamber. The sample was normally left overnight in the pumped-down chamber before growth.

The growth cycle was typically as follows: (1) The chamber was heated up under high vacuum to an intermediate temperature of 750 to 800 °C for 30 minutes to provide an out-gassing clean; (2) The turbo pump to the chamber was then disengaged and the flow of argon to the chamber commenced; (3) After the required argon pressure was attained and stabilized for about 5 minutes, the temperature was ramped up to the required growth temperature at the fastest rate possible for the chamber; (4) After growth, the chamber was cooled down by incrementally reducing the filament power input. Figure 3.5 below illustrate a typical thermal growth cycle for a 30 min growth at 1600 °C.

The average ramp rate up to the growth temperature was about 170 °C per min. (Rate was near 780 °C/min in the first minute). The cool-down rate was about 75 °C/min until a temperature below 1000 °C was attained. Thereafter, the power to the filament(s) was turned off and the specimen was left to cool to room temperature in the chamber.

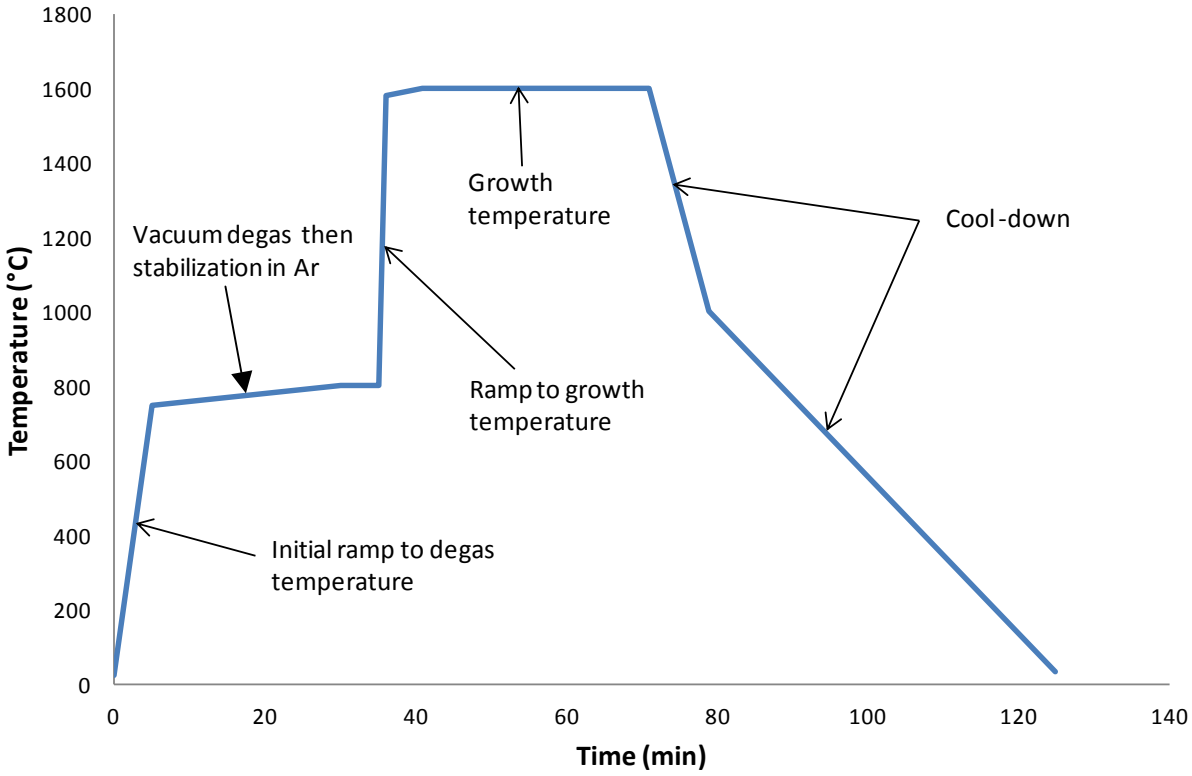

Figure 3.5: Typical heating cycle for a 30 min growth at 1600 °C.

The system was not configured to facilitate *in-situ* hydrogen etch preparation of the wafer growth surface before growths, although this step is considered important by other researchers to remove any polishing damage and to produce an optimized surface morphology of Si-C bilayer steps and terraces to promote step flow growth [31, 37, 39, 58]. Only the high-vacuum out-gassing clean at 800 °C, mentioned above, was carried out.

3.4 Growth Temperatures

Preliminary trial runs indicated that near atmospheric pressure graphene growth was not possible in this chamber at temperatures of 1450 °C or below. So, for this research, most of the growth runs were carried at temperatures

between 1450 °C and 1650 °C. The majority was at or near 1600 °C since preliminary trial runs indicated that this was close to the optimal temperature for monolayer growths at near atmospheric pressure in this chamber.

3.5 Characterization of Graphene

3.5.1 Raman Spectroscopy

Raman spectroscopy was done on the grown samples in order to confirm the presence of graphene and to estimate the number of monolayers grown, based on attenuation of the underlying SiC signal by the graphene film [65, 66]. A Renishaw inVia microscope, utilizing a 488 nm Ar ion laser with a spot size of about 1 μm, was used. Spectrum analysis was done using the associated Wire 3.2 software.

For graphene of high crystal quality, such as that obtained by micromechanical cleavage of graphite, the characteristic Raman spectrum consists of a G peak located at about 1580 cm^{-1} and a 2D peak at about 2700 cm^{-1} [65-67]. The G peak is a result of zone-center in-plane vibration and the 2D peak corresponds to the double resonant excitation of two phonons close to the K point in the Brillouin zone. Both the G and 2D peaks will blue shift to lower wavelength (higher frequency) due to strain and/or doping [66-69]. A defect induced D peak at about 1350 cm^{-1} is also observed in graphene samples with crystalline defects, and the relative intensity of this peak is an indication of the level of defect or disorder in the graphene film.

The Raman spectrum of SiC has several peaks in the 1000 – 2000 cm^{-1} range, and attenuation of the intensity of the L point optical phonon peak at about 1516 cm^{-1} by graphene overlayer has been used as the basis for a method of graphene film thickness estimation, described in Reference 65. In this method, a scaled reference spectrum of the pure (uncoated) SiC substrate is subtracted from the sample Raman spectrum, using the Wire 3.2 spectrum analysis software. The same laser power is used for sample and reference spectra.

The fractional amount, *S*, by which the SiC reference has to be scaled, (so that when it is subtracted from the sample spectrum only the graphene signal is left), is equal to the remaining fraction of the substrate Raman intensity after attenuation by the graphene film. This subtraction is illustrated in Figure 3.6, which is taken from Reference 65.

Using a simple absorbing overlay model, the remaining fraction, *S*, of the substrate Raman signal is given by: $S = e^{-2\alpha t}$, where *t* is the graphene thickness in monolayers, and α is the absorption coefficient of the graphene overlayer. By plotting the logarithm of *S*, ln(*S*), against the thickness, *t*, of graphene films estimated from XPS and TEM, which resulted in a straight, the authors of Reference 65 were able to extracted the value of α as 0.020 ± 0.002 per monolayer of graphene. Hence, using this value for α with the value of *S* obtained from the Wire 3.2 spectrum analysis, the graphene film thickness on samples was estimated.

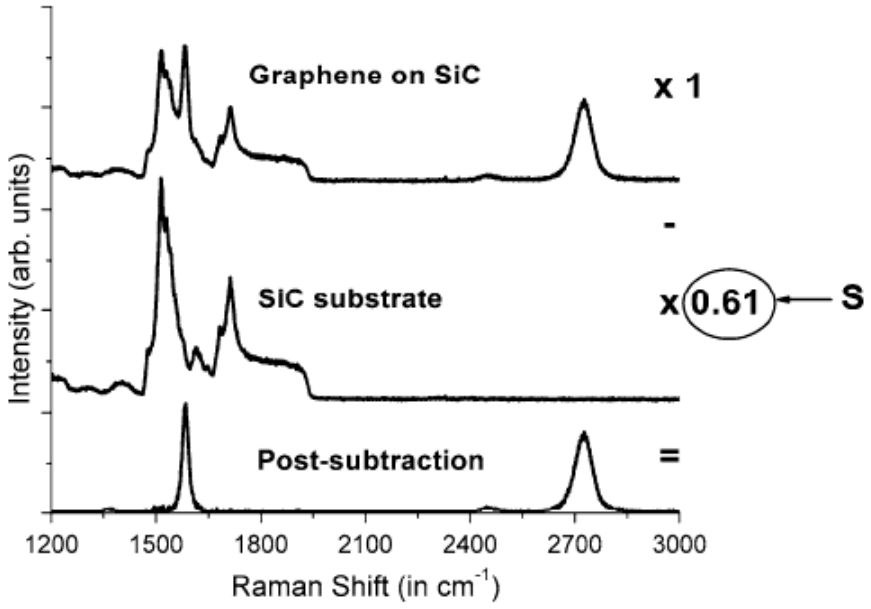

Figure 3.6: Schematic depicting the subtraction procedure by which the Raman signal fraction, *S*, is obtained. (From Reference 65)

3.5.2 Atomic Force Microscopy (AFM)

Atomic force microscopy (AFM) was done using a Veeco Dimension 2100 instrument. Topographical (height) and phase images were obtained using cantilevers in the tapping mode. Resultant images were analyzed using WSxM 5.0 Develop 3.3 image analysis software.

Because about three bilayers of SiC need to decompose to form a monolayer of graphene, areas of graphene growth are topographically lower in height than adjacent areas where no graphene growth has occurred. Also, area of thicker graphene growth, on an initially flat terrace, will be topographically lower than areas of thinner graphene growth. Hence, this is reflected in the topographical

AFM images and height profiles taken on samples. For the AFM topographical images, darker areas are lower in height than lighter areas.

The phase images, which are collected simultaneously with the topographical images, are based on the phase lag between the drive signal and the actual cantilever oscillation. This phase shift is highly sensitive to tip-sample force interaction, which in turn depends on the physical and chemical properties of the surface. Hence, a heterogeneous sample such as one with distinct graphene and buffer layer areas, produces a contrast between the two areas in the AFM phase image.

3.5.3 X-ray Photo-Electron Spectroscopy (XPS)

High-resolution X-ray photo-electron spectroscopy (XPS) was carried out for a series of grown samples using the X-Probe (SSX-100) from Surface Science Instruments (SSI). The system used an Al *K*α X-ray source with a photon energy of 1486.6 eV. Samples were first baked at 300 °C overnight under vaccum in the load-lock before being transferred into the X-ray compartment for scans. The initial bake was necessary to desorb moisture, oxygen and hydrocarbons physisorbed onto the graphene surface. High-resolution scans for C 1s and Si 2p core-level spectra were collected and analyzed using the CasaXPS software. Because the graphene was grown on an insulating SiC substrate, charge compensation using an electron flood gun was necessary during scans. Overcompensation usually occurred resulting in a shift of the spectrum to lower binding energies. The C 1s peak component of the SiC,

which is known to have binding energy of about 283.7 eV, was used to re-adjust the spectrum [36].

3.5.4 Electrical Measurements

Room temperature Hall effect measurements, in a 0.2 Tesla magnetic field were used to determine the carrier type, mobility and sheet carrier density of a series of growths. As necessary, samples were cleaved into 6 mm x 6 mm pieces, and metal contacts were made with indium (In) dots in a conventional van der Pauw configuration. Measurement currents ranged from 0.3 to 3 mA.

3.5.5 Transmission Electron Microscopy of Film

High-resolution transmission electron microscopy (HRTEM) was used to evaluate the structure of the graphene film from a typical monolayer growth at 1600 °C. For these measurements, the graphene film was transferred from the SiC substrate unto standard perforated carbon film TEM grids by a specially developed process [70, 71]. This represents the first time that epitaxial graphene grown on SiC has been transferred and imaged by TEM as a suspended film, in plan view. Previous TEM studies involved cross-sectional imaging of multilayer graphene still attached to the SiC substrate [53].

It is difficult to decouple as-grown epitaxial graphene from the SiC substrate due to the presence of an intermediate carbon-rich buffer layer in which about 30% of the carbon atoms are covalently bonded to surface Si atom of the SiC substrate, and which is responsible for the azimuthal ordering of graphene on

SiC(0001) [36, 44]. Furthermore, semi-insulating SiC is a chemically stable dielectric which is not easily etched. Hence, the sample was subjected to hydrogen intercalation to decouple the buffer layer from the SiC substrate before using a special two step process to transfer the graphene from the SiC substrate to the TEM grids. The hydrogen intercalation was carried out at atmospheric pressure by heating the as-grown graphene sample to 1050 °C in pure hydrogen for about 1½ hour. Hydrogen intercalation has been shown to convert monolayer film to a bilayer film [44].

To transfer the graphene from the SiC substrate to the TEM grids, 100 nm of Au was first deposited on the sample by e-beam evaporation followed by spin coating with PMMA. Using sharp tweezers, the graphene/Au/PMMA trilayer was mechanically peeled off and placed on a Si substrate. The PMMA was then removed with acetone and the Au was chemically etched. In the second stage, the bubbling method described in Reference 70 was used to transfer the graphene film from the Si to TEM grids for analysis.

Transmission electron microscopy was carried out at 80 kV accelerating voltage on a Joel JEM-2010F TEM retrofitted with two spherical aberration (Cs) correctors to enable high-resolution, low-voltage imaging.

3.5.6 Elevated Temperature Oxidation Study

A limited number of multilayer graphene films, grown under high vacuum conditions, were used to assess the atmospheric pressure oxidation (etching)

behavior of graphene when heated in pure oxygen in the 200 – 600 °C temperature range. The same oxygen flow rate and duration of oxidation (15 min) was used for all the samples. Raman spectroscopy was used to determine the number of graphene layers on each sample before and after each oxidation run (See section 3.5.1).

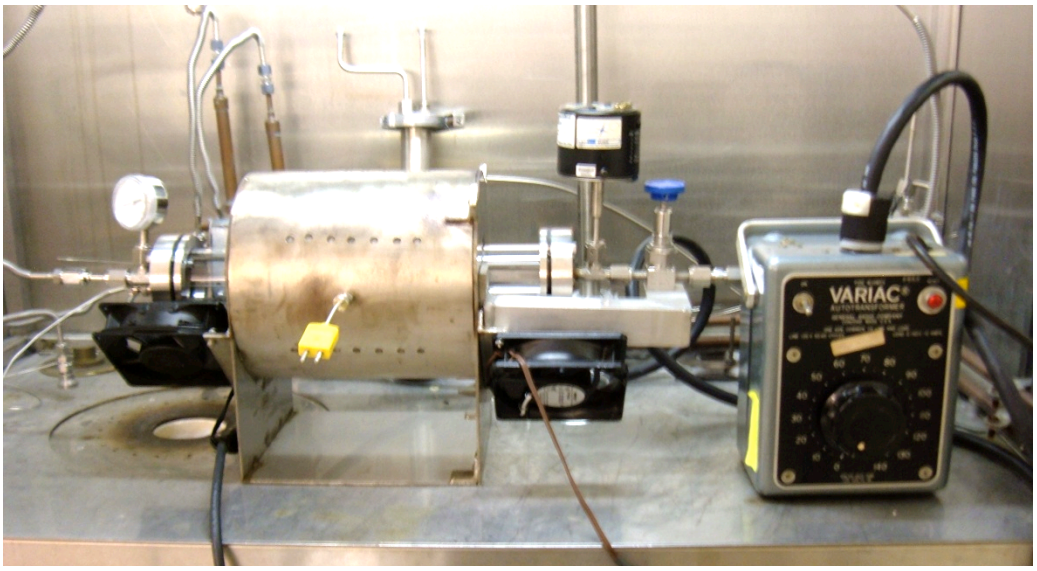

Figure 3.7: Horizontal tubular furnace used for oxidation etching study. The thermocouple in the foreground was not used. A thermocouple was inserted directly into the quartz tube through the end cap on the left.

An electrical resistance heated horizontal tubular furnace, equipped for gas flow, and with an inserted thermocouple for temperature measurement, was used (See Figure 3.7, above). The specimen was placed in a quartz boat and loaded into the middle region of the furnace. The furnace tube was first purged with high-purity nitrogen at room temperature before being heated up to the desired oxidation temperature with the nitrogen continuously flowing. Once

the oxidation temperature was reached, the nitrogen flow was switched off and the flow of high-purity oxygen switched on. After the 15 min oxidation time, the gas flow was switched back to nitrogen for cooling the sample to room temperature.

CHAPTER 4

RESULTS AND DISCUSSION

4.1 Effects of Growth Temperature

4.1.1 Effect on Graphene Growth

This research was aimed at using the modified CVD chamber at the Cornell University Wide-Bandgap-Semiconductor Laboratory to optimize growth of uniform large-area epitaxial graphene (EG), of a monolayer thickness and greater, by the thermal decomposition of 6H-SiC(0001), and to characterize the graphene. The temperature regime required for growths is discussed below.

No epitaxial graphene growth was obtained at 1450 °C or below with near atmospheric pressure, although macroscopic step bunching was observed. AFM images in Figure 4.1 show step bunching for a run at 1450 °C, but the Raman spectrum in Figure 4.2 showed neither G nor 2D peaks. Also, the surface of the terraces was very smooth as compared to the roughening that usually accompanies graphene growth. However, XPS spectrum for this run definitely indicated the presence of a $(6\sqrt{3} \times 6\sqrt{3})R30°$ carbon-rich buffer layer (Figure 4.3). The XPS spectrum was best fitted with two components with peaks at binding energies of 283.7 eV and 285.5 eV, corresponding to the C1s peaks for the SiC substrate and the buffer layer, respectively [36].

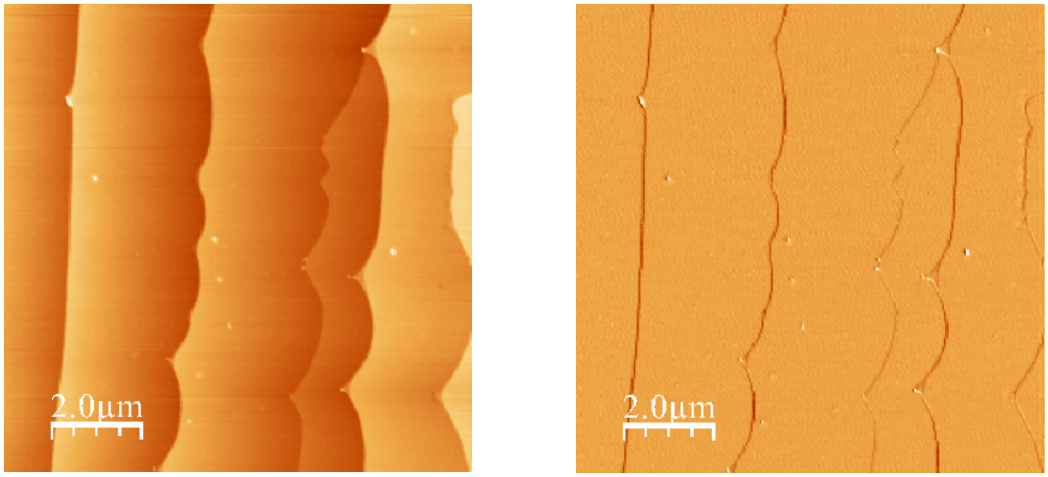

(a) Topographical image (b) Phase image

Figure 4.1: AFM (a) topographic and (b) phase images of a sample grown at 1450 °C. Macroscopic step bunching is observed but only a buffer layer formed.

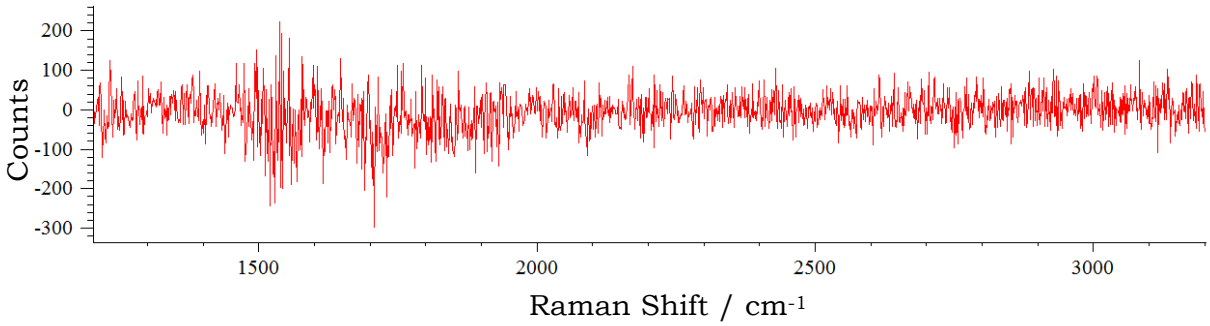

Figure 4.2: Raman spectrum of a 1450 °C run showing background noise only. The absence of the G and 2D peaks indicates that no graphene growth occurred at 1450 °C.

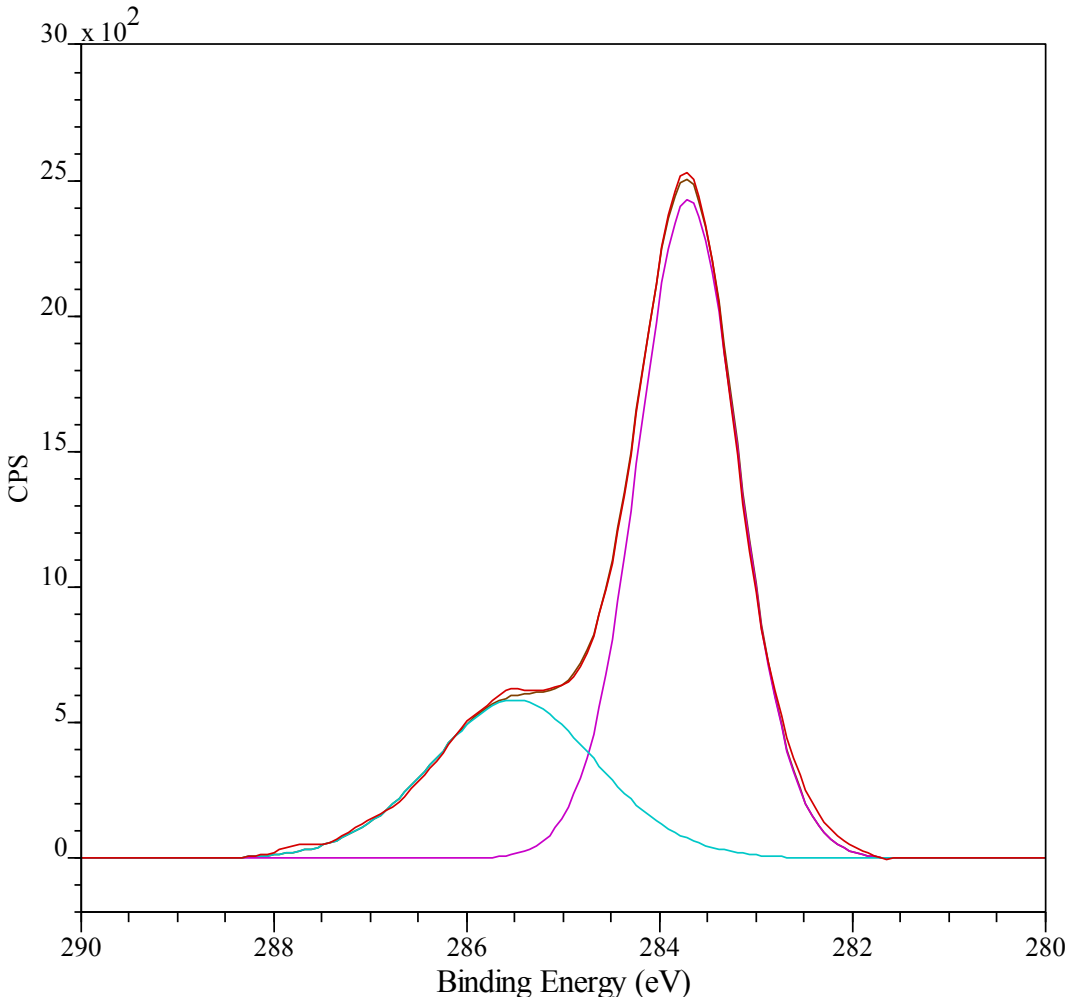

Figure 4.3: XPS C1s spectrum for growth at 1450 °C. The spectrum (red) is best fitted with two components (purple and blue) with peaks at binding energies of 283.7 eV and 285.5 eV, corresponding to the C1s signal from the SiC substrate and the buffer layer. This shows that only the buffer layer was formed.

Limited graphene growth was obtained at 1500 °C. The Raman spectra for up to 45 min growth indicated less than a monolayer of graphene, and AFM revealed that the graphene was mainly located at step edges (Figures 4.4 and 4.5). The 45 min growth also showed that, apart from the step edge graphene growth, nucleation and growth of graphene was also occurring at defect points

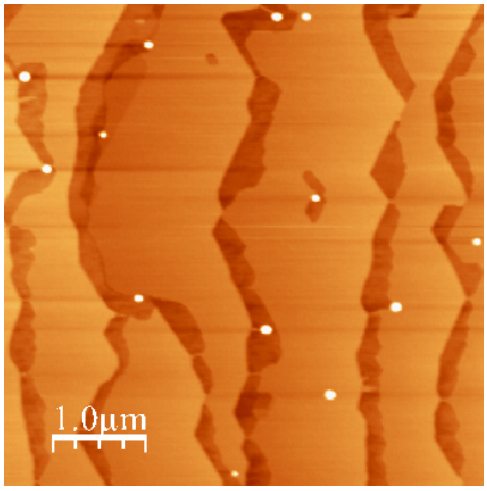

(a) Topographical image

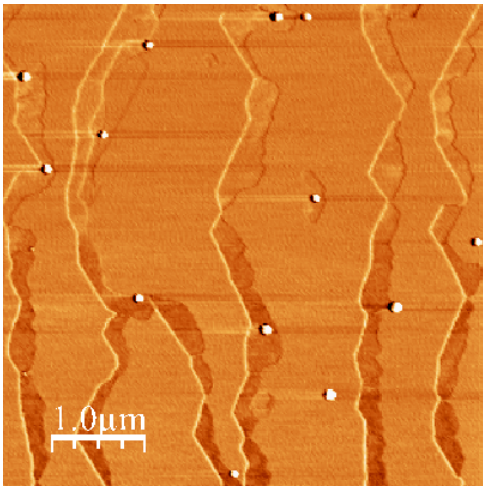

(b) Phase image

Figure 4.4: AFM of growth at 1500 °C for 15 min. Graphene has only begun to form at the step edges. The terraces are expected to be covered with the (6√3 x 6√3)R30° buffer layer. (The white particles are dust artefacts)

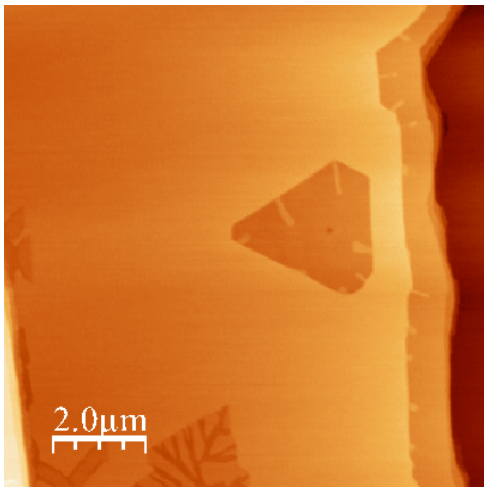

(a) Topographical image

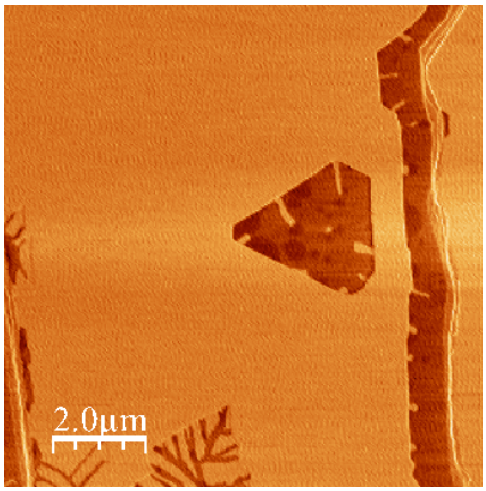

(b) Phase image

Figure 4.5: AFM of growth at 1500 °C for 45 min. The phase contrast in (b) clearly shows that graphene (dark brown phase) has only started to grow at the step edges and at defect points on the terrace (triangular features). Most of the surface (light brown phase) is the (6√3 x 6√3)R30° buffer layer.

on the step terraces (Figure 4.5). This is discussed further in Section 4.3.3. The terraces were also relatively wide at 8 – 9 μm.

Fifteen (15) minutes growth at 1550 °C resulted in increased graphene growth (compared to growth at 1500 °C), but still growth was incomplete across the terraces. Most of the surface still consisted of the (6√3 x 6√3)R30° buffer layer (Figure 4.6). Increasing the growth time to 30 min resulted in monolayer growth across the SiC surface, however the step edges were rough (undulating) and the terraces were very narrow (less than 2 μm) (see Figure 4.7). Forty-five (45) minutes growth resulted in significantly larger terraces (about 8 μm wide) and 1 – 2 graphene layer growth across the terraces, with only a scattering of untransformed islands of SiC and/or buffer layer (light patches) (Figure 4.8). Increasing the growth time beyond 45 min likely would have resulted in complete transformation of these islands.

Height profiling revealed that most of the islands were close to 4.2 Å (Figure 4.9). This is the difference between the three bilayers of SiC (7.5 Å), that need to decompose to form one layer of graphene, and the thickness of a graphene layer (3.3 Å). This indicates that the surface adjacent to the islands was indeed monolayer graphene.

Raman spectrum for the 1550 °C, 45 min growth is shown in Figure 4.10. The strong G-peak and 2D peaks located at 1589 cm^{-1} and 2719 cm^{-1} confirm the presence of graphene. A small disorder-induced D-peak at about 1353 cm^{-1} indicated only a small defect level in the graphene film, probably mostly due to

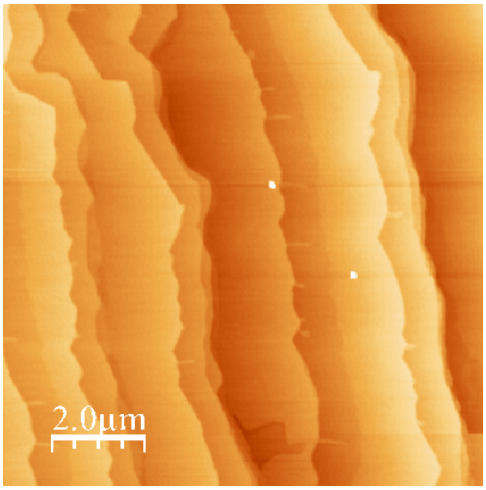

(a) Topographical image

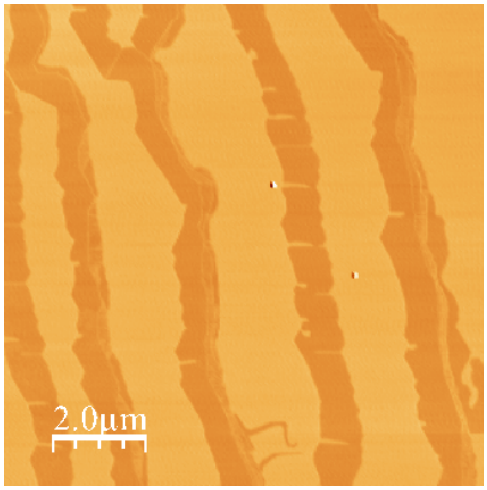

(b) Phase image

Figure 4.6: AFM images of a 1550 °C, 15 min growth showing graphene growth adjacent to the step edges that has not progressed across the terraces, which remain mostly buffer layer terminated SiC.

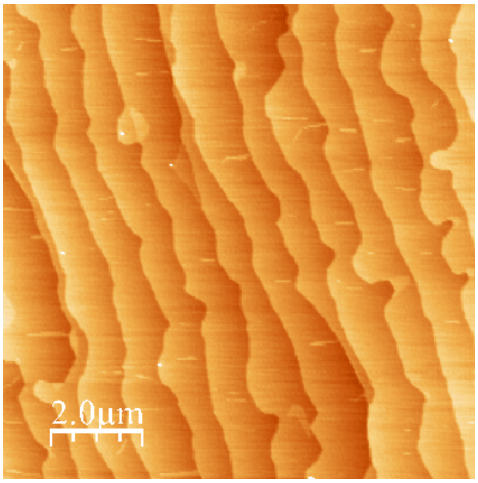

(a) Topographical image

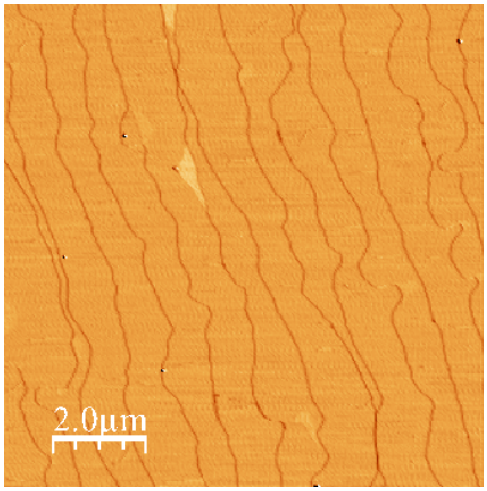

(b) Phase image

Figure 4.7: AFM images of a 1550 °C, 30 min growth showing complete growth of graphene across the terraces. The terraces are however narrow (< 2 µm) and the step edges are rough (undulating).

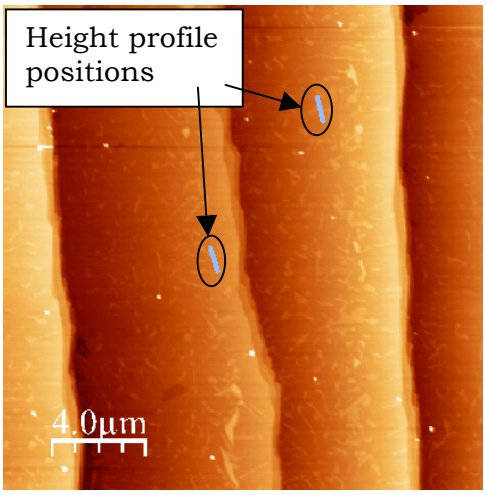

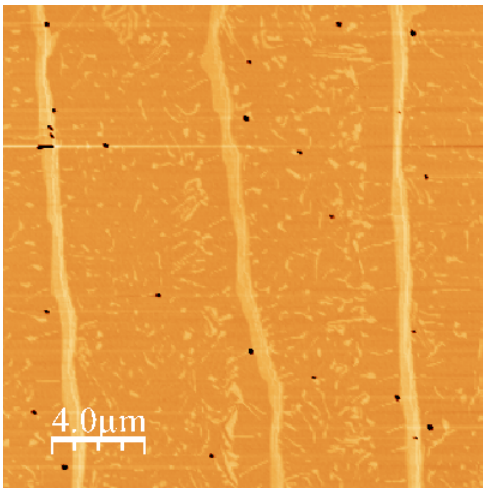

(a) Topographical image (b) Phase image

Figure 4.8: AFM images of a 1550 °C, 45 min growth. Growth of 1 – 2 layers of EG has occurred across the terraces, but there are scattered islands of untransformed SiC/buffer layer. The terraces are significantly wider than for the 30 min growth shown in Figure 4.7, above. The height profiles across two typical islands at positions indicated in (a) are given below.

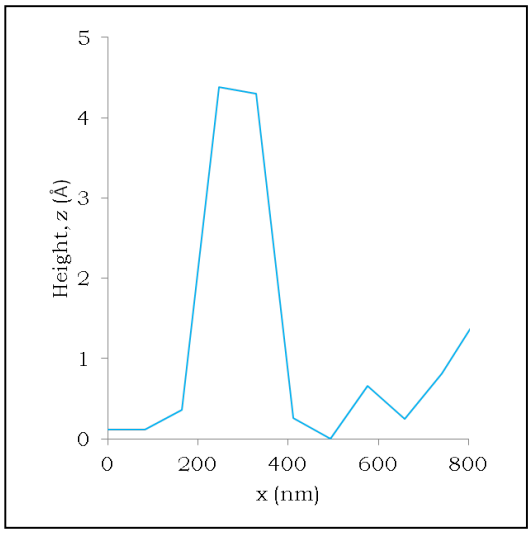

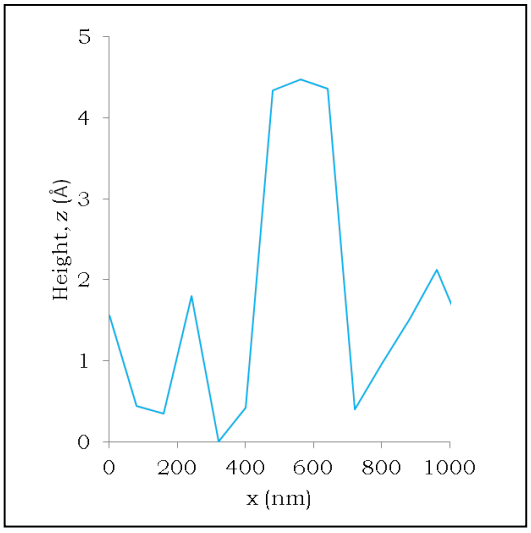

Figure 4.9: Height profiles across untransformed SiC/buffer layer islands shown in Figure 4.8 (a) above. The heights were close to 4.2 Å, which is the difference between the three bilayers of SiC (7.5 Å) that decompose to form one layer of graphene (3.3 Å).

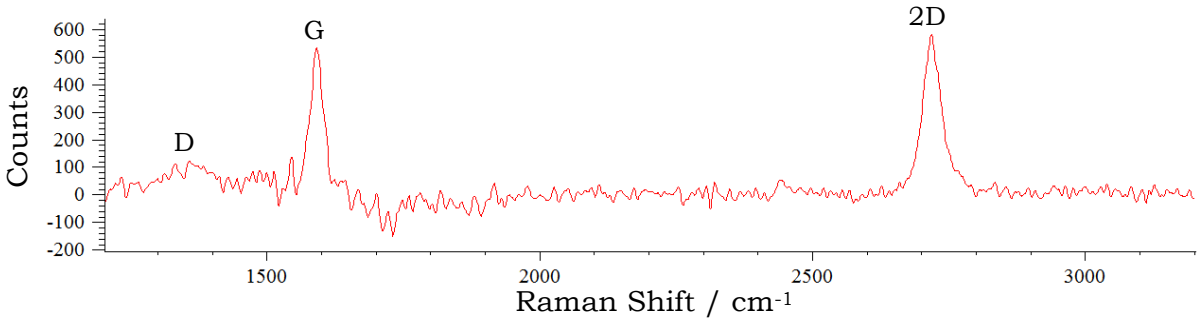

Figure 4.10: Raman spectrum of 1550 °C, 45 min growth showing the distinct G and 2D peaks of graphene. The low intensity D-peak at 1353 cm^{-1} indicates a small level of defect.

the scattered SiC/buffer layer islands (See Section 4.2).

For 15-minute growths at1600 °C, Raman spectroscopy indicated that at least one complete monolayer of graphene was usually grown. However, AFM images generally indicate strips of one or two extra layers adjacent to step edges (Figure 4.11). Increasing the growth time to 30 minutes resulted in 1.5 – 2.5 layers of EG growth. Figure 4.12 shows the AFM images of a 1600 °C, 30 min growth which had reasonably uniform bilayer growth but with irregular step edges and relatively narrow terrace width, similar to what is obtained for 30 minutes growths at 1550 °C (Figure 4.7). Growth at 1600 °C for 45 min produced 2 – 3 layer graphene growth with wider terrace and straighter step edges than for the 30 min growths (Figure 4.13).

As expected, for growths within the 1450 °C to 1650 °C temperature range, the general trend was for increased number of EG growth layers with increasing

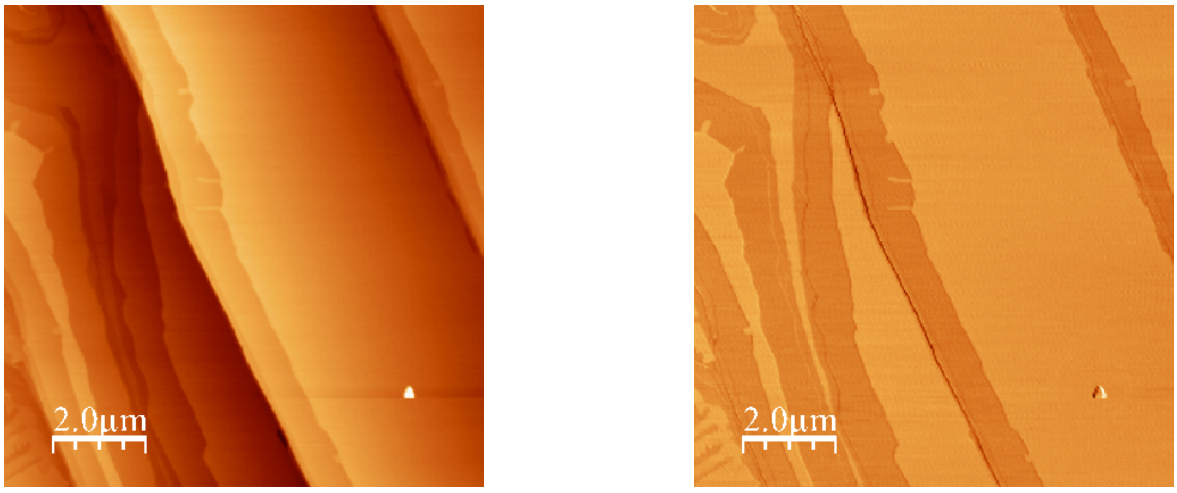

(a) Topographical image (b) Phase image

Figure 4.11: AFM of a 1600 °C, 15 min growth. This along with Raman spectroscopy indicated a single layer EG across the terraces with an extra layer of graphene forming adjacent to step edges as narrow strips.

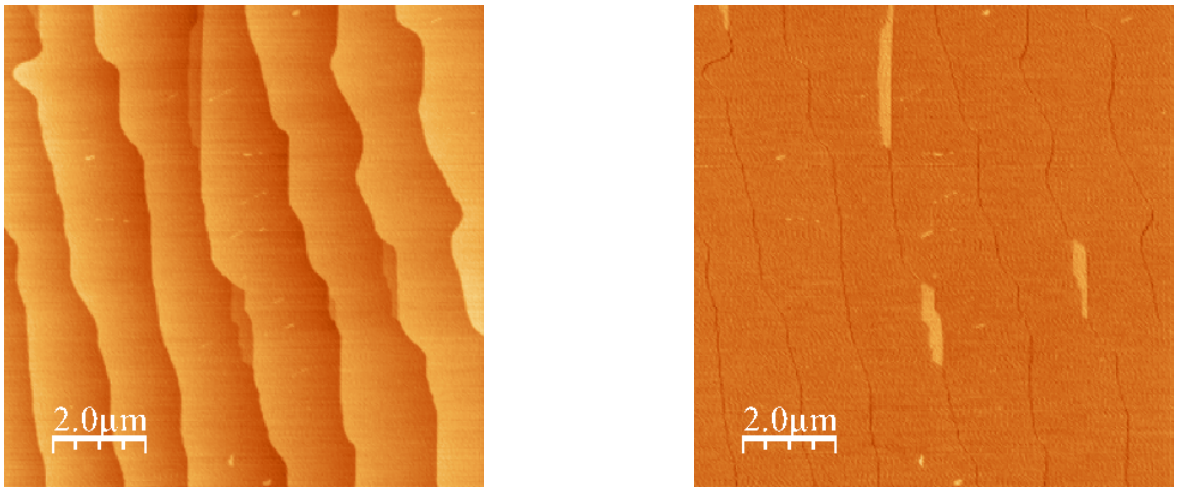

(a) Topographical image (b) Phase image

Figure 4.12: AFM of a 1600 °C, 30 min growth. This along with Raman spectroscopy data indicated almost uniform growth of bilayer EG. The steps edges were irregular and the terraces narrow relative to 15 min and 45 min growths.

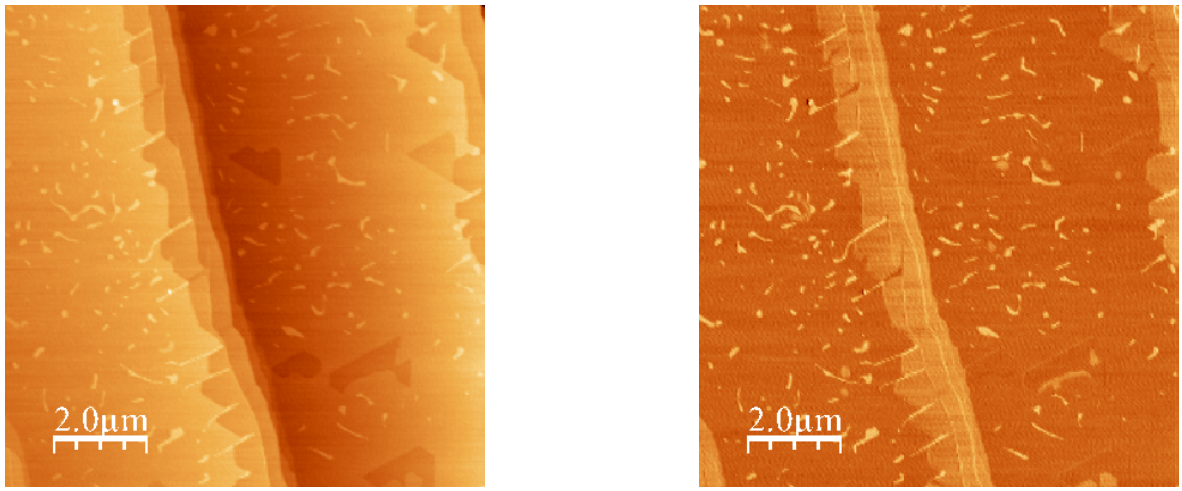

(a) Topographical image (b) Phase image

Figure 4.13: AFM of 1600 °C, 45 min growth. Additional layer growth can be seen at the step edges, and there is a distribution of untransformed SiC/buffer layer islands across the terrace. Raman spectroscopy indicated 2 – 3 layers.

temperature and time of growth. Figures 4.14 gives plots of average number of layers with temperature for 15 min, 30 min and 45 min growths, and Figure 4.15 gives average number of layers as a function of time at temperatures of 1450 °C , 1500 °C , 1550 °C and 1600 °C.

It should be pointed out that, the unique mode of graphene growth by the thermal decomposition of the substrate to release C atom to form graphene layers and with evaporation of the Si atoms, results in a self-limiting effect on the graphene growth. As soon as the buffer layer forms, it becomes a barrier for escape of Si atoms, and as graphene layers form, which may cover even step edges, the escape of Si atoms is impeded even further. The Si atoms can only

escape at defect points in graphene sheets or at uncovered step edges. Hence, as the sheet gets thicker so will be an expected increase in the self-limiting effect. Because of this, an Arrhenius-type rate of graphene growth with temperature was not immediately obvious from the plots of average number of layer growth versus temperature (Figure 4.14). However, an Arrhenius-type relation between growth rate ($\Gamma_{growth)}$ and temperature would be expected. That is: $\Gamma_{growth} = Ae^{-E_A/kT}$, where A is the pre-factor, E_A is the activation energy, k is the Boltzmann constant, and T is the temperature in Kelvin.

To extract the activation energy for the growth regime, growth rates for 1500 °C, 1550 °C and 1600 °C were obtained from the slopes of the plots of average number of layers versus growth time (Figure 4.15). The natural log of these is plotted against 1000/T in Figure 4.16, and from the slope of this plot an activation energy of approximately 3.1 eV was extracted.

It was observed that for the relatively smooth and uniform growths, which presumably would have progressed by simple step flow, the step heights were predominantly about 0.75 nm or three-bilayer heights. This is consistent with the observation that some step terraces are more thermodynamically stable than others so decomposition of the SiC surface and step bunching would occur so as to favor steps terraces with the lowest surface energy [33, 58, 62, 63]. See also Section 2.4.1.

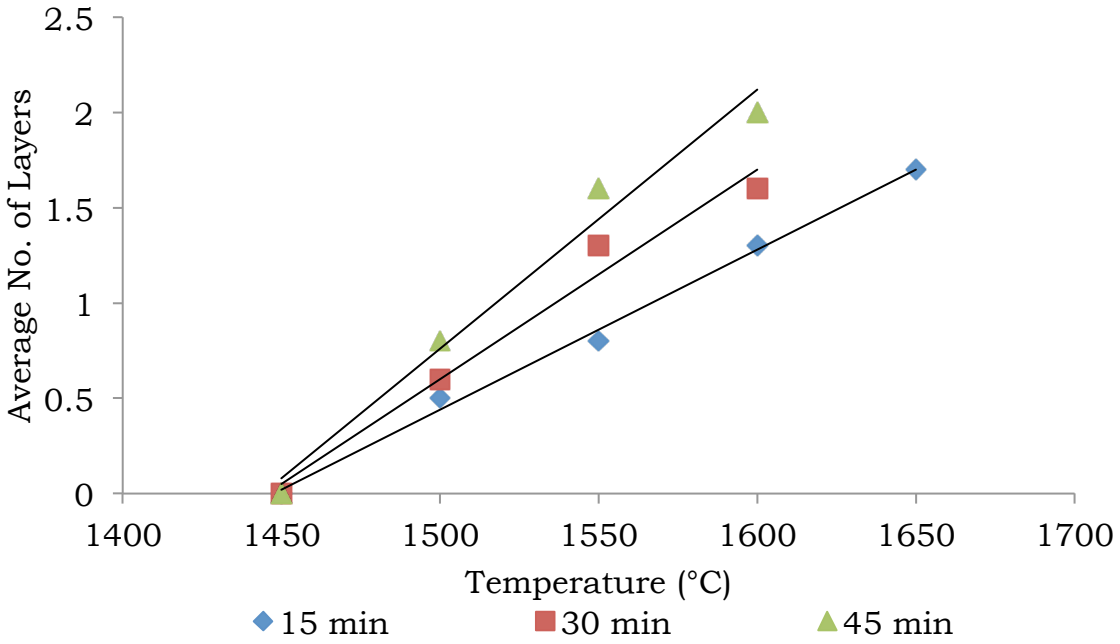

Figure 4.14: Plots of average number of graphene layers grown as a function of temperature for 15 min, 30 min and 45 min growth times. The plots show the general trend of increased growth with increase in both temperature and time of growth.

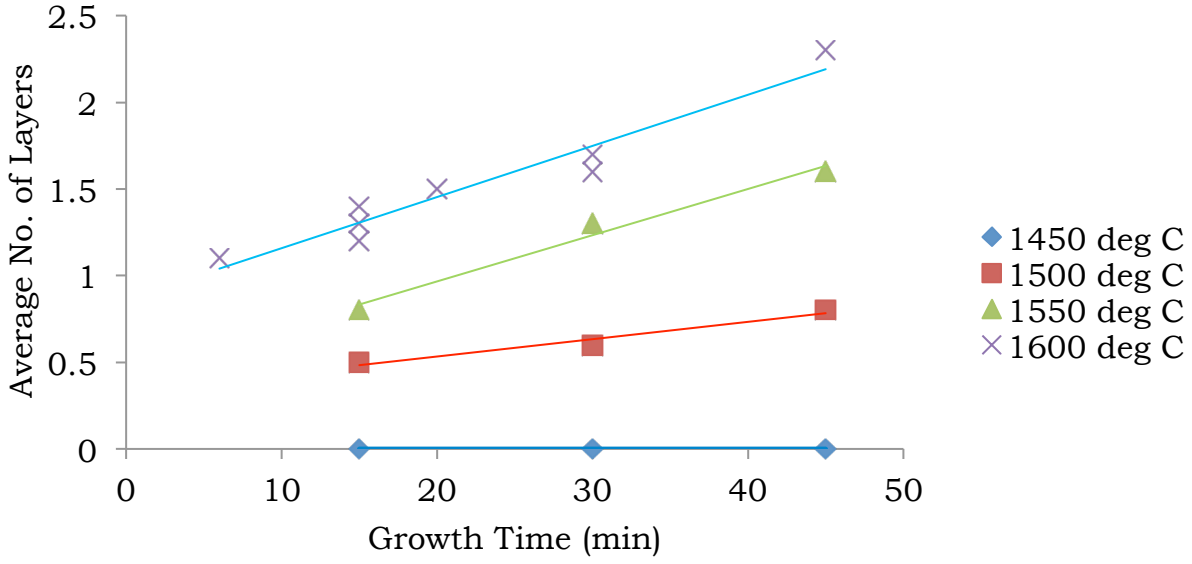

Figure 4.15: Plot of average number of layers grown as a function of growth time for 1450 °C, 1500 °C, 1550 °C and 1600 °C growths, showing the general trend of increase in EG growth with growth time.

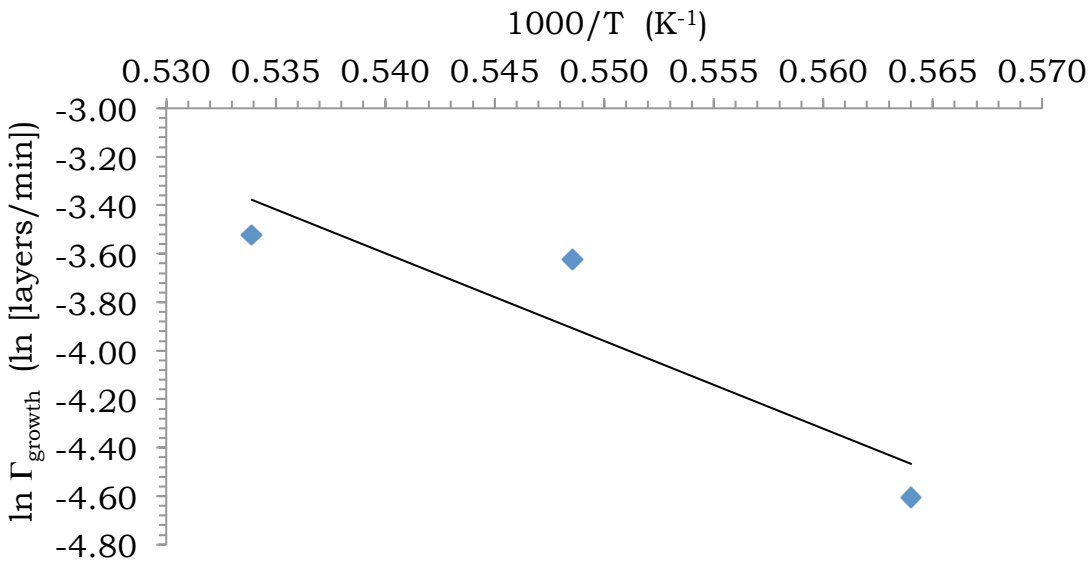

Figure 4.16: Plot of natural logarithm of growth rate (ln Γ_{growth}) versus 1000/T. Growth rates obtained from slope of plots of average number of layers versus growth time for 1500 °C, 1550 °C and 1600 °C (Figure 4.15).

4.1.2 Deep-Pit Formation

It was found that, at temperatures above 1650 °C, deep pits started to form on the surface of the SiC samples, and that the density of pits showed a clear trend of increasing with temperature. AFM images in Figure 4.17 show the increase in pit density with temperature for samples from the same wafer which were grown for the same time. A sample grown at about 1750 °C for 5 min is also shown with a high density of pitting. The type of pitting observed here did not appear to be the same as those described by Hannon and Tromp as forming due to pinning of decomposing surface steps by domain of buffer layer and migration of steps through gaps in the buffer layer at step edges [72].

The increase in pit density with temperature suggests that vacancy point defects, and not dislocations, are the likely cause. The fraction (*f*) of vacancy defects increases exponentially with temperature given by:

$$f = exp\left(-E_f/k_B T\right)$$

where E_f is the formation energy, k_B is the Boltzmann constant, and T the absolute temperature [73].

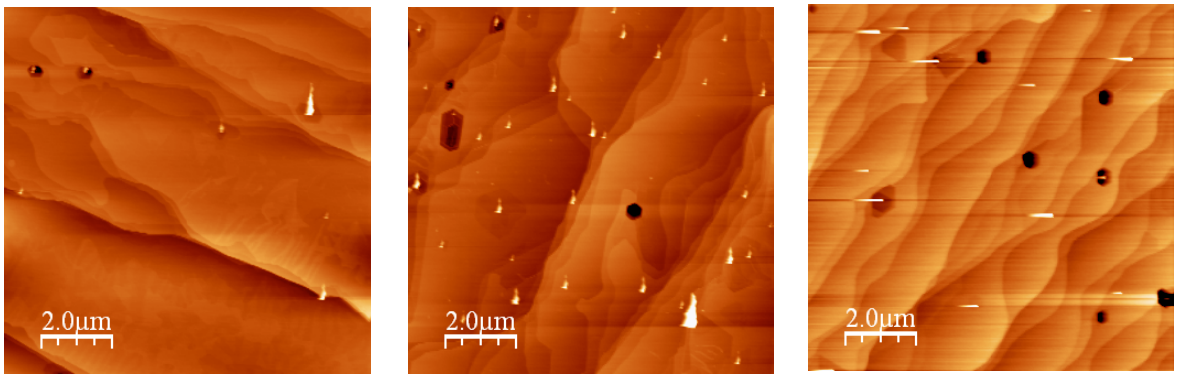

1675 °C, 10 min 1690 °C, 10 min 1705 °C, 10 min

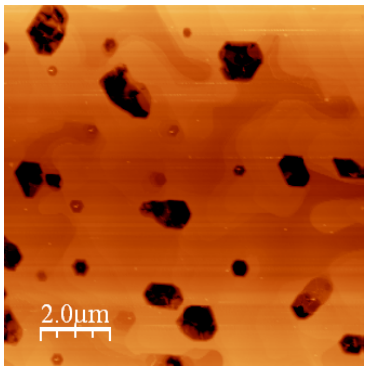

1750 °C, 5 min

Figure 4.17: Showing formation of deep pit at high temperature and the increase in pit density with increasing temperature.

Triangular shallow pits formed at lower temperatures, (described later in Section 4.3.3), are likely to originate from these same point defects.

The formation of deep-pits at high temperatures puts a limit to how high a temperature EG growth can be carried out. Also, the electrical results discussed in Section 4.5 show that this type of pitting results in relatively low electron mobility.

4.2 Raman Spectroscopy

It was observed that, for the epitaxial graphene grown for this research, both the Raman G and 2D peaks were blue shifted with respect to that of graphene obtained by micromechanical cleavage (See Section 3.5.1). For example, for the 1600 °C growths, the mean upward shifts were 16 cm^{-1} and 30 cm^{-1} for the G and 2D peaks, respectively. This shift to higher phonon frequencies is consistent with other research findings, and is explained as being mainly due to compressive strain developed in EG graphene film due to differential contraction between the film and substrate in cooling from the growth temperature. There is also a smaller contribution from the effect of the electron doping of the graphene due to interaction with the buffer layer/SiC interface [66-69].

The defect-induced D peak, positioned at about 1350 cm^{-1}, was relatively small or non-existent for the monolayer and few-layer growths done at 1600 °C and

above. This indicated that almost defect-free, uniform large-area graphene films were successfully grown.

4.3 XPS Characterization

A series of samples were characterized by X-ray photo-electron spectroscopy (XPS). Scans were done to obtain high-resolution core-level C 1s and Si 2p spectra. The observed binding energy is a function of the species and the nature of the local chemical bonding. Small, but well defined, shifts in binding energy are used to identify the local bonding structure/environment.

The C 1s spectrum of EG graphene on SiC consists of three components; a component near 283.7 eV from the bulk SiC substrate, a component near 284.8 eV from the EG graphene layer, and a component near 285.5 eV from the $(6\sqrt{3} \times 6\sqrt{3})R30°$ surface reconstructed carbon buffer layer [36]. Using the CasaXPS software, the spectra of the scanned samples were fitted with these components, providing a means to compare compositional differences. Figure 4.18 shows typical C 1s spectra for 15 min growth at (a) 1500 °C and (b) 1600 °C, with fits to the constituent components. The letter "B" is used to designate the buffer-layer spectrum component, "G" the graphene component, and "S" the component from the bulk SiC. Comparing the 1500 °C growth to 1600 °C, the increase in the graphene C 1s signal and the attenuation of both the buffer-layer and SiC C 1s signals indicated increased graphene growth.

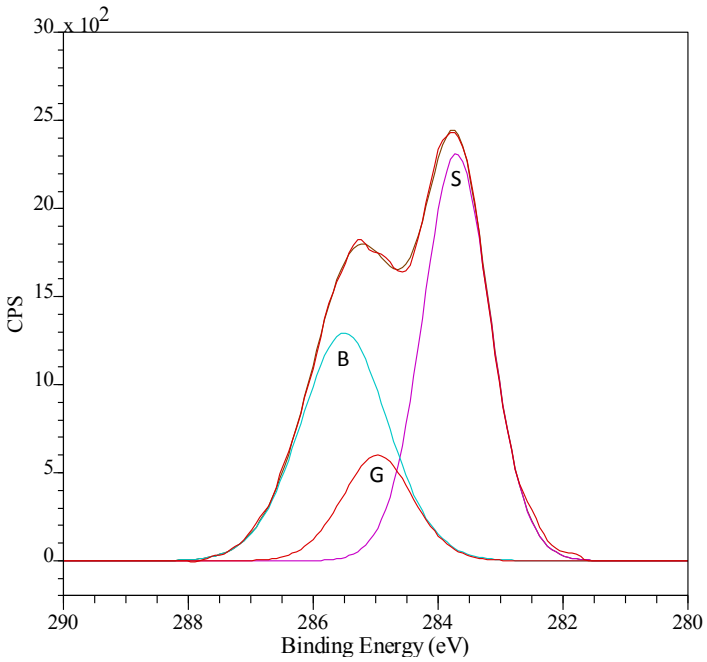

(a) 1500 °C, 15 min

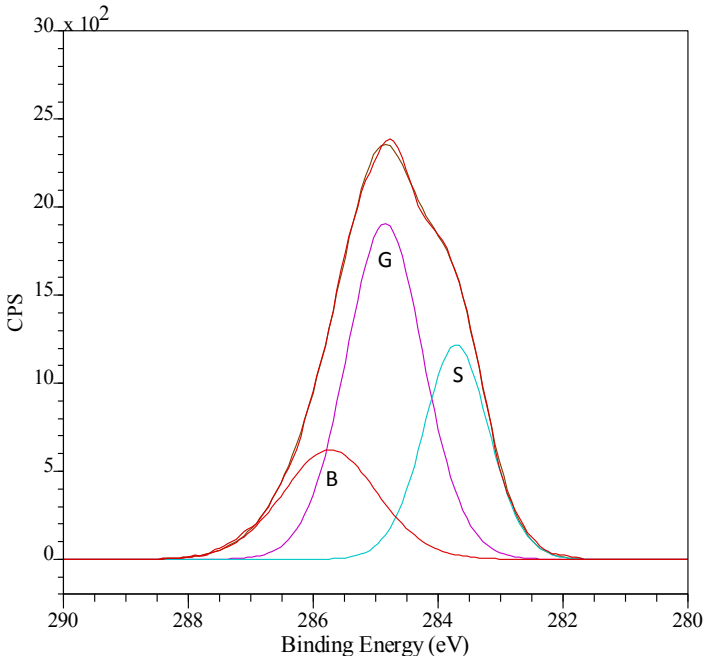

(b) 1600 °C, 15 min

Figure 4.18: XPS C 1s spectra for 15 min growth at (a) 1500 °C and (b) 1600 °C, with the constituent components spectra fitted. "B" designates the buffer-layer spectrum component, "G" the graphene component, and "S" the component from the bulk SiC.

High-resolution X-ray photo-electron spectroscopy on a set of samples, grown over a temperature range of 1450 – 1650 °C for growth times of 15 – 45 min, confirmed a clear layer thickness dependence on growth temperature and growth time. Figure 4.19 shows overlays of XPS high-resolution C 1s spectra for 15 min growth at 1450, 1500, 1550, 1600 and 1650 °C.

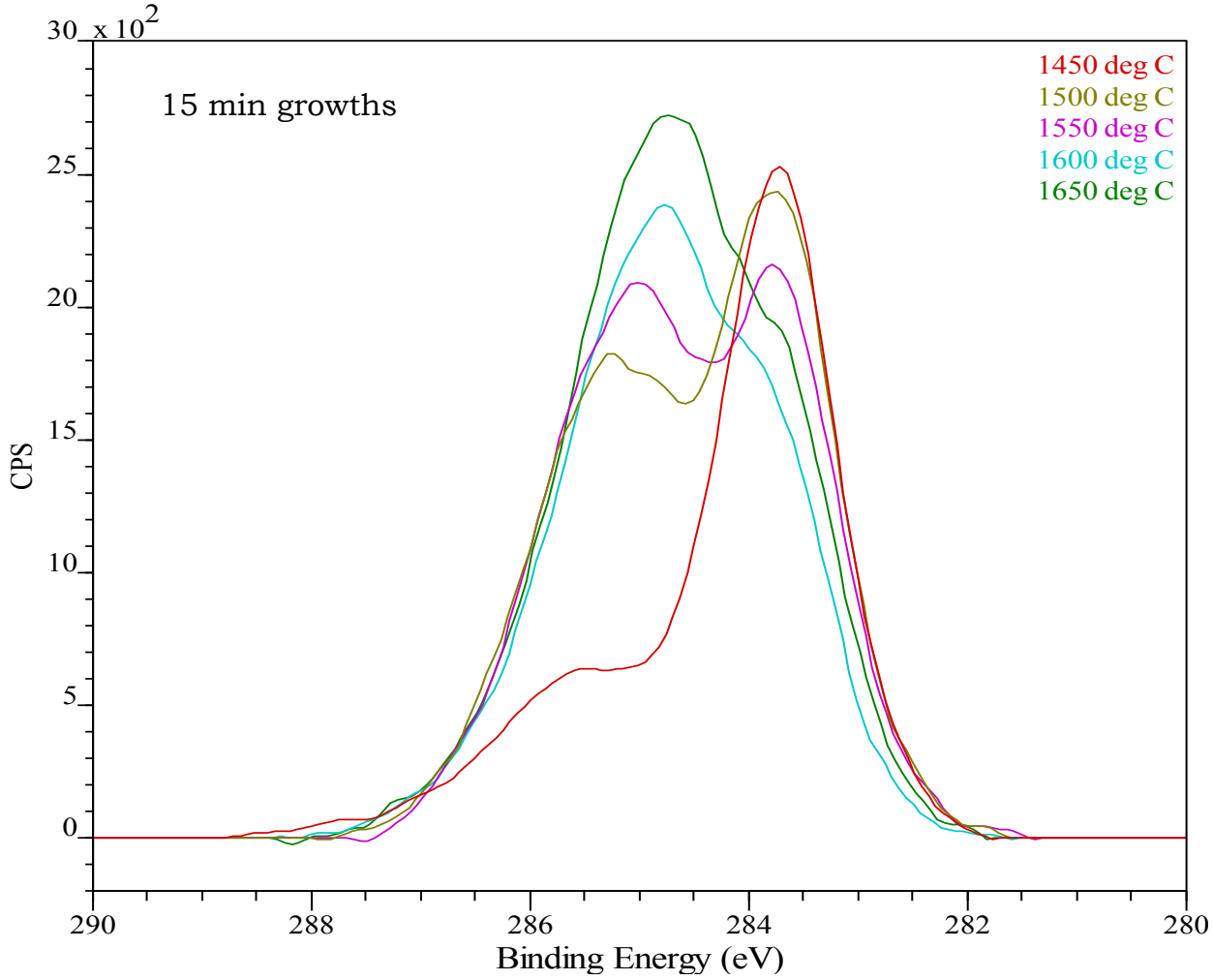

Figure 4.19: Overlay of XPS high-resolution C 1s spectra for 15 min growth at 1450, 1500, 1550, 1600 and 1650 °C. The spectrum for the 1450 °C growth is composed of buffer layer and SiC C 1s components only (See Section 4.1.1 and Figure 4.3). Note the progressive rise in intensity of the graphene C 1s signal (284.8 eV) and progressive attenuation of the intensity of the SiC C 1s signal (283.7 eV) with increasing temperature.

The spectrum for the 1450 °C growth was found to be composed of buffer layer and the bulk SiC C 1s components only (See also Section 4.1.1 and Figure 4.3). The overlaid spectra shows the progressive rise in intensity of the graphene C 1s signal (peaking towards about 284.8 eV), and progressive attenuation of the intensity of the SiC C 1s signal (at about 283.7 eV) with increasing temperature. This is consistent with the increase layer growth of graphene with temperature.

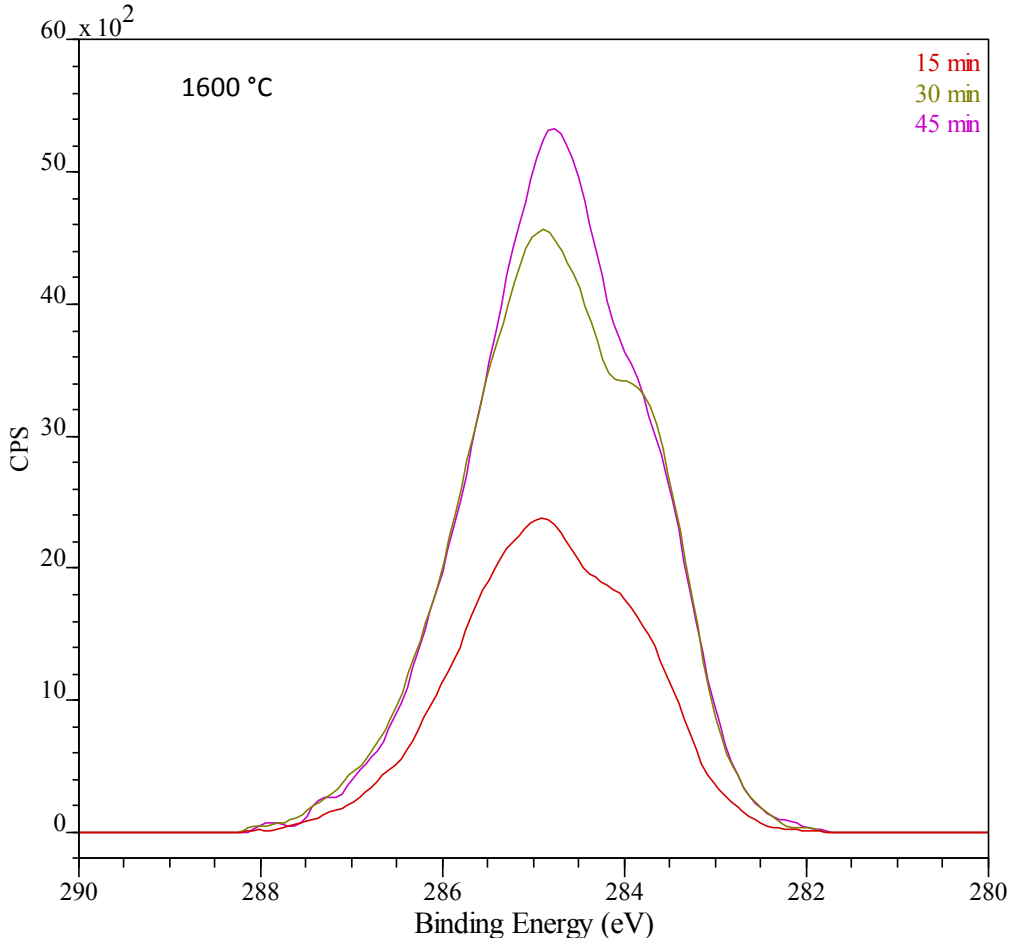

Figure 4.20: Overlay of high-resolution XPS spectra of samples grown at 1600 °C for 15, 30 and 45 min. The peak due to the graphene C 1s signal increases with growth time consistent with increased EG thickness.

Figure 4.20 shows an overlay of high-resolution XPS C 1s spectra for 1600 °C growths for 15, 30 and 45 min growth times. The increase in EG layer thickness with increase in time of growth is evidenced by the progressive increase in the intensity of the graphene component peak with time.

4.4 Growth Features and Their Effects

Several growth features were observed which had significant effects on the regularity of step flow and, as a consequence, on the growth of uniform high-quality graphene. It is important to understand how growth features contribute to, or hinder, the formation of a uniform continuous graphene film, and to understand the mechanisms by which these occur since the ability to grow uniform large area graphene by the thermal decomposition of SiC will ultimately determine whether or not graphene growth by this route will fulfill the promise for graphene electronics. The formation of deep rounded pits at high temperature was already discussed in section 4.1.2. Other important features revealed by AFM are discussed below.

4.4.1 Arrow-like Incursions

"Arrow-like" growth features were at times observed where etching dents with arrow-head shaped leading edge penetrated terraces (See Figure 4.21). These incursions ultimately broke up terraces into smaller irregular domain sizes.

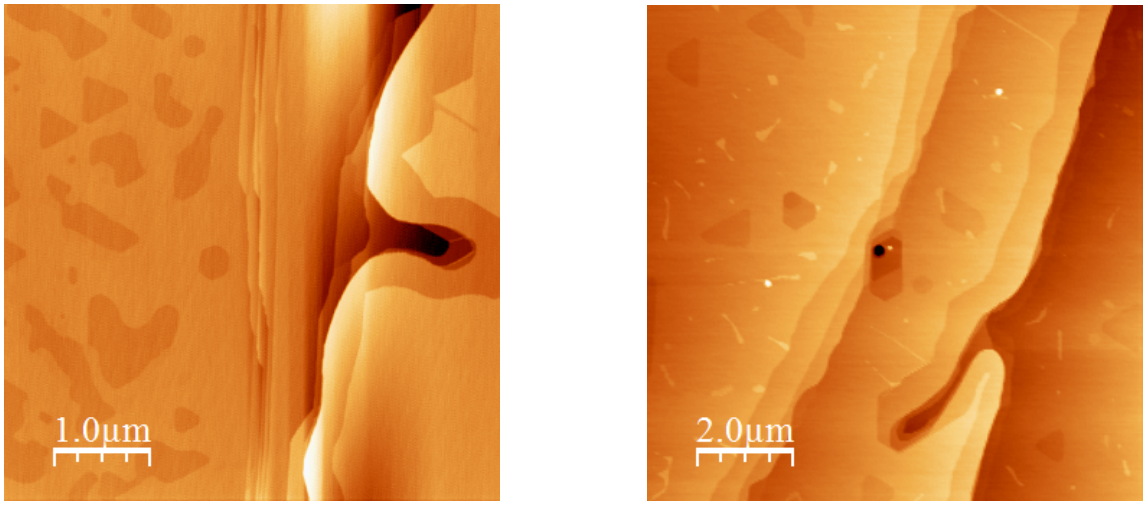

(a) (b)

Figure 4.21: AFM images showing incursion of "arrow-like" growth features into terraces. These cause new step edges to be formed at an angle to the original step edge and created irregular terrace geometries.

Ohta *et al* proposed that arrow-like growth features occur by a growth mechanism that depends strongly on the initial surface morphology and carbon diffusion that governs the spatial relationship between SiC decomposition and graphene growth [64]. The decomposition of about three bilayers of SiC is required to provide the number of C atoms necessary to form one layer of graphene, and graphene growth normally starts at existing step edges of the SiC surface [39, 58]. If the SiC surface from which growth starts consist of a terrace with a single bilayer step edge, the decomposition of the terrace, beginning at the step edge, will only provide sufficient C atoms to nucleate graphene ribbons which will decorate the step edge and retard further step edge decomposition. Eventually etching will occur only if new lengths of SiC steps are created by etching dents in the step edge when two ribbons approach

each other. The arrow-like growth morphology is explained by a carbon diffusion-controlled growth which is also used to explain the roughening of initial straight steps often seen during graphene growth. Ohta *et al* concluded that step flow growth was not possible with single bilayer SiC steps due to instabilities caused by carbon diffusion leading to complex growth morphologies (See also Section 2.4.1 on Step Flow Growth).

Simple step flow growth, with maintenance of relatively straight step edges, appears to be only possible when growth of graphene starts from triple bilayer SiC steps. In this case, the number of carbon produced by the decomposing step edge is approximately equal to the number of carbon atoms in the same area of graphene. Also, in this case, the graphene evidently does not coat the receding step edge and retard Si sublimation, but is immediately incorporated in the graphene growth front.

Research at the U.S. Naval Research Laboratory by Nyakiti *et al* has demonstrated that growth of graphene on 2 – 4 μm high step free mesas of SiC deposited on 4H-SiC (0001) resulted in graphene with significant improvement over what is observed for epitaxial graphene (EG) grown on conventional SiC substrates [31, 74]. Although their main aim was to eliminate step-bunched edges, which has been shown to reduce carrier mobility and increase electrical resistance of EG [55-57], the method would have also ensured that growth occurred by decomposition of sufficient number of SiC bilayer, starting at the

mesa edges, to form large-area graphene with low, uniform strain approaching that of exfoliated graphene.

4.4.2 Finger Growth and Residual SiC Islands

Incomplete growth of graphene adjacent to step edges, as evidenced by fingerlike arrays of alternate graphene-SiC lamellae, is a feature seen when growth temperature is too low or growth time is too short. It was even observed that is some cases the same sample had areas of uniform graphene coverage with other areas showing finger growth. This may be due to inherent in-homogeneity in the sample itself or possibly non-uniform heating, especially when rotation of the stage was not used.

Figure 4.22 shows the AFM images of a sample grown without sufficient time for complete graphene growth across the terraces. The finger pattern can be seen at the edge of the advancing step with alternating lamellae of graphene and untransformed SiC. In addition, the images shows that finger growth also started at points on the terraces and had grown in a pattern as to reveal the points from which they emanate. The initiation points are probable vacancy point defects on the SiC surface, which are also believed to be responsible for the triangular pit features described next (Section 4.4.3). In fact, Figure 4.5 in Section 4.1.1 shows both finger and more uniform graphene growth associated with triangular pits.

When graphene grows in a finger pattern across terraces, it sometimes results in untransformed islands of SiC/buffer-layer (See Figures 4.8, 4.13 and 4.23). Some of these islands are straight and roughly perpendicular to step edges suggesting that they resulted from step edges finger growths after the step flow decomposition of SiC had occurred. However, some of the islands were more rounded suggesting that they resulted from finger growth originating at defect points on the terrace or as a result of a combination of step flow and growth from terrace defect points. Further research is required to determine the detailed mechanism for the SiC/buffer-layer island formation.

The residual SiC/buffer-layer islands would act as discontinuities in the grown graphene film and no doubt affect the electrical properties of the film.

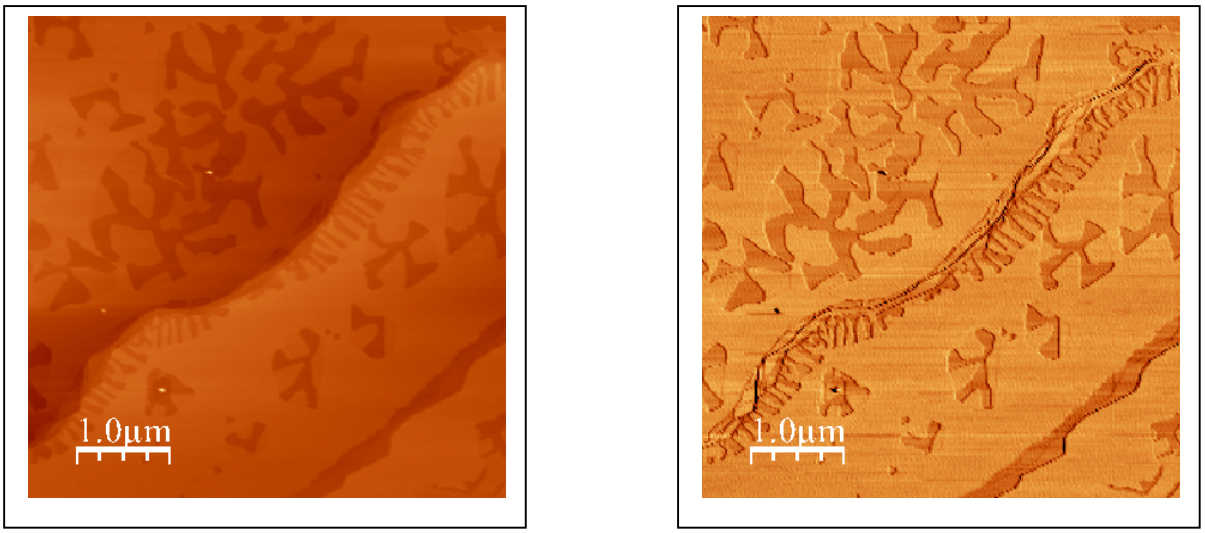

(a) Topographical image (b) Phase image

Figure 4.22: AFM images showing finger growths from both a step edge and from point defects on terraces.

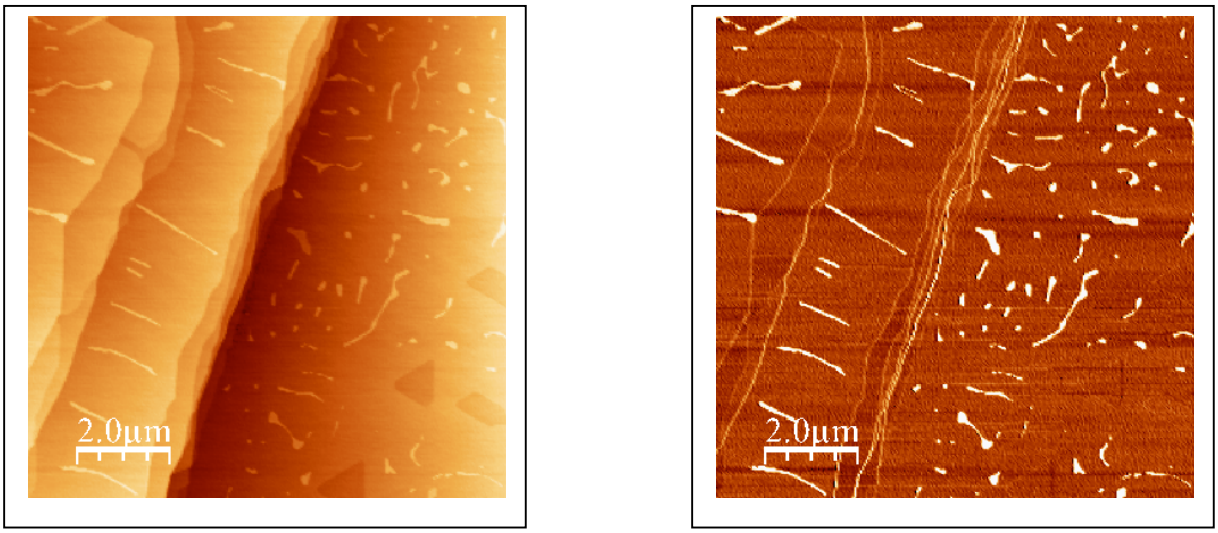

(a) Topographical images (b) Phase image

Figure 4.23: AFM images showing untransformed SiC/buffer layer islands on terraces after growth of graphene across the terrace.

4.4.3 Triangular Pits

In some growths, nucleation of graphene was observed to occur on the surface of the step terraces resulting in relatively shallow triangular depressions or pits (See Figure 4.24). On a given terrace, the majority of triangular pits had the same orientation, typically with one of the flat triangular edge parallel to the step edge (Figure 4.24 (a)). Step edges are usually perpendicular to the $\langle 11\bar{2}0 \rangle$ crystallographic directions and uniform step flow during bunching or reverse step flow during uniform thermal decomposition to form graphene is in the $\langle 11\bar{2}0 \rangle$ direction. In other words, step flow during bunching or decomposition is typically along the $\{11\bar{2}0\}$ planes. Hence, the orientation of the triangular pits

indicates that, after nucleation, they grow by erosion of the SiC along the three $\{11\bar{2}0\}$ planes and in the $\langle 11\bar{2}0\rangle$ directions.

A study by Bolen *et al* found similar types of pit formation and they further determined that the density of pits showed a clear trend of increasing with temperature [63]. As a result, they proposed that vacancy point defects, and not dislocations, were most likely the cause. The crystallographic orientation and growth pattern observed in this thesis research would support the point defects origin for the pits, however, the research did not provide sufficient data to assess the temperature effect.

Height profiles across the triangular pit in Figure 4.24 (a) revealed that the depths were about 4 to 4.5 Å (See Figures 4.24 (b) and (c)). This corresponds to the difference (4.2 Å) between a graphene layer thickness (3.3 Å) and the thickness of the three SiC bilayers (7.5 Å) that need to decompose to form graphene. This indicates that a graphene layer was formed on the bottom of the pit during formation. Graphene growth via terrace pits can no doubt impinge on each other, and with graphene from step flow decomposition, possibly reducing the domain size of films. On the other hand, since growth orientation from step and pits are similar, impinging graphene films may be coherent enough to bond seamlessly. Further research would be required to determine the exact effect. In any case, isolated surface pits after growth will cause surface roughening and hence degrade the uniformity and electrical properties of the graphene films.

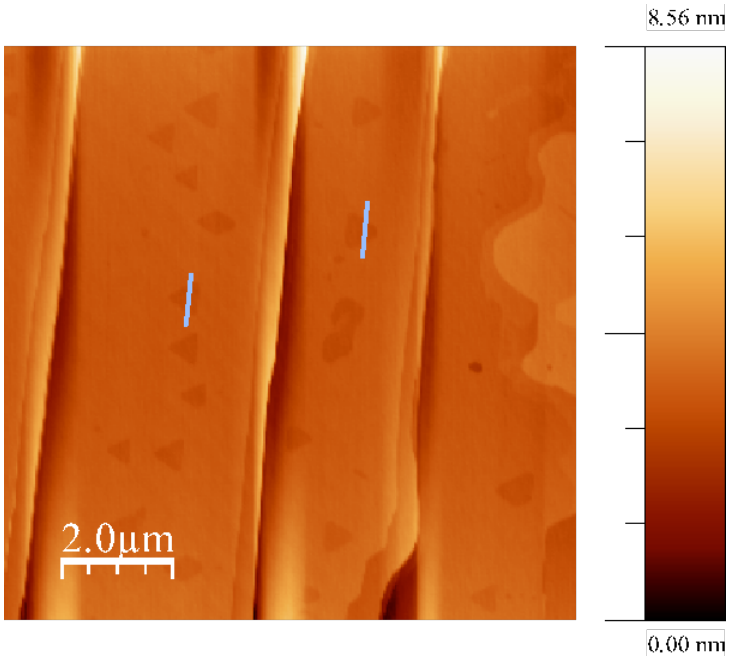

(a)

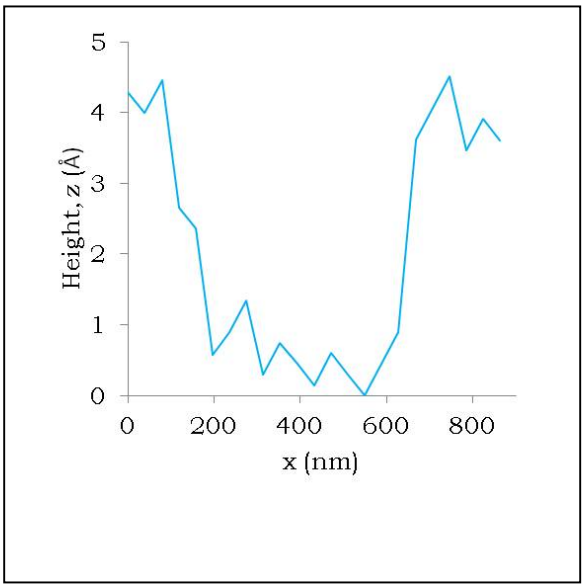

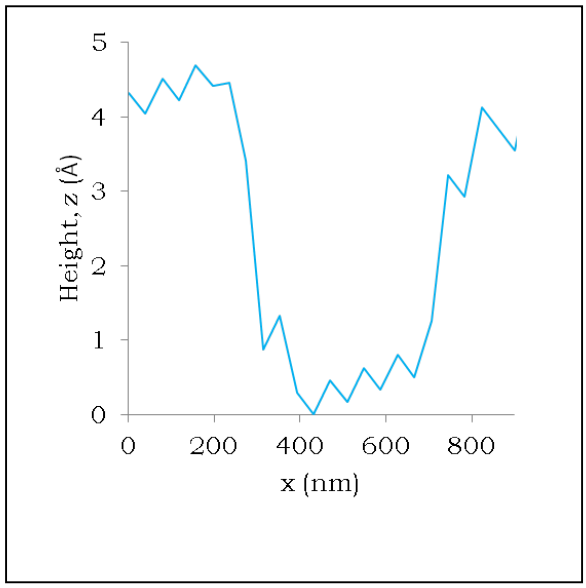

(b) (c)

Figure 4.24: (a) AFM image showing triangular pit on the step terraces. Figures (b) and (c) give height profiles across two pits shown in (a).

4.4.4 Extra Layer Growth at Step Edges

It was observed that narrow strips of additional graphene layer(s) usually started to form at new step edges once at least a single layer had grown across the step terraces. For example, growth with monolayer graphene across the terraces often exhibited one or two thin strips of graphene film adjacent to the step edges (See Figures 4.11 and 4.13).

4.5 Electrical Characteristics

Table 1 gives the measured electrical characteristics for a set of samples.

A plot of carrier mobility versus sheet carrier concentration for this set of samples (Figure 4.25) showed that, although there was significant scatter in data points, the overall trend was that carrier mobility decreased with increase in sheet carrier concentration, consistent with other research findings [7, 30, 38]. As carriers arise from donor-like states associated with the buffer layer and its interface to the substrate, scattering by these ionized donor states will increase with increase in carrier concentration leading to reduced mobility.

The lowest carrier mobility was obtained for the 1500 °C growths. This was expected since AFM showed that graphene growth at 1500 °C was limited to films adjacent to step edges, even for 45 min growth, so that the samples were effectively non-conducting. Very high sheet resistance values were also obtained for these samples (See Figure 4.26). Samples grown at very high

temperatures that caused deep-pit formation exhibited low carrier mobility and relatively high sheet carrier densities. The low carrier mobility is likely to be due to increased electron scattering resulting from a high density of trapped charges associated with the pits. The pits constitute regions of high defect density which would provide a high density of donor states and charge traps leading to increased *n*-doping of the graphene film along with enhanced scattering of sheet carriers.

Table 1: Electrical Properties of Graphene Grown Under Various Conditions of Temperature and Time

Growth Temperature (°C)	Growth Time (min)	Sheet Carrier Concentration (cm^{-2})	Carrier Mobility ($cm^2/V.s$)	Sheet Resistance (Ω/sq.)
1500	30	5.59×10^{12}	21	73120
1500	45	4.81×10^{12}	13	100202
1550	30	3.33×10^{12}	566	3309
1550	45	8.60×10^{12}	368	2084
1575	30	4.64×10^{12}	597	2264
1575	30	8.18×10^{12}	325	2404
1600	15	3.17×10^{12}	592	4158
1600	15	3.29×10^{12}	616	3312
1600	45	2.79×10^{12}	841	3023
1600	45	5.75×10^{12}	797	1411
1615	5	6.70×10^{12}	501	1960
1620	10	8.60×10^{12}	477	1525
1625	15	7.42×10^{12}	485	1800
1625	15	6.70×10^{12}	363	2619
1625	30	5.13×10^{12}	703	1734
1650	15	2.60×10^{12}	814	2985
1650	20	8.39×10^{12}	566	1326
1705	5	1.30×10^{13}	280	1784
>1705	5	1.25×10^{13}	208	2477

In general, higher mobility was obtained for samples grown at 1600 °C – 1650 °C where there was uniform growth of at least a monolayer of graphene. The highest mobility of 840 $cm^2/V.s$ was obtained for a sample grown at 1600 °C for 45 min for which Raman spectroscopy indicated a 2 – 3 layer growth. The as-grown graphene was intrinsically electron doped with sheet carrier density in the range of 3 – 9 x 10^{12} cm^{-2}.

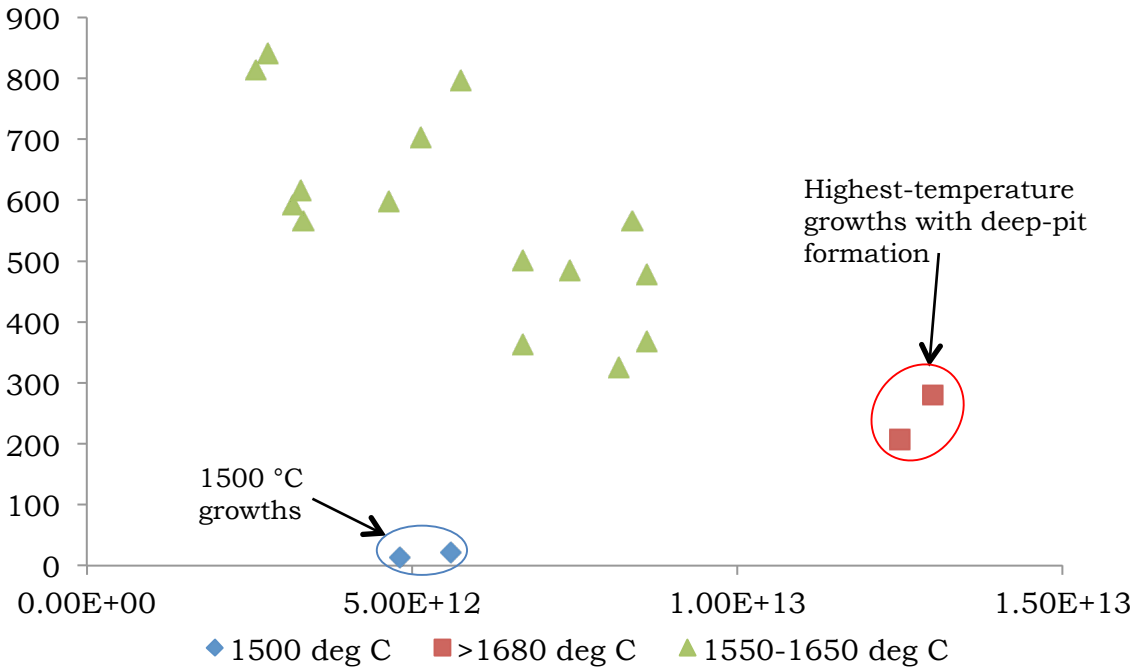

Figure 4.25: Plot of carrier mobility versus sheet carrier concentration for a set of samples.

Plots of electrical properties, (sheet resistance, carrier mobility and carrier concentration), versus growth temperature for 15 min growth time are given in Figures 4.26 – 4.28. Sheet resistance versus growth temperature for 15 min

growth time is plotted on a semi-log graph in Figure 4.26. The very high sheet resistance of the growths at 1575 °C and below, relative to growths at 1600 °C – 1650 °C is clearly indicated. This is because for 15 min growths at 1675 °C and below, the graphene growth had not extended across terraces but was limited to strips adjacent to step edges. On the other hand, growths at 1600 °C and above usually resulted in complete coverage of the terraces with at least a monolayer of graphene. It should be noted, however, that growth for longer time (45 min) at a temperature as low as 1550 °C did result in growth of 1 – 2 layer graphene with sheet resistance in the same order as 1600 °C, 15 min growths.

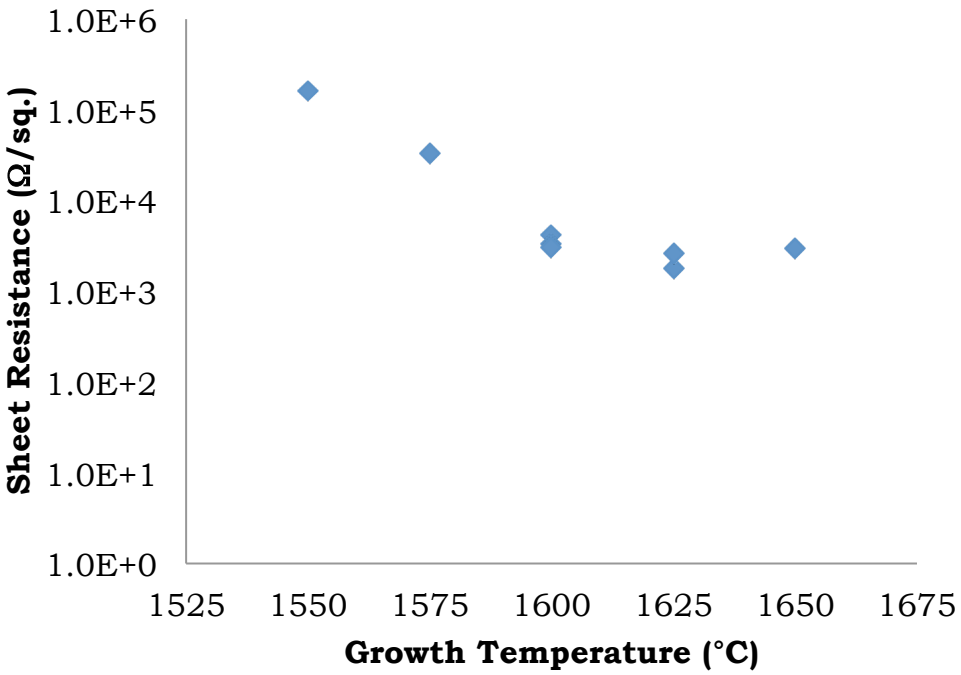

Figure 4.26: Plot of sheet resistance versus growth temperature for 15 min growths.

The plot of carrier mobility versus growth temperature (Figure 4.27) shows the expected trend of increasing carrier mobility with temperature within the temperature range that deep pit formation does not occur. The increase in mobility with temperature is consistent with the increased and more uniform coverage of the surface with graphene as the temperature increases.

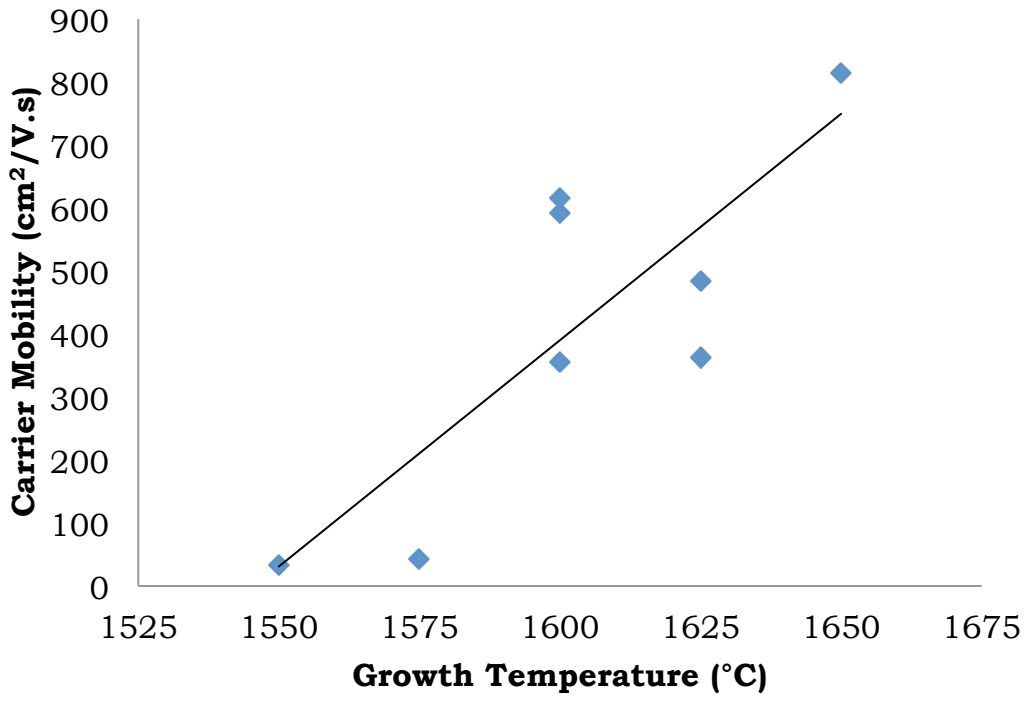

Figure 4.27: Plot of carrier mobility versus growth temperature for 15 min growths.

Figure 4.28 shows that there was a large scatter in the data for carrier concentration versus growth temperature. Hence, no correlation could be

made between carrier concentration and growth temperature within the 1550 °C to 1650 °C range plotted here. However, as discussed earlier, growth at higher temperatures where deep pits formed did result in increased carrier concentration due to the doping effect of the pits.

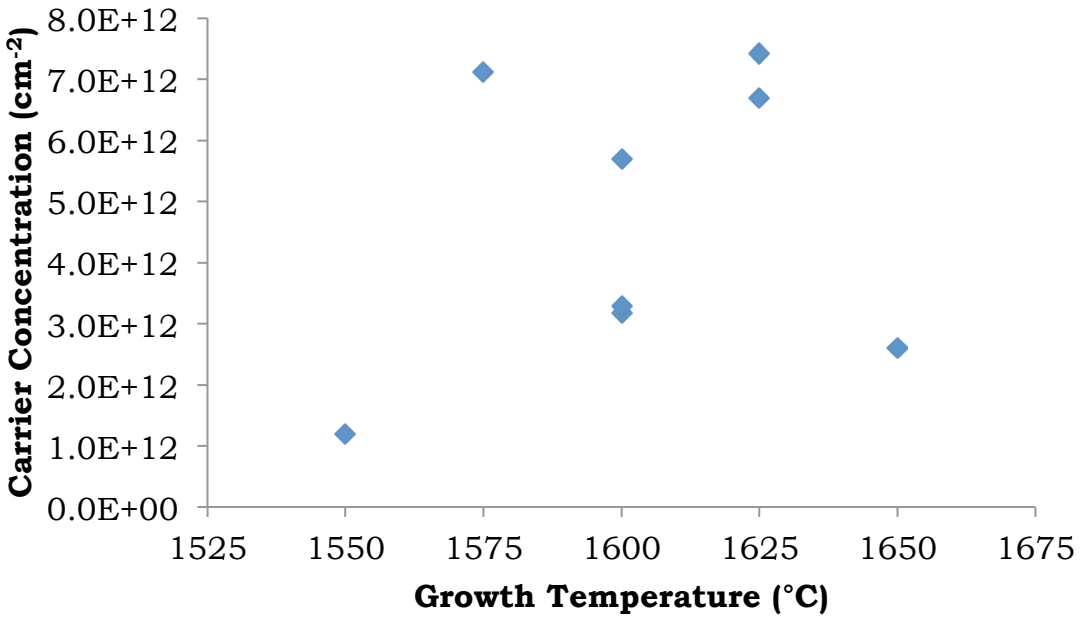

Figure 4.28: Plot of carrier concentration versus growth temperature for 15 min growths.

4.6 TEM Characterization

For the first time EG grown on SiC were transferred and imaged by TEM as a suspended film, in plan-view. Previous TEM studies on SiC EG involved cross-sectional imaging of multilayer graphene still attached to the SiC substrate [53, 68]. These were aimed at studying the stacking configuration of graphene with Raman signature, and with local morphological features of the SiC substrate,

such as step edges. Graphene obtained by micromechanical cleavage of graphite, CVD graphene grown on metal substrate, and CVD graphene grown on dielectric substrates have been previously imaged in plan-view [6, 21, 23, 75, 76]. CVD graphene grown on sapphire (Al_2O_3) has also been subsequently imaged this way [26].

The plan-view high-resolution TEM imaging done here was able to show the planar real space atomic structure of the EG, distinguish between monolayer and bilayer regions of the membrane, and establish the stacking registry of the bilayer graphene. The TEM micrographs shown in Figures 4.29 – 4.31 were for a mainly bilayer graphene sample. This sample was originally grown as monolayer graphene, but subsequent hydrogen intercalation before transfer would have converted it into bilayer graphene by decoupling and transformation of the intrinsic buffer layer (See Section 2.2.3).

Figure 4.29 shows the TEM micrographs of the transferred bilayer EG. The overview image and HRTEM images at three different positions are shown. The overview image showed that there was some wrinkling and tears in the film, likely arising from the transfer process. The upper right HRTEM image was taken adjacent a tear and the two-layer boundary of the graphene bilayer can be clearly seen, as evidenced by the two dark lines. Figure 4.30 shows a HRTEM of the film and a fast Fourier transform (FFT) of the image. These data indicate that the rotation between the graphene layers was 0° confirming *AB* stacking. In Figure 4.31, selected-area electron diffraction (SAED) patterns

taken at the position shown in 4.31 (a), are given in 4.31 (b). Intensity profile taken along the four diffraction spots, highlighted in the figure, indicated that the position where the SAED was done consisted of bilayer graphene with *AB* stacking [76].

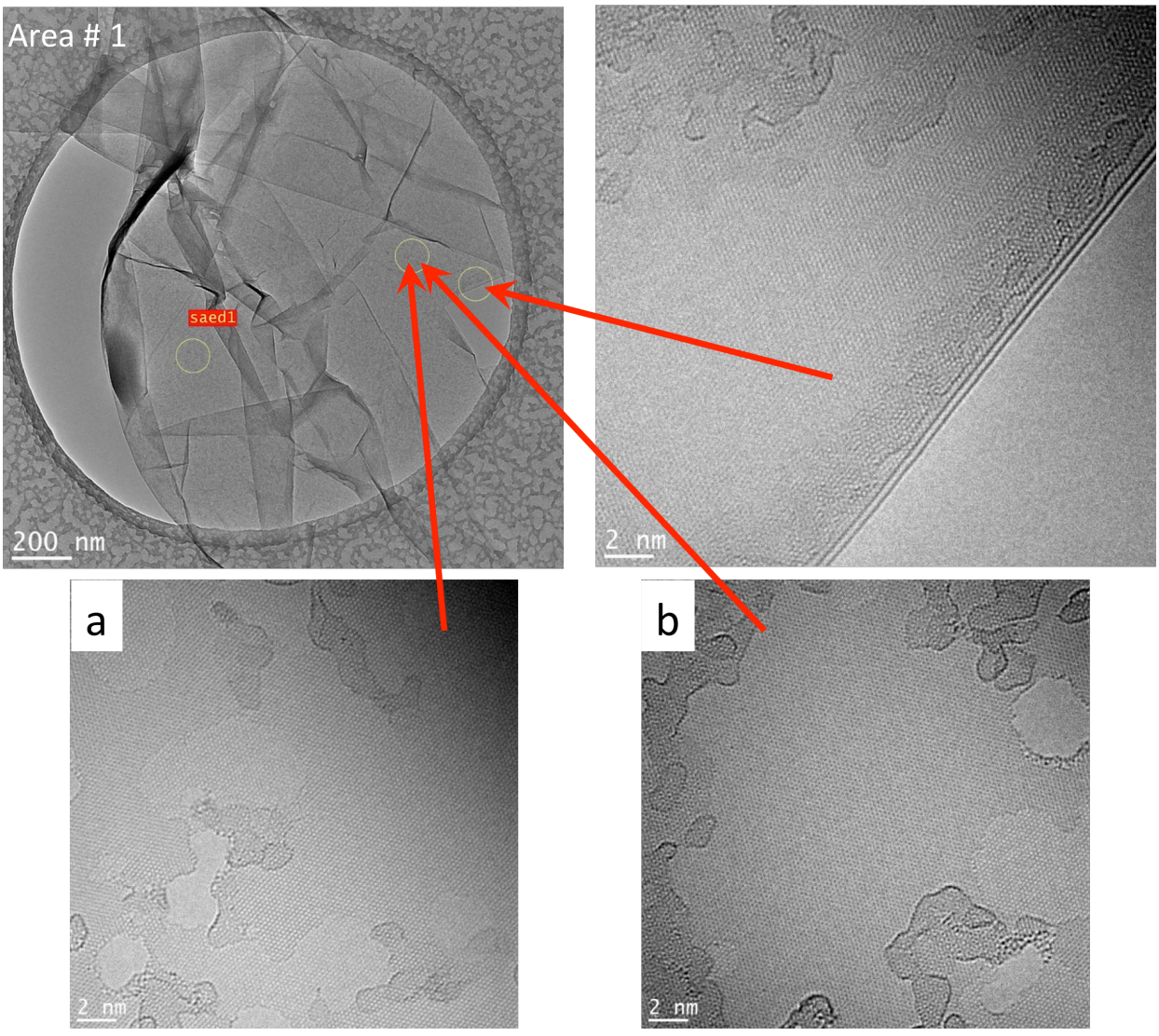

Figure 4.29: Overview image and TEM micrographs at three position of a mainly bilayer EG graphene film. The two straight lines at the edge of a tear in the film (top right micrograph) clearly shows the bilayer nature of film.

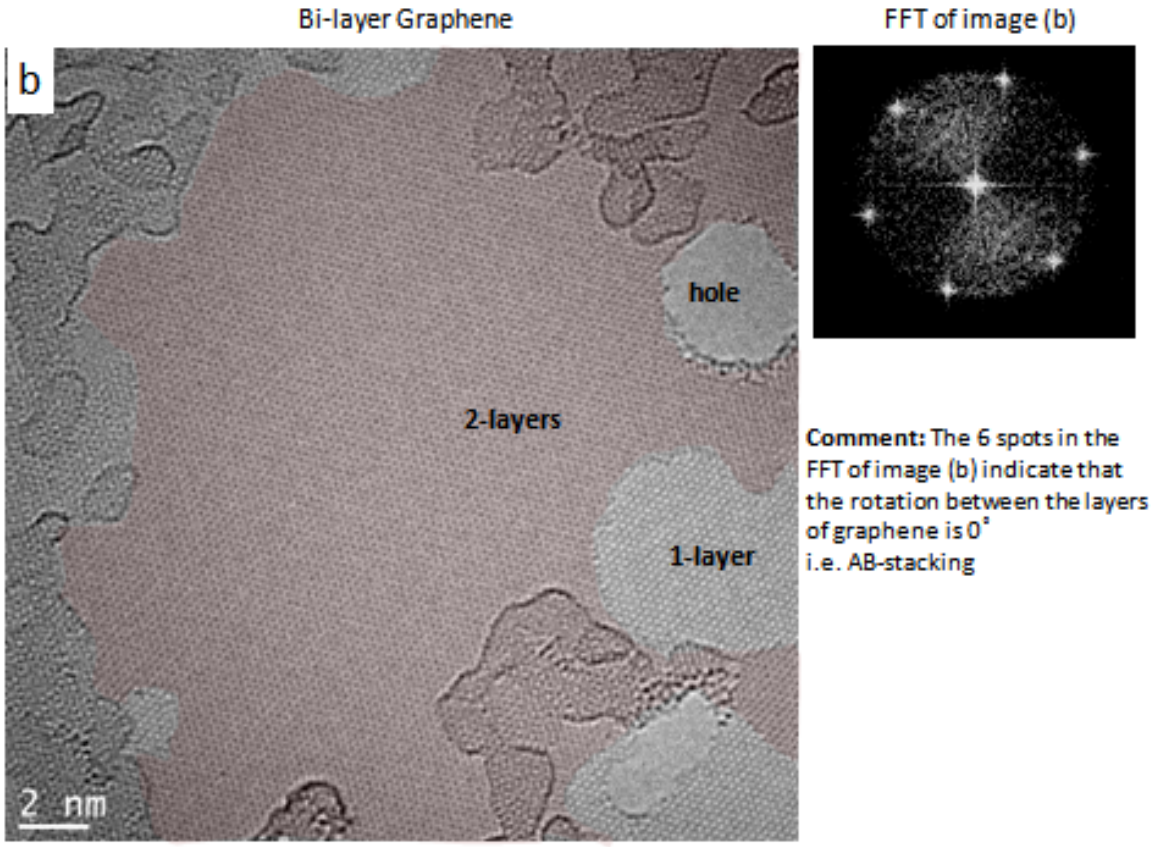

Figure 4.30: HRTEM of film and fast Fourier transform of film (top right) indicating that the rotation between the graphene layers is 0°, confirming *AB* stacking.

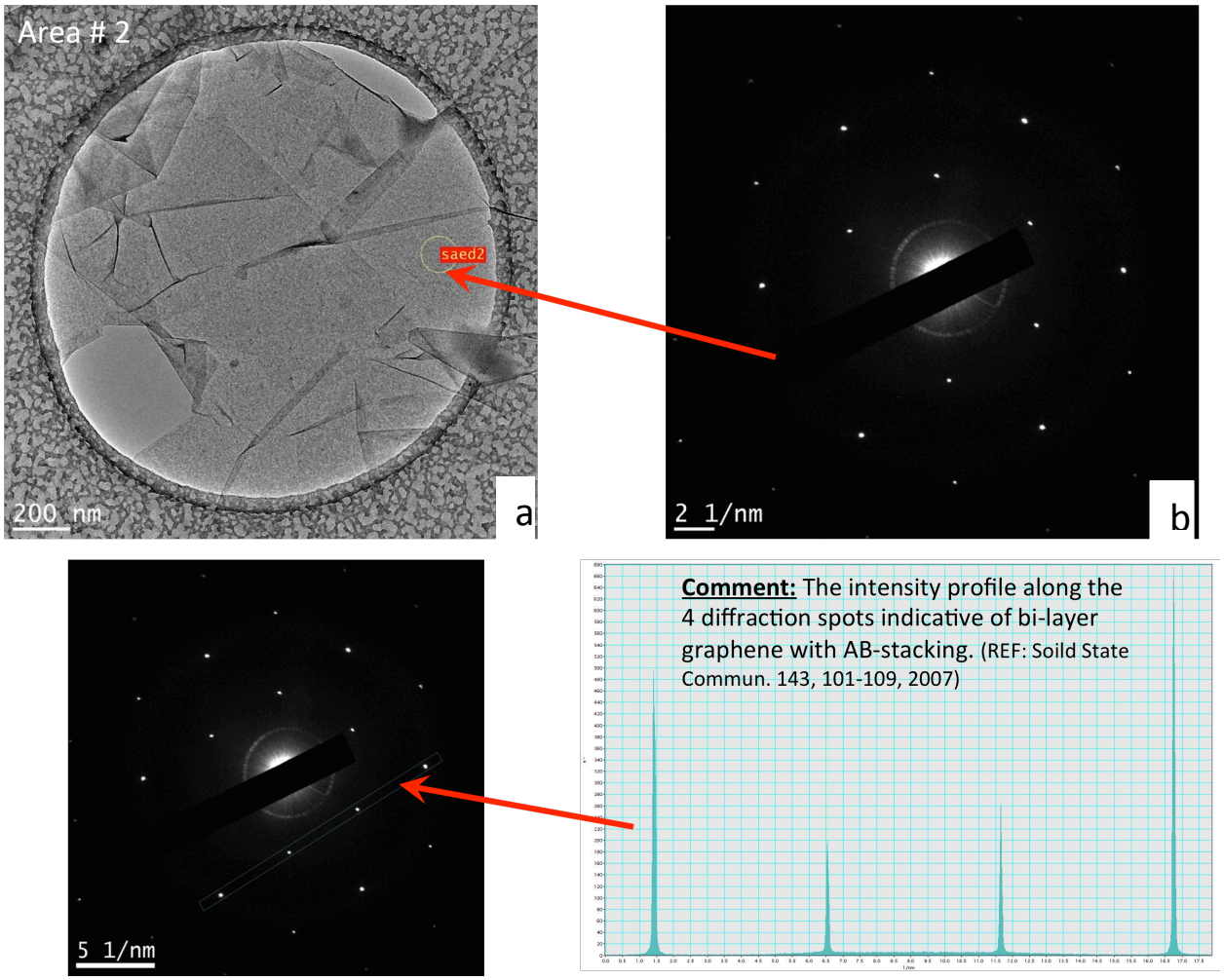

Figure 4.31: Selected-area electron diffraction (SAED) taken at the position shown, and the resulting diffraction patterns. Intensity profile taken along the four diffraction spots, highlighted in the figure, indicated that the position where the SAED was taken consisted of bilayer graphene with *AB* stacking [Reference 76].

4.7 Elevated Temperature Oxidation Study

Silicon carbide (SiC) is a wide band-gap, high thermal conductivity material with a high breakdown electric field and a high electron saturation velocity. It can therefore be used in high-temperature electronics, in high power switching and in high frequency power generation [47, 48]. It is envisaged that graphene grown on SiC could be integrated with the SiC substrate for devices operating in harsh environment at high temperatures, provided that the graphene can remain stable at the high operating temperatures. Hence, for this research, a limited oxygen etching study was done on multi-layer graphene grown under high vacuum conditions to assess it stability at elevated temperature in a highly oxidizing atmosphere (pure oxygen).

Etch rate was determined to be about 0.33 layer/min (or 1 layer every 3 min) at 600 °C. No etching was observed at 500 °C or below. These results are consistent with an independent study done by Liu *et al*, but using graphene obtained from mechanically exfoliated Kish graphite [77]. They found that under an O_2/Ar gas flow, (with oxygen partial pressure of 350 Torr), no oxidative etching was observed in bi-layer or triple-layer graphene after 2h at 500 °C. However, etch pits were observed by AFM in single layer graphene at 450 °C but not at 400 °C or below. These results indicate that graphene is resistant to oxidative etching, even in pure oxygen, at atmosphere pressure up to 400 °C. The indications are therefore that graphene is suitable for elevated temperature application under atmospheric conditions, and also that it is a very good complementary material for integrated graphene-SiC electronic.

However, further research is required to study the oxidation behavior under different partial pressures of oxygen and to elucidate the thermodynamics of the oxidative etching process. The effects of other types of oxidizing environments also require further research.

CHAPTER 5

CONCLUSIONS AND RECOMMENDATIONS

1. The modified CVD chamber at the Wide-Bandgap-Semiconductor Laboratory at Cornell University was shown to successfully grow uniform large-area epitaxial graphene by thermal decomposition of 6H-SiC(0001) at near atmospheric pressure.

2. Only formation of the graphene-like ($6\sqrt{3}$ x $6\sqrt{3}$)R30° surface reconstruction occurred at 1450 °C with no graphene grown even after 45 minutes of processing time. Very limited growth of graphene was achieved at 1500 °C. At 1550 °C, complete coverage of the growth surface with a monolayer of graphene was achieved after 30 minutes. Uniform, large area monolayer graphene was grown in 15 minutes at 1600 °C, sometimes with thin strips of bilayers and/trilayers graphene adjacent to step edges. Terrace widths after growths were as high as 8 μm.

3. Raman spectroscopy and X-ray photoelectron spectroscopy (XPS) confirmed a clear trend of increasing graphene layer thickness with increasing temperature and time.

4. For the first time, transmission electron microcopy (TEM) was used to image epitaxial graphene film grown on SiC, in plan-view. TEM and selected-area electron diffraction (SAED) confirmed that the layers in a bilayer film had *AB* Bernal stacking order.

5. Several growth features, namely deep rounded pits at the higher temperatures, shallow triangular pits, arrow-like incursions across terrace, finger growths, residual SiC islands on terraces, nucleation of graphene at multiple defect points on terraces, and extra graphene layers at step edges, were observed. These generally led to roughening of the growths surface, reduced domain size and uniformity of the graphene grown, and in turn negatively affected the electrical properties of the epitaxial graphene. Further research is required to determine the formation mechanisms of these features and to determine how they can be eliminated or reduced.

6. Electrical measurements showed that there was a general trend of increasing carrier mobility with decreasing sheet carrier concentrations. Higher carrier mobilities, (up to 840 $cm^2/V.s$), were obtained for samples grown at 1600 °C – 1650 °C where uniform growth of at least a monolayer graphene was obtained. The as-grown graphene was intrinsically electron doped with sheet carrier density in the range of 3 – 9 x 10^{12} cm^{-2}. Growth at temperatures greater than 1650 °C tended to result in the formation of deep rounded pits, roughening of the substrate surface and reduced carrier mobility.

7. Elevated temperature oxidation study of multi-layer epitaxial graphene showed that graphene is resistant to oxidative etching, even in pure oxygen at atmospheric pressure, up to 400 °C. However, further research is required to study the oxidation behavior under other oxygen partial pressures, in other

oxidizing environments, and to elucidate the thermodynamics of the oxidation process.

8. In this research, pre-graphitization hydrogen etching of the SiC substrate was not carried out although it is considered an important production step by other researchers. However, uniform large-area graphene was still successfully grown at near atmospheric pressure. Modification of the growth chamber to facilitate wafer preparation by *in situ* hydrogen etching is expected to improve the growth morphology of the graphene.

9. The effect of SiC wafer quality was not studied in this research. However, there were indications that there was some variation in results between growths on samples from different wafers. Careful selection of SiC wafers, in terms of defect density and off-cut angle from on-axis, would be expected to give more consistent and improved growth morphology.

REFERENCES

1. K.S. Novoselov, A.K. Geim, S.V. Morosov, D. Jiang, Y. Zhang, S.V. Dubonos, I.V. Grigorieva, and A.A. Firsov. *Science* **306**, 666-669, (2004).

2. K.S. Novoselov, A.K. Geim, S.V. Morozov, D. Jiang, M.I. Katsnelson, I.V. Grigorieva, S.V. Dubonos, and A.A. Firsov. *Nature* **438**, 197-200, (2005).

3. N.M.R Peres, F. Guinea, and A.H. Castro Neto. *Physical Review B* **73**, 125411, (2006).

4. A.K. Geim and K.S. Novoselov. *Nature Materials* **6**, 183-191, (2007).

5. Y. Zang, Y-W. Tan, H.L Stormer, and P. Kim. *Nature* **438**, 201-204, (2005).

6. T.J. Booth, P. Blake, R. Nair, D. Jiang, E.W. Hill, U. Bangert, A. Bleloch, M. Gass, K.S. Novoselov, M.I. Katsnelson, and A.K. Geim. *Nano Letters* **8** (8), 2442, (2008).

7. V. Dorgan, M-H. Bae, and E. Pop. *Applied Physics Letters* **97**, 082112, (2010).

8. F. Schwierz. *Nature Nanotechnology* **5**, 487-496, (2010).

9. A.K. Geim. *Science* **324**, 1530-1534, (2009).

10. M.C. Lemme, T.J. Echtermeyer, M. Baus, and H. Kurz. *IEEE Electron Device Letters* **28** (4), (2007).

11. D. Jiang, V.R. Cooper, and S. Dai. *Nano Letters* **9** (12), 4019-4024, (2009).

12. P. Blake, P.D. Brimicombe, R.R. Nair, T.J. Booth, D. Jiang, F. Schedin, L.A. Ponomarenko, S.V. Morozov, H.F. Gleeson, E.W. Hill, A.K. Geim, and K.S. Novoselov. *Nano Letters* **8** (6), 1704-1708, (2008).

13. Q. He, S. Wu, Z. Yin, and H. Zhang. *Chemical Science* **6**, 1764-1772, (2012).

14. N.D. Mermin. *Physical Review* **176**, 250-254, (1968).

15. K.H. Lee, H-J. Shin, J. Lee, I. Lee, G-H. Kim, J-Y. Choi, and S-W. Kim. *Nano Letters* **12**, 714-718, (2012).

16. Z. Liu, L. Song, S. Zhao, J. Huang, L. Ma, J. Zhang, J. Lou, and P.M. Ajayan. *Nano Letters* **11**, 2032-2037, (2011).

17. C.R. Dean, A.F. Young, I. Meric, C. Lee, L. Wang, S. Sorgenfrei, K. Watanabe, T. Taniguchi, P. Kim, K.L. Shepard, and J. Hone. *Nature Nanotechnology* **5** (10), 722-726, (2010).

18. J. Young Kwak, J. Hwang, M. Graham, H. Alsalman, N. Munoz, B. Calderon, and M. Spencer. *Device Research Conference (DRC)* 2013 71st Annual (Volume: Supplement), p. 1-2.

19. P. Blake, E.W. Hill, A.H. Castro Neto, K.S. Novoselov, D. Jiang, R. Yang, T.J Booth, and A.K. Geim. *Applied Physics Letters* **91**, 063124, (2007).

20. K.I. Bolotin, K.J. Sikes, J. Hone, H.L. Stormer, and P. Kim. *Physical Review Letters* **101**, 096802, (2008).

21. A. Reina, X. Jia, J. Ho, D. Nezich, H. Son, V. Bulovic, M. Dresselhaus, and J. Kong. *Nano Letters* **4** (1), 30-33, (2009).

22. X. Li, W. Cai, J. An, S. Kim, J. Nah, D. Yang, R. Piner, A. Vetamakanni, I. Jung, E. Tutuc, S. Banerjee, L. Colombo, R. Ruoff. *Science* **324**, 1312, (2009).

23. M.H. Rummeli, A. Bachmatiuk, A. Scott, F. Borrnert, J.H. Warner, V. Hoffman, J-H Lin, G. Cuniberti, and B Buchner. *ACS Nano* **4** (7), 4206-4210, (2010).

24. J. Sun, N. Lindvall, M.T. Cole, T. Wang, T.J. Booth, P. Boggild, K.B.K. Teo, J. Liu, and A. Yurgens. *Journal of Applied Physics* **111**, 044103-1 – 044103-6, (2012).

25. J. Sun, N. Lindvall, M.T. Cole, K.B.K. Teo, and A. Yurgens. *Applied Physics Letters* **98**, 252107-1 – 252107-3, (2011).

26. J. Hwang, M. Kim, D. Campbell, H.A. Alsalman, J. Young Kwak, S. Shivaraman, A.R. Woll, A.K. Singh, R.G. Hennig, S. Gorantla, M.H. Rummeli, M.G. Spencer. *ACS Nano* **7** (1), 385-395, (2013).

27. A.J. van Bommel, J.E. Crombeen, and A. van Tooren. *Surface Science* **48**, 463-472, (1975).

28. C. Berger, Z. Song, T. Li, X. Li, A.Y. Ogbazghi, R. Feng, Z. Dai, A.N. Marchenkov, E.H. Conrad, P.N. First, and W.A. de Heer. *Journal of Physical Chemistry B* **108**, 19912-19916, (2004).

29. C. Virojanadara, M. Syvajarvi, R. Yakimova, and L.I. Johansson. *Physical Review B* **78**, 245403, (2008).

30. P.N. First, W. A. de Heer, T. Seyller, C. Berger, J.A. Stroscio, J-S. Moon. *MRS Bulletin* **35**, (2010).

31. L.O. Nyakiti, V.D. Wheeler, N.Y. Garces, R.L. Myers-Ward, C.R. Eddy Jr., and D.K. Gaskill. *MRS Bulletin* **37**, 1149-1157, (2012).

32. C. Virojanadara, R. Yakimova, J.R. Osiecki, M. Syvajarvi, R.I.G Uhrberg, L.I. Johansson, and A.A. Zakharov. *Surface Science* **603**, L87-L90, (2009).

33. G. Reza Yazdi, R. Vasiliauskas, T. Iakimov, A. Zakharov, M. Syvajarvi, and R. Yakimova. *Carbon* **57**, 477-484, (2013).

34. R.M. Tromp and J.B. Hannon. *Physical Review Letters* **102**, 106104, (2009).

35. K.V. Emtsev, A. Bostwick, K. Horn, J. Jobst, G.L. Kellogg, L. Ley, J.L. McChesney, T. Ohta, S.A. Reshanov, J. Rohrl, E. Rotenberg, A.K. Schmid, D. Waldmann, H.B. Weber, and T. Seyller. *Nature Materials* **8**, 203-207, (2009).

36. K.V. Emtsev, F. Speck, T. Seyller, and L. Ley. *Physical Review B* **77**, 155303, (2008).

37. J.K. Hite, M.E. Twigg, J.L. Tedesco, A.L. Friedman, R.L. Myers-Ward, C.R. Eddy, Jr., and D.K. Gaskill. *Nano Letters* **11**, 1190-1194, (2011).

38. J.L. Tedesco, B.L. VanMil, R.L. Myers-Ward, J.M. McCrate, S.A. Kitt, P.M. Campbell, G.G. Jernigan, J.C. Culbertson, C.R. Eddy, Jr., and D.K. Gaskill. *Applied Physics Letters* **95**, 122102, (2009).

39. J. Hass, W.A. de Heer, and E.H. Conrod. *Journal of Physics: Condensed Matter* **20**, 323202, (2008).

40. J.A. Robinson, M. Hollander, Michael LaBella, III, K.A. Trumbull, R. Cavalero, and D.W. Snyder. *Nano Letters* **11**, 3875-3880, (2011).

41. C. Riedl, U. Starke, J. Bernhardt, M. Frank, and K. Heinz. *Physical Review B* **76**, 245406, (2007).

42. N. Srivastava, G. He, Luxmi, and R.M. Feenstra. *Physical Review B* **85**, 041404, (2012).

43. G. He, N. Srivastava, and R.M. Feenstra. *Journal of Electronic Materials* **43** (4), 819-827, (2014).

44. C. Riedl, C. Coletti, T. Iwasaki, A.A. Zakharov, and U. Starke. *Physical Review Letters* **103**, 246804, (2009).

45. C. Virojanadara, A.A. Zakharov, R. Yakimova, L.I. Johansson. *Surface Science* **604**, L4-L7, (2010).

46. F. Speck, J. Jobst, F. Fromm, M. Ostler, D. Waldmann, M. Hundhausen, H.B. Weber, and T. Seyller. *Applied Physics Letters* **99**, 122106, (2011).

47. P.G. Neudeck, R.S. Okojie, and L.Y. Chen. *Proceedings of IEEE* **90** (6), 1065-1076, (2002).

48. M. Bhatnager, and B.J. Baliga. *IEEE Trans. Electronic Devices* **40** (3), 645-656, (1993).

49. C.H. Park, B-H. Cheong, K-H. Lee, and K.J. Chang. *Physical Review B* **47** (7), 4485-4493, (1994).

50. O. Madelung *et al. Group IV Elements IV-V and III-IV Compounds Part b – Electronic, Transport, Optical and Other Properties*, Landbold-Bornstein – Group III Condensed Matter, Vol. 41A1b, Springer.

51. P.T.B Shaffer. *Acta Crystallography* **B25**, 477, (1969).

52. T. Ayalew. *SiC Semiconductor Devices Technology, Modeling and Simulation*, Dissertation for Doctor of Technical Sciences, Technical University of Vienna, Austria. (http:/www.iue.tuwien.ac.at/phd/ayalew/node20.html)

53. J. Robinson, X. Weng, K. Trumbull, R. Cavalero, M. Wetherington, E. Frantz, M. LaBella, Z. Hughes, Mark Fanton, and D. Snyder. *ACS Nano* **4** (1), 153-158, (2010).

54. J.A Robinson, K.A. Trumbull, M. LaBella III, R. Cavalero, M.J. Hollander, M. Zhu, M.T. Wetherington, M. Fanton, and D.W. Snyder. *Applied Physics Letters* **98**, 222109, (2011).

55. M.K. Yakes, D. Gunlycke, J.L. Tedesco, P.M. Campbell, R.L. Myers-Ward, C.R. Eddy, Jr., D.K. Gaskill, P.E. Sheehan, and A.R. Laracuente. *Nano Letters* **10**, 1559-1562, (2010).

56. Y. Guo, L.W. Guo, J. Huang, R. Yang, Y.P. Jia, J.J. Lin, W. Lu, Z.L. Li and X.L. Chen. *Journal of Applied Physics* **115**, 043527, (2014).

57. Y-M. Lin, D.B. Farmer, K.A. Jenkins, J.L. Tedesco, R.L. Myers-Ward, C.R. Eddy, Jr., D.K. Gaskill, and Y. Wu. *IEEE Electron Device Letters* **32** (10), 1343-1345, (2011).

58. M. Hupalo, E.H. Conrad, and M.C. Tringides. *Physical Review B* **80**, 041401(R), (2009).

59. J. Ristein, S. Mammadov, and Th. Seyller. *Physical Review Letters* **108**, 246104, (2012).

60. A.H. Castro Neto, F. Guinea, N.M.R. Peres, K.S. Novoselov, and A.K. Geim. *Review of Modern Physics* **81**, 109, (2009).

61. V. Borovikov, and A. Zangwill. *Physical Review B* **80** (12), p.4, (2009).

62. T. Kimoto, A. Itoh, and H. Matsunami. *Journal of Applied Physics* **81** (8), 3494-3500, (1997).

63. M.L. Bolen, S.E. Harrison, L.B. Biedermann, and M.A. Capano. *Physical Review B* **80**, 115433, (2009).

64. T. Ohta, N.C. Bartelt, S. Nie, K. Thurmer, and G.L. Kellogg. *Physical Review B* **81**, 121411(R), (2010).

65. S. Shivaraman, M.V.S. Chandrashekhar, J.J. Boeckl, and M.G. Spencer. *Journal of Electronic Materials* **38** (6), 725-730, (2009).

66. D.S. Lee, C. Riedl, B. Kraub, K. von Klitzing, U. Starke, and J.H. Smet. *Nano Letters* **8** (12), 4320-4325, (2008).

67. Z.H. Ni, W. Chen, X.F. Fan, J.L. Kuo, T. Yu, A.T.S. Wee, and Z.X. Shen. *Physical Review B* **77**, 115416, (2008).

68. J. Rohrl, M. Hundhausen, K.V. Emtsev. T. Seyller, R. Graupner, and L. Ley. Applied Physics Letters **92**, 201918, (2008).

69. J.A. Robinson, M. Wetherington, J.L. Tedesco, P.M. Campbell, X. Weng, J. Stitt, M.A. Fanton, E. Frantz, D. Snyder, B.L. VanMil, G.G. Jernigan, R.L. Myers-Ward, C.R. Eddy, Jr., and D.K. Gaskill. *Nano Letters* **9** (8), 2873-2876, (2009).

70. S. Gorantla, A. Bachmatiuk, J. Hwang, H.A. Alsalman, J. Young Kwak, T. Seyller, J. Eckert, M.G. Spencer, and M.H. Rummeli. *Nanoscale* **6** (12), 889-896, (2013).

71. S. Unarunatoi, Y. Murata, C.E. Chialvo, H-S. Kim, S. MacLaren, N. Mason, I. Petrov, and J.A. Rogers. *Applied Physics Letters* **95**, 202101, (2009).

72. J.B. Hannon, and R.M. Tromp. *Physical Review B* **77**, 241404(R), (2008).

73. M. Ohring. *Materials Science of Thin Films* (2nd Ed.), Academic Press, (2002).

74. L.O. Nyakiti, R.L. Myers-Ward, V.D. Wheeler, E.A. Imhoff, F.J. Bezares, H. Chun, J.D. Caldwell, A.L. Friedman, B.R. Matis, J.W. Baldwin, P.M. Campbell, J.C. Culbertson, C.R. Eddy, Jr., G.G. Jernigan, and D.K. Gaskill. *Nano Letters* **12**, 1749-1756, (2012).

75. P.Y. Huang, J.C. Meyer, and D.A. Muller. *MRS Bulletin* **37**, 1214-1221, (2012).

76. J.C. Meyer, A.K. Geim, M.I. Katsnelson, K.S. Novoselov, D. Obergfell, S. Roth, C. Girit, and A. Zettl. *Solid State Communications* **143**, 101-109, (2007).

77. L. Liu, S. Ryu, M.R. Tomasik, E. Stolyarova, N. Jung, M.S. Hybertsen, M.L. Steigerwald, L.E. Brus, and G.W. Flynn. *Nano Letters* **8** (7), 1965-1970, (2008).